

Fiber-based Light Sources for Coherent Raman Scattering and Multi-Photon Imaging

Dissertation
zur Erlangung des akademischen Grades
Doktor-Ingenieur (Dr.-Ing.)

vorgelegt dem Rat der Physikalisch-Astronomischen Fakultät
der Friedrich-Schiller-Universität Jena
von Dipl.-Phys. Thomas Gottschall
geboren am 27.07.1983 in Jena, Deutschland

Gutachter

1. Prof. Dr. Andreas Tünnermann, Jena, Deutschland
2. Prof. Dr. Markus Schmidt, Jena, Deutschland
3. Prof. Dr. William Wadsworth, Bath, Vereinigtes Königreich

Tag der Disputation: 15.06.2017

Contents

1	Introduction	1
2	Imaging Processes using Multiphoton Excitation and Coherent Raman Scattering	3
2.1	Multi-Photon Imaging (MPI)	3
2.2	Coherent Raman Imaging	5
2.2.1	Linear Raman Scattering	6
2.2.2	Coherent Raman Scattering	10
2.2.3	Stimulated Raman Scattering	14
2.2.4	Coherent Anti-Stokes Raman Scattering	15
3	Optimal Parameter Set of Laser Sources for Three-Photon Excited Fluorescence Imaging and Coherent Raman Scattering	18
3.1	Parameters for Coherent Raman Scattering Imaging Applications	18
3.1.1	Wavelength	18
3.1.2	Bandwidth	20
3.1.3	Laser Power and Phototoxicity	22
3.2	Coherent Anti-Stokes Raman Scattering Imaging	25
3.3	Stimulated Raman Scattering Imaging	26
3.4	Three-Photon Excited Fluorescence Imaging	29
4	Fundamentals of Optical Fibers	30
4.1	Optical Fibers and Photonic Crystal Structures	30
4.2	Waveguide Dispersion	32
4.3	Non-Linear Effects for Frequency Conversion in Optical Fibers	35
4.3.1	Self-Phase Modulation	35
4.3.2	Raman Scattering	36
4.3.3	Soliton-Self Frequency Shift	37
4.3.4	Four-Wave Mixing	39
4.3.5	Supercontinuum Generation	45
4.4	Active Fibers	45

4.5	Mode-Locked Lasers	47
4.6	Similariton Lasers	48
5	All-Fiber Widely Tunable Optical Parametric Oscillator	50
5.1	Narrow-Band Four-Wave-Mixing-Based Optical Parametric Oscillator	50
5.1.1	Passive Dispersive Filter	51
5.1.2	Reaching the Steady State	53
5.1.3	Tuning the FOPO	57
5.1.4	Influence of the Feedback Fiber Length	59
5.2	Temporal Walk-Off During Conversion	60
5.3	Influence of Self-Phase-Modulation Broadened Pump Pulses on the Conversion Process	62
5.4	Influence of the Pulse Shape on the Conversion Efficiency and Bandwidth	64
6	Implemented Laser Sources for Multi-Photon and Coherent Raman Scattering Imaging	68
6.1	Fiber OPO for CARS Imaging	68
6.2	Fiber OPO for Three-Photon Excited Fluorescence (3PEF) Imaging	76
6.3	Fiber OPO for SRS Imaging	85
6.3.1	Widely tuneable all-fiber FOPO for SRS	86
6.3.2	Linear Cavity FOPO	92
6.3.3	Application to CRS imaging	97
7	Conclusion	100
	Bibliography	102
	Appendix	110

1 Introduction

The progress in medicine, sanitation and overall prosperity has led to an increasing life-expectancy in developed countries. Consequently, degenerative and lifestyle-induced diseases, such as cardiovascular ones, Alzheimer's and certain types of cancer are the major cause of death in these countries today. As a result, the focus of bio-medical research has shifted towards early detection and treatment methods to mitigate the etiopathology of these degenerative diseases. However, their early diagnosis requires the detection of molecular perturbations on a microscopic scale, e.g. DNA mutations in the case of cancer. As a result, new imaging methods for a routine use in a medical environment are required.

Imaging methods based on coherent Raman scattering (CRS) are, nowadays, among the most potent techniques for a rapid visualization of the chemical composition of complex structures with sub-micrometer resolution. In particular, these methods are called Coherent anti-Stokes Raman scattering (CARS), stimulated Raman scattering (SRS) and the Raman induced Kerr effect (RIKE). All of these techniques have attracted great interest in the life and material science communities, since they are able to detect different molecules by their specific vibrational spectra. This potentially leads to label-free detection and fluorescence-free marking via small reporter molecules, e.g. alkyne tags or deuterated drugs. This intriguing feature, which has been known since the dusk of the last millennium, could not find routine usage outside specialized laser laboratories staffed with experienced laser scientists, because laser sources for CRS imaging are, even today, driven by large and complex laser setups. These systems are usually based on free-space lasers, where part of their radiation is converted in a free-space optical parametric oscillators. The light is either converted to a certain wavelength where multi-photon imaging (MPI) is beneficially operated at (e.g. 1250 nm) or the energy difference between two spectral features are tuned in a range of 1000 to 3000 cm^{-1} to enable CRS based imaging. Due to the unreliability and massive scale of such laser systems, there have been numerous attempts to create laser concepts, which are not only powerful enough, but also robust, compact and easy enough to use to bring these promising imaging technologies to real-world clinical environments.

Optical fibers, on the other hand, are a key technology which has enabled and contributed to the development of many fields of technology. High-speed communications and laser machining are two prominent examples, which were revolutionized by the fiber concept. Among their key advantages, in respect to other laser technologies, are reliability, maintenance-free operation and compact system footprints. Consequently, fiber technology might hold the key to the ultimate laser source driving CRS imaging.

This dissertation is devoted to exploring this possibility. First, a close look is taken at imaging processes based on multi-photon imaging in general and coherent Raman scattering in particular. Afterwards, in chapter 3, the demands for these non-linear imaging techniques and the optimal set of laser parameters is determined. Chapter 4 will lay the foundation, on which fiber laser sources can be constructed to enable internal conversion to the desired wavelength range needed to drive the addressed imaging techniques. The advantages of four-wave-mixing-based conversion is highlighted, since it the basis for the fiber based optical parametric oscillator (FOPO) described in Chapter 5, which is the core idea of this work. Here, its physical operation principle, implicit functionality and versatility are discussed. Chapter 6 describes the implementations of the FOPO for coherent anti-Stokes Raman scattering, stimulated Raman scattering and three-photon excited fluorescence, illustrating the advantages of this laser concept in contrast to other concepts. Finally, chapter 7 will conclude the work and give an outlook on how the technology could revolutionize medical surgery.

2 Imaging Processes using Multiphoton Excitation and Coherent Raman Scattering

2.1 Multi-Photon Imaging (MPI)

The excitation of fluorophores with multiple photons is called multi-photon excitation [1]. An intense laser beam is focused and scanned over a labeled specimen with a spot size smaller than $1\ \mu\text{m}$. If multiple photons are absorbed to excite a fluorescent marker, the emitted light can be collected and allocated to the present position of the scanner [2,3]. Therefore, a map of the fluorescent marker in the scanned focal plane can be created. As the laser focus has a well defined z-position and the fluorescent light may only emerge from the very focus of the beam, a three dimensional map of the sample can be generated by scanning multiple depths. This is an inherent advantage to bright field microscopy which, traditionally, only confocal scanning [4] or light sheet microscopy [5] offers. As the absorption of blood and water is weak in the near infrared, the excitation wavelengths can penetrate deep (up to $\sim 1.5\ \text{mm}$) into the tissue [6]. In section 3.1, the choice off the right wavelength range to work in will be discussed. As it has been already mentioned, the intensity of the exciting laser used for multi-photon imaging is so high that the probability for multiple photons to be absorbed at once becomes significant. The principle is depicted in figure 2.1. Two photons with wavelength λ_1 stimulate a fluorophores in its absorption band at E_{abs} . Subsequently, the fluorophor will release a fluorescence photon from its emission band E_{em} with a wavelength $> \lambda_1/2$. The same principle can be applied when three photons are absorbed by the fluorophor. In both cases the energy gap of the absorption band of the fluorescent marker has to be twice or three times the stimulation photon energy.

2. Imaging Processes using Multiphoton Excitation and Coherent Raman Scattering

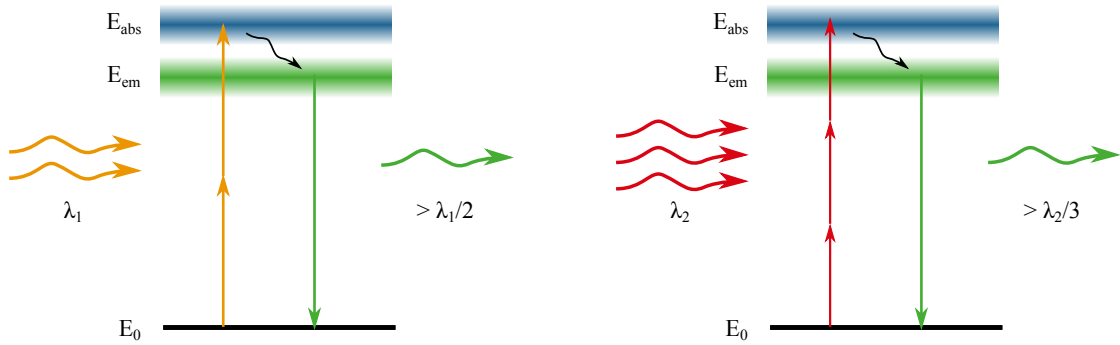


Figure 2.1: Energy diagram of two and three photon excited fluorescence.

By the use of ultra-short laser pulses (e.g. 100 fs pulse length) peak powers in the order of multiple Kilowatts can be easily generated by standard free-space oscillators. The peak power of a rectangular shaped laser pulse can be determined by $\hat{P} = \frac{E}{\tau}$, where E is the energy the laser pulse carries and τ the pulse length.¹ If these pulses are tightly focused with an high NA microscope objective, focal spots of down to 400 nm in diameter can be reached. This corresponds to a peak intensity of $1TW/cm^2$ which is high enough to enable three photon absorption of the fluorophores. Despite these huge intensities, the average power of such a laser with a pulse repetition rate in the range of 100 MHz is only ~ 20 mW. This example highlights the potential of ultra-short pulse lasers to produce high photon densities to trigger non-linear effects at low average powers to minimize photo-induced damage in the tissue. How to reach this kind of laser performance at the wavelengths needed for maximum tissue penetration from a compact fiber laser source is still an open issue. In chapter 3 the optimal parameters for a MPI source will be discussed before a generation method of such laser parameters will be introduced in chapter 4. The characterization of the resulting laser will be conducted in chapter 5 before the results of a real world laser source and the attained three photon excited fluorescence measurements are presented in chapter 6.

MPI requires intrinsic or extrinsic markers to identify different structures in the biological tissue. These markers can be poisonous to the specimen and/or alter the behavior of the system e.g. the metabolism. Therefore, researchers are looking for ways to visualize different chemical compounds without such markers. One way and possibly the most promising method is coherent Raman imaging (CRS). Thus the main effort of this work was devoted to construct a compact laser tailored to

¹This relation is exact for square pulse and does not differ significantly for e.g. Gaussian shaped pulses.

the needs of CRS imaging.

2.2 Coherent Raman Imaging

Contrary to multi-photon imaging, in coherent Raman imaging the chemical selectivity is not provided by extrinsic contrast agent (e.g. fluorescent marker). This label-free contrast comes from the inelastic scattering of photons off a molecule by either exciting or annihilating a molecular vibrational state. The shifted spectral lines are (due to the inelastic nature of the scattering) called Stokes and anti-Stokes signals. The number and position of the vibrational frequencies depend on the bond strength and the mass of the connected molecule section. Therefore, the energy signature is highly specific for each molecule, which makes Raman-based imaging a chemically differentiating method without the need for potentially toxic or functionality altering marker agents.

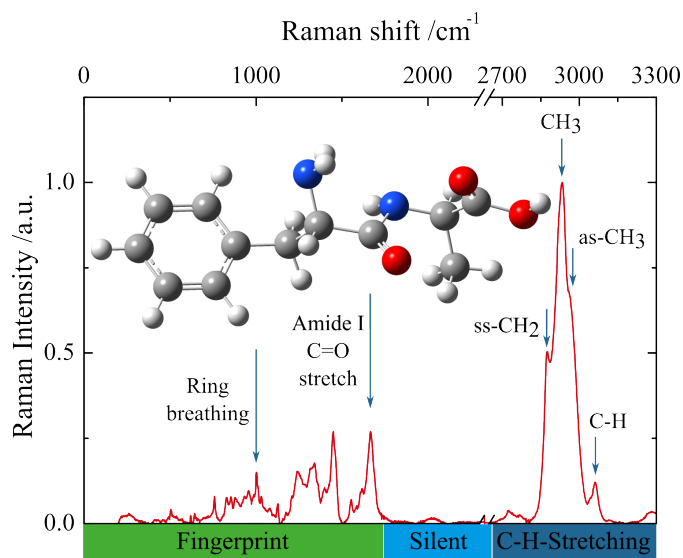


Figure 2.2: Structure and Raman shift spectrum of a dipeptide Pre-Ala molecule. [?]

Figure 2.2 depicts a dipeptide Pre-Ala molecule and its Raman shift spectrum in the so called fingerprint region, which contains tightly packed highly specific vibrational bands and a few characteristic bands of certain functional groups. Two of them are the benzene ring breathing vibration at $\sim 1000\text{ cm}^{-1}$ and the $C=O$ double bond of the peptide group at 1650 cm^{-1} . At higher wave-numbers $C-H$ stretching vibrations e. g. of the methylene groups at 2850 cm^{-1} and 2930 cm^{-1} can be found. Between those regions, only very few vibrations, of e.g. triple bonds, occur [7]. Hence, this part is called the silent spectral region. The energy signature of Raman

spectra of cells and biological tissues can be assigned to carbohydrates, nucleic acids, lipids and proteins. As cancerous tissue and other anomalies are accompanied by alterations in the composition, structure and concentration of molecules, Raman spectra provide a sensitive and highly specific indication of the type and the state of the specimen. In the following sub chapters the physical background of Raman scattering as a tool for bio-imaging is reviewed. Afterwards, two improvements of this method namely Stimulated Raman Scattering and Coherent anti-Stokes Raman scattering as fast, chemically sensitive imaging methods are introduced.

2.2.1 Linear Raman Scattering

The inelastic scattering of light on bound atoms is called Raman scattering. The interaction between the oscillation of the atoms in a molecular bond and the photons is mediated by the electrons, which are bound to the atoms.

The electric field of the light-wave moves charged particles with an oscillation frequency associated with its wavelength. As these frequencies are in the range of hundreds of THz , the nuclei are too inertial to follow adiabatically. Consequently, the interaction of the light field with the matter is dominated by the interaction with the electrons. The bound electrons are displaced, which induces an electric dipole moment: $\mu(t) = -e \cdot r(t)$, with e being the charge of the electron and $r(t)$ its displacement from the equilibrium positions. Close to the nucleus, the motion of a bound electron can be approximated by an harmonic oscillator. The resulting macroscopic polarization can then be obtained by summing up over the electric dipole density N :

$$P(t) = N\mu(t). \quad (2.1)$$

If the applied electric fields are weak compared to their binding fields, the polarization caused by the displacement follows directly the electrical field and can be written as

$$P(t) = \epsilon_0\chi E(t), \quad (2.2)$$

where ϵ_0 is the electric permittivity of vacuum and χ is the susceptibility of the material. If the intensity is increased and the displacement of the electrons becomes stronger, the binding potential of the electrons can no longer be correctly described as an harmonic oscillator. To describe the anharmonic motion of the electrons, the description of the polarization should be expanded by the inclusion of additional

2. Imaging Processes using Multiphoton Excitation and Coherent Raman Scattering

terms which are non-linearly dependent on the electrical field:

$$P(t) = \epsilon_0[\chi^{(1)}E(t) + \chi^{(2)}E^2(t) + \chi^{(3)}E^3(t) + \dots], \quad (2.3)$$

with $\chi^{(n)}$ being the n th order susceptibility. In order to generate observable third-order signals, which we will see later are needed for the Raman scattering process, the electrical field strengths of the driving fields can be much lower than the electrical field strength of the bound electrons. For biological imaging, for the intensity range of $10^{10}W/m^2$, the the third-order susceptibility is the dominating non-linear order. The second-order susceptibility is not occurring (or very weak) in isotropic materials like biological tissue and the intensity is not high enough to enable higher-order susceptibilities. The non-linear response is enhanced if the driving field is tuned to the electronic resonance of the material or molecule. Since these resonances are generated by the motion of the atoms, it can be said that the oscillating motion of the atoms in a molecular bond disturbs the polarizability of the electrons. Far from electronic resonances, the electronic dipole moment $\mu(t)$ is connected to the polarizability $\alpha(t)$ by the optical driving field $E(t)$ [8,9].

$$\mu(t) = \alpha(t)E(t) \quad (2.4)$$

For the theoretical case of a still standing atom, the polarizability is a time independent value α_0 . To include the vibration motion of the atoms one can expand α in a Taylor series:

$$\alpha(t) = \alpha_0 + \left(\frac{\delta\alpha}{\delta Q}\right)Q(t) + \dots, \quad (2.5)$$

where the term $\delta\alpha/\delta Q$ can be interpreted as the coupling strength of the nucleus to the electron motion. The motion of the atom core can be described as a harmonic oscillator by $Q(t) = 2Q_0\cos(\omega_\nu t + \Phi) = Q_0e^{i\omega_\nu t + i\Phi} + c.c.$, where Q_0 is the amplitude of the nuclear motion, ω_ν is the resonance frequency of the molecular bond and Φ its phase. If an optical wave $E(t) = Ae^{-i\omega_1 t} + c.c.$ (A is the amplitude of the electrical field, c.c. is the complex conjugate of the term in front) interacts with the bound atom, equation 2.4 becomes

$$\mu(t) = \alpha_0 Ae^{-i\omega_1 t} + A \left(\frac{\delta\alpha}{\delta Q}\right) Q_0 \left(e^{-i(\omega_1 - \omega_\nu)t + i\Phi} + e^{-i(\omega_1 + \omega_\nu)t - i\Phi}\right) + c.c. \quad (2.6)$$

The dipole moment of the electrons now oscillates at different frequencies. The first term describes Rayleigh scattering and the second term describes the generation of the Stokes and anti-Stokes frequencies at $\omega_1 - \omega_\nu$ and $\omega_1 + \omega_\nu$. The information

2. Imaging Processes using Multiphoton Excitation and Coherent Raman Scattering

of the vibrational frequencies of the molecular bonds are, therefore, transferred to the dipole moment of the electrons. Thus, the vibrational frequencies of the molecular bonds can be probed by a light field which scatters partially inelastically generating a so-called Raman shift equal to this frequency. This process can be depicted more simply by considering the energy states which are involved in the Raman scattering process. In this depiction, the pump photons emitted by the laser are exciting the ground state of the system to a so-called virtual state. This state has no lifetime and decays instantly. In the likely event that the system returns to its ground state a photon with the same amount of energy is released. This event is the well-known Rayleigh scattering process. If part of the energy is absorbed by exciting a higher vibrational state in one of the molecular bonds, the photon is red shifted and released. Therefore, the scattering process is described to be inelastic. The bond is left in an excited state and the photon is released in a random direction. If the excited energy state is absorbing another pump photon before it decays, the energy of the excited state is transferred to the pump photon and its photon energy increases. The radiated Raman shifted light can be calculated by the amplitude of the electrical field emitted by the oscillation dipole. The resulting time average of the Poynting flux can be integrated over the unit sphere to derive the overall intensity of the Raman shifted light:

$$I(\omega_s) = \frac{\omega_s^4}{12\pi\epsilon_0 c^3} Q_0^2 |A|^2 \left| \frac{\delta\alpha}{\delta Q} \right| \quad (2.7)$$

The intensity of the shifted light is linearly proportional to the intensity of the incident light $I = |A|^2$ and proportional to ω_s^4 . This wavelength dependence of the incident light is well known for Rayleigh scattering and is also true for Raman scattering. From an experimentalists point of view, it is convenient to define a cross section $\sigma(\omega_s)$ for the Raman scattering process, such that:

$$I(\omega_s) = Nz\sigma(\omega_s)I_0, \quad (2.8)$$

with N being the molecular density and z the interaction length. Depending on the cross sections of the different resonances, the likelihood of this process to occur is in the order of 10^{-8} . Consequently, the measurement of those events involve long integration times, high average powers and highly sensitive measurement equipment. This process is usually depicted by the involved energy states of the exciting laser and by the excited phonons (see fig. 2.3).

2. Imaging Processes using Multiphoton Excitation and Coherent Raman Scattering

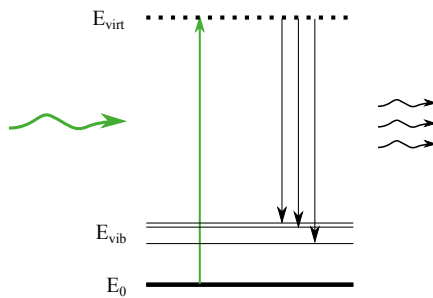


Figure 2.3: Energy diagram of the Raman scattering process. The virtual state E_{virt} is generated when an incoming photon is absorbed by the molecular bond. Then, different photon with different energies may be generated when the bond is not returning to its original state but a molecular vibration is excited. Depending on the energy of this state, the out-coming photon is red-shifted by this amount of energy.

The benefit of this technique is that the different Raman shifts are all excited simultaneously by the pump source and the scattering occurs only in dependence of the cross-sections of the molecular bonds and their concentration in the solution. To improve the scattering efficiency and, therefore, shorten the acquisition times for a certain signal to noise ratio, the process can be stimulated or seeded similar to the stimulated emission in the laser process or during seeded parametric conversion. The stimulation of the Raman scattering process leads to a higher conversion efficiency, which is then in the order of 10^{-4} . The amount of energy which is subtracted from the pump beam and added to the Stokes beam is, therefore, still extremely low. To detect this very small change, two solutions are possible: First, either the pump or the Stokes beam needs to be modulated to detect the change at the modulation frequency via lock-in detection of the other beam after conversion. This technique is called stimulated Raman scattering (SRS). The second method is to probe the excited molecular states by another probe photon, which will absorb the amount of stored energy of the excited molecular state and create the so-called anti-Stokes photons, which is spectrally separated from the pump and Stokes photon. This method is called coherent anti-Stokes Raman scattering (CARS). Both processes yield a much higher signal (which allows for a much faster detection) than the linear Raman scattering process but need sophisticated lasers in order to run efficiently. In the following sections both techniques are explained in depth.

2.2.2 Coherent Raman Scattering

During linear Raman scattering, the molecule is addressed by an input field, which is far from a molecular resonance. In this case, the initial phase of the Raman oscillation is random and is, therefore, said to be spontaneous and incoherent. If together with the pump field, a Stokes field is added to stimulate the scattering process, the phase of the scattered waves is determined by the phase of the incoming fields. Therefore, SRS and CARS produce coherent signals.

The light field which acts on the vibrational motion of the bound nuclei is given by $E_i(t) = A_i^{-i\omega_i t} + c.c.$ where $i=1,2$ is referring to the pump and Stokes fields. The external force exerted by the incoming light fields is:

$$F(t) = \left(\frac{\delta\alpha}{\delta Q} \right)_0 [A_1 A_2^* e^{-i\Omega t} + c.c.], \quad (2.9)$$

where the frequency difference between the pump and Stokes field is $\Omega = \omega_1 - \omega_2$. The nuclear displacement can be then described by a damped harmonic oscillator model [10]:

$$\frac{d^2 Q(t)}{dt^2} + 2\gamma \frac{dQ(t)}{dt} + \omega_\nu Q(t) = \frac{F(t)}{m}, \quad (2.10)$$

where γ is the damping constant and m is the reduced mass of the nuclear oscillator. The resulting oscillation of the nuclei is then: $Q(t) = Q(\omega_\nu) e^{i\Omega t} + c.c.$ with the amplitude

$$Q(\omega_\nu) = \frac{1}{m} \left(\frac{\delta\alpha}{\delta Q} \right)_0 \frac{A_1 A_2^*}{\omega_\nu^2 - \Omega^2 - 2i\Omega\gamma}. \quad (2.11)$$

It is obvious that the amplitude of the oscillation is large if the frequency difference of the driving light fields Ω is the same as the oscillation frequency ω_ν of the molecular bond. The absolute frequency of the pump and Stokes fields does not influence the amplitude of the scattered light and can be chosen according to other aspects as discussed in chapter 3.1.1.

The oscillation of the nuclei causes an altered electronic polarizability of the material. The electronic fields of the incoming light E_1 and E_2 experience this change by the effective macroscopic polarization in the material, which can be described as the sum of the dipole moments (see eq. 2.1). By using the equations 2.1, 2.4 and 2.5, the polarization can be written as:

$$P(t) = N \left[\alpha_0 + \left(\frac{\delta\alpha}{\delta Q} \right)_0 Q(t) \right] \{E_1(t) + E_2(t)\} \quad (2.12)$$

The terms which depend on α_0 correspond to the linear polarization, which is

2. Imaging Processes using Multiphoton Excitation and Coherent Raman Scattering

independent of the oscillation of the atom cores, whereas the terms linear to $(\frac{\delta\alpha}{\delta Q})_0$ correspond to the third-order polarization. These terms are dependent on the nuclei movement and contribute to the nonlinear polarization

$$P_{NL} = P(\omega_{cs})e^{-i\omega_{cs}t} + P(\omega_2)e^{-i\omega_2t} + P(\omega_1)e^{-i\omega_1t} + P(\omega_{as})e^{-i\omega_{as}t}, \quad (2.13)$$

with the frequencies: $\omega_{cs} \equiv 2\omega_2 - \omega_1$, the coherent Stokes frequency and $\omega_{as} \equiv 2\omega_1 - \omega_2$, the coherent anti-Stokes frequency. The resulting nonlinear polarization, therefore, consist of contributions which oscillate at the driving frequencies ω_1 and ω_2 (see figure 2.4a), as well as at the newly generated frequencies ω_{cs} and ω_{as} (see figure 2.4(b)). The energy diagram in figure 2.4(c) depicts possible non-linear interactions of the driving fields with the vibrating molecular bond at the frequency Ω . The first panel shows the generation of the coherent Stokes generation: An excited vibration absorbs a photon with the frequency ω_2 . A so-called virtual state (at the energy level $E_{virt,2}$) is generated, which is depleted instantaneously by a photon of the second light field with the frequency ω_1 to the ground state. A second photon at ω_2 is absorbed by the system bringing it to the virtual state at the energy level $E_{virt,1}$. This state can then radiate the so-called coherent Stokes photon at ω_{cs} . The whole process is called coherent Stokes Raman scattering (CSRS). The second panel in 2.4(c) depicts stimulated Raman gain (SRG) and stimulated Raman loss (SRL). Here, the driving fields ω_1 and ω_2 excite a vibrational mode in the system via the virtual state $E_{virt,2}$. In this path part of the photons of the driving field at ω_1 are converted to photons at ω_2 , which are than added to the corresponding field. The difference energy is remaining as the excited phonon in the system. The last panel describes the excitation of the virtual state at $E_{virt,2}$ and the depletion of this state to excite the vibrational state of the atoms, while releasing a photon at ω_2 . This state is excited by another photon at ω_1 , bringing the system to the virtual energy level $E_{virt,3}$. From this state the so-called Anti-Stokes photon is released to bring the system to its ground state. The overall process is called coherent anti-Stokes Raman scattering (CARS) and will be subject of the chapter 2.2.4.

2. Imaging Processes using Multiphoton Excitation and Coherent Raman Scattering

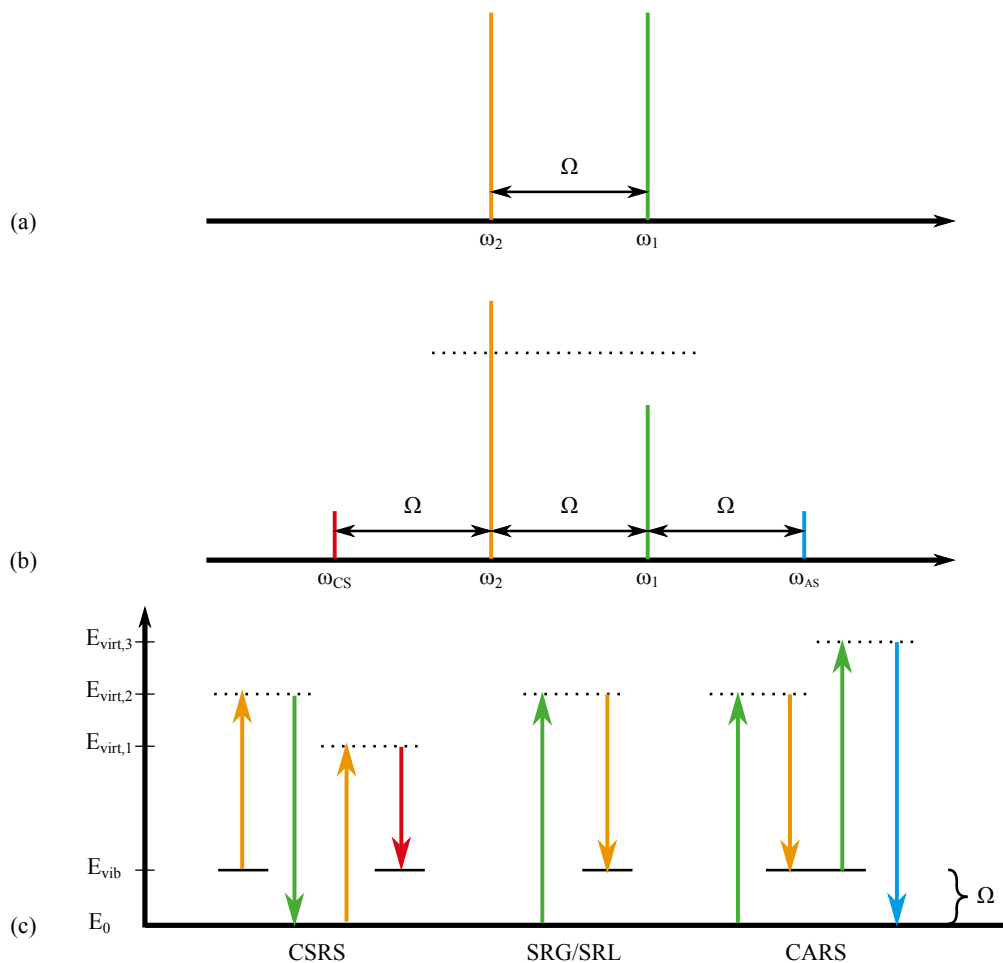


Figure 2.4: Spectrum and energy diagrams of the Coherent Raman scattering processes. (a) The incoming light fields at frequency ω_1 and ω_2 with the frequency difference $\omega_1 - \omega_2$ are in resonance with the frequency Ω of the atomic oscillation. (b) The frequency components after non-linear scattering. The dotted lines represents the level of the incoming light fields in (a). (c) Energy diagrams of the possible non-linear conversion paths. Here, the dotted lines mark the energy levels of the virtual states.

The amplitude of the polarization for the different frequencies in equation 2.13 can be written as [8]:

$$P(\omega_{cs}) = 6\epsilon_0\chi_{NL}^*(\Omega)A_2^2A_1^* \quad (2.14)$$

$$P(\omega_2) = 6\epsilon_0\chi_{NL}^*(\Omega)|A_1|^2A_2 \quad (2.15)$$

$$P(\omega_1) = 6\epsilon_0\chi_{NL}^*(\Omega)|A_2|^2A_1 \quad (2.16)$$

$$P(\omega_{as}) = 6\epsilon_0\chi_{NL}^*(\Omega)A_1^2A_2^* \quad (2.17)$$

2. Imaging Processes using Multiphoton Excitation and Coherent Raman Scattering

with the nonlinear susceptibility:

$$\chi_{NL}(\Omega) = \frac{N}{6m\epsilon_0} \left(\frac{\delta\alpha}{\delta Q} \right)_0^2 \frac{1}{\omega_\nu^2 - \Omega^2 - 2i\Omega\gamma}. \quad (2.18)$$

To determine the parameters which influence the intensity of the SRL, SRG and CARS signals, the non-linear polarization term has to be inserted into the nonlinear wave equation:

$$\nabla^2 \mathbf{E} - \frac{n^2}{c^2} \frac{\partial^2}{\partial t^2} \mathbf{E} = \frac{1}{\epsilon_0 c^2} \frac{\partial^2}{\partial t^2} \mathbf{P}_{NL} \quad (2.19)$$

as a source term in order to solve for the nonlinear field \mathbf{E} . [8] To simplify the calculation, we approximate the light fields within the interaction length of the focused beams as plane waves. In this approximation the different driving fields can be written as:

$$E_j(z, t) = \frac{1}{2} \left(A_j(z) e^{i(k_j z - \omega_j t)} + c.c. \right) \mathbf{x}, \quad j = 1, 2, 3, \quad (2.20)$$

where \mathbf{x} is the orientation vector of the E-field, which is orthogonal to the propagation direction of the plane waves. The $k_j = \omega_j n_j / c$ is the scalar wave vector and j identifies the different incident waves. The resulting amplitude A_4 of the resulting field E_4 can be derived by using the slowly varying envelope approximation [11] and by integration over the interaction length L :

$$A_4(L) \sim i\chi_{NL}(\Omega) A_1 A_2^* A_3 L \text{sinc} \left(\frac{\Delta k L}{2} \right) e^{i\Delta k L / 2}. \quad (2.21)$$

For CARS, where the first and third fields are usually identical, the intensity of the generated anti-Stokes field scales as:

$$I(\omega_{as}) \sim |A_{AS}(L)|^2 \sim |\chi_{NL}(\Omega)|^2 I_1^2 I_2 L^2 \text{sinc} \left(\frac{\Delta k L}{2} \right). \quad (2.22)$$

For SRS where the scattering of the light field at ω_1 is stimulated by the field at ω_2 :

$$A_2^{stim}(L) \sim i \{ \chi_{NL}(\Omega) \}^* A_1^* A_2 A_1 L \quad (2.23)$$

The change in intensity of the incident light at ω_2 at the resonance Ω can be calculated from the interference with the remaining field:

$$\Delta I(\omega_2) \sim 2 \text{Im} \{ \chi_{NL}(\Omega) \} I_1 I_2 L. \quad (2.24)$$

This change represents the stimulated Raman gain, which is linearly dependent on the interaction length and the intensities of the light fields at ω_1 and ω_2 . The same approach can be used to determine the change of intensity of the first light field at ω_1 , which is called the stimulated Raman loss:

$$\Delta I(\omega_1) \sim -2\text{Im} \{ \chi_{NL}(\Omega) \} I_1 I_2 L. \quad (2.25)$$

So far, the theoretical background about the origin of CRS and the signal dependence of SRS and CARS on the main laser parameters has been established. In the following two sections the consequences for a practical implementation of these two modalities for chemically resolved imaging will be discussed.

2.2.3 Stimulated Raman Scattering

In order to conduct chemically sensitive measurements via SRS, a laser source, which delivers two different wavelengths, is focused onto a sample. The wavelength λ of the light is connected to the oscillation frequency of the E field by $\omega = \frac{2\pi c}{\lambda}$. If the wavelength difference of the two colors matches a molecular bond vibrational frequency, part of the incoming light at ω_1 is shifted to the second field at ω_2 (for $\omega_1 > \omega_2$). In order for SRS to work efficiently for tightly focused beams, the power of the laser has to be in the range of 1 kW. To prevent photo-induced damage, the lasers have to be pulsed to reach these power levels (over a short time) at a moderate average power. The issue of phototoxicity will be discussed in chapter 3.1.3. Still, the interference of the stimulated Raman loss and gain with the driving fields at ω_1 and ω_2 causes only little changes in intensity. In order to detect these small changes, lock-in detection needs to be applied. The lock-in detection works by modulating one of the driving pulse trains with a frequency which is lower than the pulse repetition rate. After the SRS process the non-modulated pulse train carries the SRS signal at the modulation frequency. It is detected by a photo-diode and can be separated by electronic filtering from the signal (see figure 2.5).

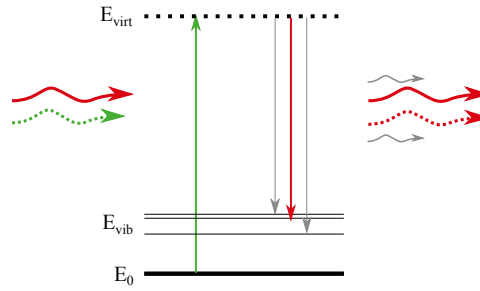


Figure 2.5: Energy diagram of the stimulated Raman scattering process. Depicted are the two driving fields, where the pulse train of the laser with the higher photon energy (green arrow) is modulated (dotted arrows). For the instances where both fields are present and interact with the molecular bond, the modulated pump pulse train is scattered on the bond and loses part of its photon energy in the process. It becomes part of the field with the lower photon energy (red arrows) which represents a small change compared to its overall intensity. The gray arrows represent the spontaneous Raman scattering emission which are many orders of magnitude more unlikely than the stimulated emission..

A pre-requisite for this detection method to work is a laser with an extremely low noise figure at the modulation frequency. Noise at the modulation frequency of the non-modulated beam will burrow the signal and will require long integration times to extract it. The noise issue will be discussed in chapter 3.3. The optimal parameters of the wavelength range in which the laser should operate, the pulse length, repetition rate and required output power will be discussed in the same place.

2.2.4 Coherent Anti-Stokes Raman Scattering

In section 2.2.2, the dependence of the signal intensity on the peak powers of the driving fields of SRS and CARS has been established (equations 2.22, 2.24 and 2.25). It is apparent that the degree of non-linearity is higher for CARS and that it is quadratically dependent on the intensity of the pump field (that with the highest photon energy). The energy diagram in figure 2.6 depicts the conversion path of the CARS process. The anti-Stokes signal component is spectrally separated from the rest of the driving fields, which can be filtered out by high-contrast spectral filters. The detection of the signal is, in comparison, straightforward and it is usually done with a highly sensitive photo-multiplier.

2. Imaging Processes using Multiphoton Excitation and Coherent Raman Scattering

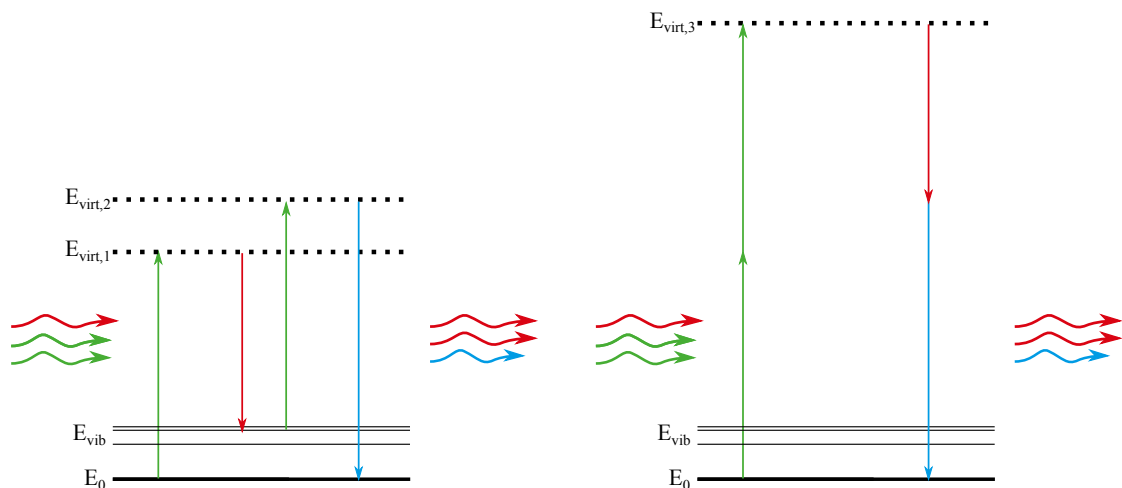


Figure 2.6: Energy diagram of the coherent anti-Stokes Raman scattering (CARS) process and origin of the non-resonant background. The photons with the higher photon energy (the “pump”, green) and the coincident driving photon with the lower energy (the “Stokes”, red) cause the stimulated excitation of a molecular bond if the frequency difference of the pump and the Stokes match the bond vibrational frequency. Then, if another high energy photon (the “probe”) is absorbed it will cause the depletion of this excited molecular bond while releasing an “anti-Stokes” photon (marked in blue). The right-hand side diagram describes an alternative route to generated a signal that overlaps with the anti-Stokes photon without the aid of a molecular state. In this case two pump photons are converted to signal and idler photons, which cause a non-specific background for the anti-Stokes.

Equation 2.22 describes this conversion path but also includes a different possibility to generate a signal at this frequency. If $\chi_{NL}(\Omega)$ is divided in its real and imaginary parts, the spectral behavior $S(\Omega)$ of the anti-Stokes component $I(\omega_{as})$ can be written as:

$$S(\Omega) \sim |\chi_{NL}(\Omega)|^2 = |\chi_{NR}^{(3)}|^2 + |\chi_R^{(3)}(\Omega)|^2 + 2\chi_{NR}^{(3)} \text{Re} \left\{ \chi_R^{(3)}(\Omega) \right\}.$$

The spectrum of the non-linear response can hence be written as the sum of a non-resonant background ($\chi_{NR}^{(3)}$), the resonant term ($\chi_R^{(3)}(\Omega)$) and the interference term $2\chi_{NR}^{(3)} \text{Re} \left\{ \chi_R^{(3)}(\Omega) \right\}$ [12]. The line shape resembles the behavior of a driven oscillator and is depicted in figure 2.7(a). The red line represents the line shape of the imaginary part of $\chi_{NL}(\Omega)$ which is the lineshape of the spontaneous Raman process. Its amplitude is plotted versus the detuning of the energy difference of the pump and Stokes fields in respect to the resonance frequency of the molecular bond. The blue line represents the real part of $\chi_{NL}(\Omega)$. The linewidth of the resonance was set to 5 cm^{-1} and the ratio of the resonant to the non-resonant term was set

2. Imaging Processes using Multiphoton Excitation and Coherent Raman Scattering

to unity.

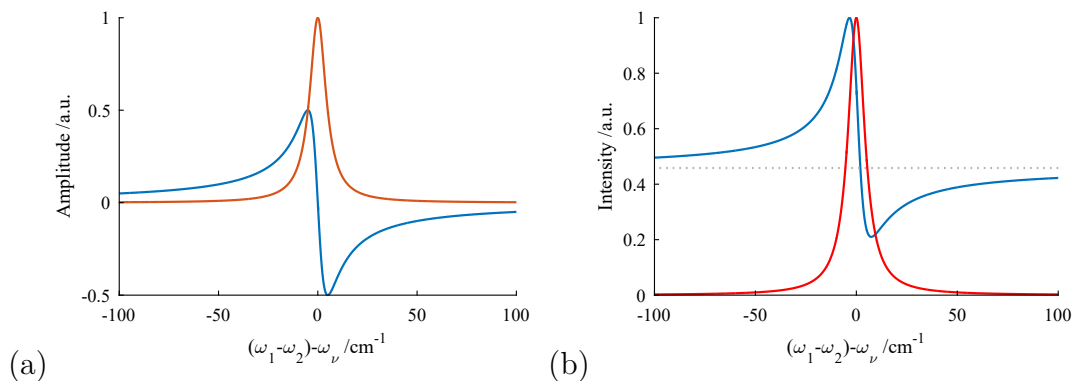


Figure 2.7: Spectral response of the CARS process on a resonance with a linewidth of 5 cm^{-1} . (a) Imaginary (blue) and real (red) part of $\chi_{NL}(\Omega)$. (b) CARS lineshape $S(\Omega)$ (red) with non-resonant background (dotted gray line) in comparison to the linear lineshape (red)

The resulting spectral response of the CARS signal is significantly different compared to a narrow Raman line. Firstly, there is the non-resonant background caused by quantum pathways which contribute to the anti-Stokes radiation but do not contain propagators at $\omega_1 - \omega_2$ (see figure 2.6 right panel). Secondly, the line peak is shifted by a few cm^{-1} (compare the positions of the peaks of the red and blue curve) and lastly, the shape differs strongly as the interference term causes constructive and destructive interference of the real part of $\chi_{NL}(\Omega)$ with the non-linear background. In the case of overlapping resonances, the spectrum becomes quite complicated and difficult to compare to the linear Raman spectrum. Also, the contrast of the anti-Stokes radiation is limited by the presence of the non-resonant background. In the depicted situation (figure 2.7), where the non-resonant background is as strong as the resonant one, the spectral contrast is quite poor. For stronger resonances or a weaker non-linear background radiation, the lineshape quickly becomes close to the linear Raman shape again. Therefore, CARS is very well suited for strong resonances but becomes difficult to interpret if the resonances are weak and tightly spaced.

It was assumed that the excitation fields are narrowband. To gain information about many resonances at once, the Stokes field may be broadband in order to excite many resonances simultaneously [13]. In general, the detection of the anti-Stokes generation has to be spectrally resolved. However, the integration time and sensitivity of spectrometers are orders of magnitude longer than a photo multiplier. Therefore, to reach video rate acquisition times, single-band excitation (single-band CRS) needs to be used.

3 Optimal Parameter Set of Laser Sources for Three-Photon Excited Fluorescence Imaging and Coherent Raman Scattering

In this chapter, the optimal parameters for three-photon excited fluorescence (3PEF) imaging and coherent Raman scattering are deduced. Based on this knowledge, a suitable fiber-based laser concept will be introduced in chapter 5 and the experimental results and application to non-linear imaging will be presented in chapter 6.

3.1 Parameters for Coherent Raman Scattering Imaging Applications

Before the optimal parameters for CARS, SRS and multi-photon imaging (MPI) are deduced, the common requirements for wavelength, bandwidth and laser power for CRS imaging will be explored. Except for the bandwidth requirements, these findings are also true for MPI. In the following part, specific requirements for each of the imaging modalities will be established.

3.1.1 Wavelength

One of the most important aspects of non-linear imaging is the possibility to scan the tissue three-dimensionally as it was introduced in section 2.1. In order to maximize the achievable penetration depth, absorption and scattering in the tissue have to be minimized. The absorption in typical biological material is limited by the absorption of water and hemoglobin. The highest transparency of both materials is found in the wavelength range of 600 to 1400 nm and around 1700 nm.

3. Optimal Parameter Set of Laser Sources for Three-Photon Excited Fluorescence Imaging and Coherent Raman Scattering

Therefore, all of the photons should be in this range since, otherwise, heating caused by absorption could destroy the sample. The spectral range from 600 to 1400 nm spans 9500 cm^{-1} , which is broad enough to encompass all biochemically relevant Raman shifts. Figure 3.1 shows exemplarily the pump and Stokes within the spectral window for a typical application of multiplex (a) and single frequency (b) CARS.

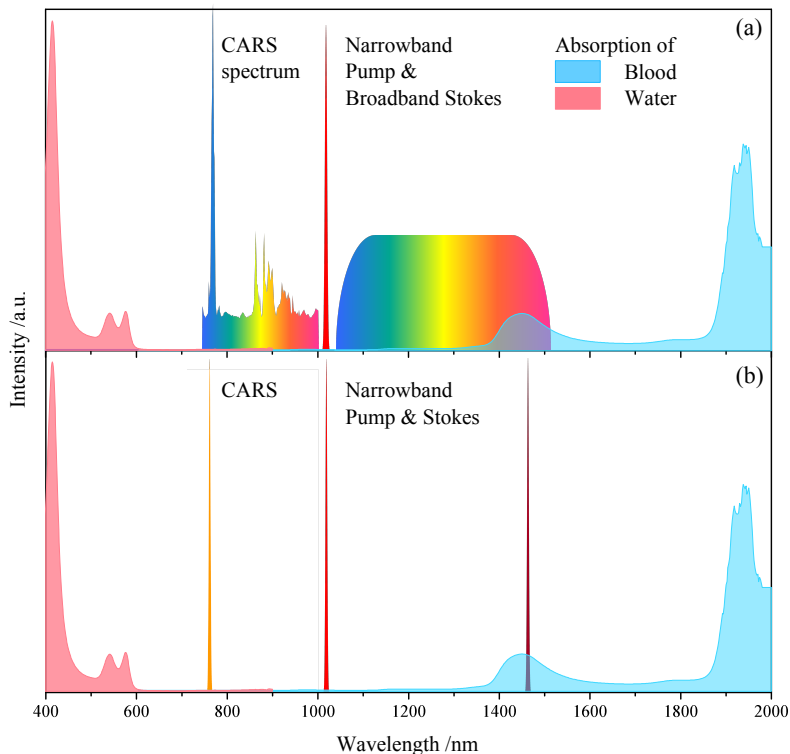


Figure 3.1: (a) Example of multiplex CARS and single frequency CARS within the spectral work space given by the absorption of water and hemoglobin. [14]

In this spectral range, the losses are dominated by Rayleigh scattering. Rayleigh scattering losses are proportional to ω^4 and, therefore, photons with shorter wavelengths are scattered much more strongly than photons in the near infrared. Furthermore, the non-linear absorption of multiple photons leads to a strong absorption in the UV. Thus, non-linear imaging techniques, in which the peak power of the light is high enough to cause such an interaction, benefits from longer wavelengths. On the other hand, the spot size increases at longer wavelengths and there is a limited availability of high NA, NIR-corrected microscope objectives. Therefore, the wavelength range around $1\text{ }\mu\text{m}$ is a trade-off between low scattering losses, non-linear absorption, spatial resolution and the availability of optical glasses and components.

3.1.2 Bandwidth

The spectral resolution of the CARS and SRS processes is determined by the spectral bandwidth of the pump and Stokes laser pulses [15]. In the case of single band CRS, the convolution of both bandwidths determines the spectral resolution of the measurement. Therefore, both driving pulses (pump and Stokes) have to be narrowband in order to reach a high spectral resolution (and with it a high chemical resolution). In figure 3.2 a spectral CARS scan in the CH- stretching range of 2750 to 3000 cm^{-1} with a spectral resolution of 1 cm^{-1} is compared to the same measurement with a simulated spectral resolution of 5 and 10 cm^{-1} .

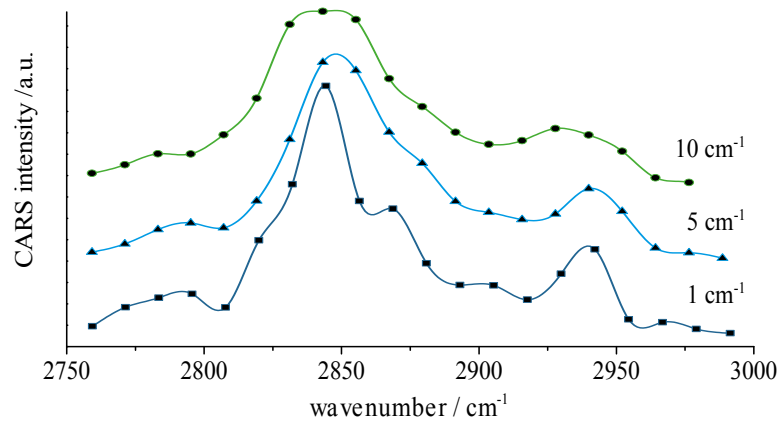


Figure 3.2: Spectral CARS signal sweep for different resolutions. [16]

It is clearly visible that the contrast between the different lines is much better at the highest resolution. Especially in the fingerprint region, where the Raman bands are much closer together, spectral resolutions below 5 cm^{-1} are preferable. For isolated Raman lines, the non-resonant background in a CARS measurement increases linearly with the spectral width of the driving pulses. Thus, in order to increase the contrast to the non-resonant background, the bandwidth of the lasers has to be as narrow as possible [17]. Even though SRS does not suffer from the non-resonant background in the same way as CARS does, a wideband excitation results in a lower signal yield as only a (small) part of the bandwidth of the pump and Stokes pulses are contributing to the SRS process. The advantage of CARS imaging with narrowband excitation is depicted in figure 3.3.

3. Optimal Parameter Set of Laser Sources for Three-Photon Excited Fluorescence Imaging and Coherent Raman Scattering

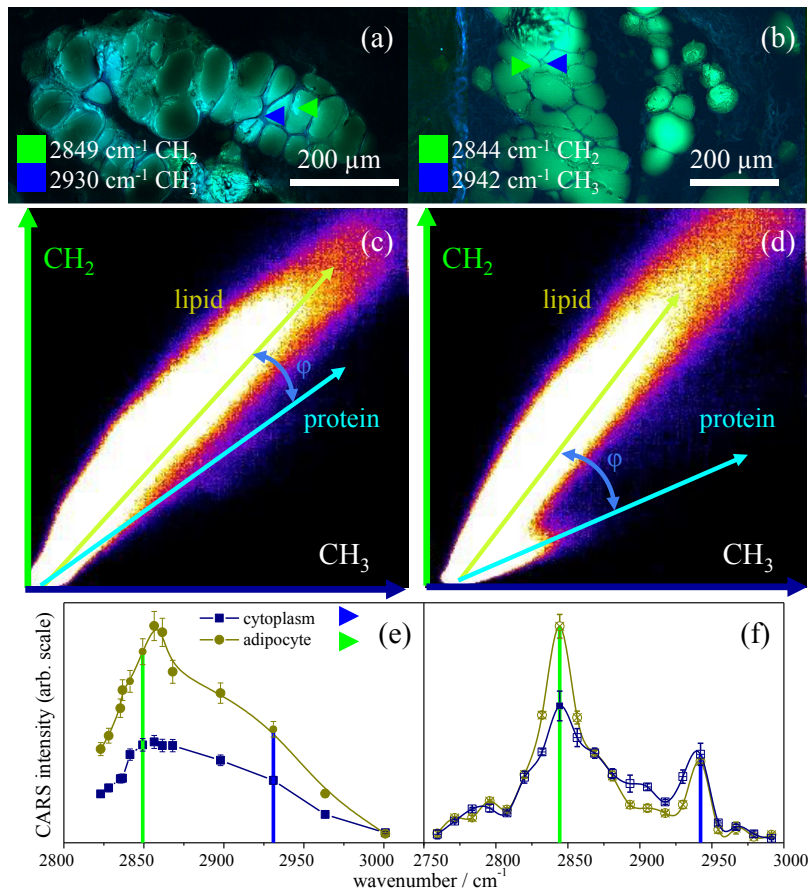


Figure 3.3: Contrast advantage of high spectral resolution CARS imaging at 30 cm^{-1} (a) and 1 cm^{-1} (b). The CARS data from protein and lipid structures can be plotted in a two-color CARS image at the C–H stretching resonance of CH_3 (2930 cm^{-1} , blue) and CH_2 (2850 cm^{-1} , green). The spectral separation of the components is determined by the separation angle φ in the frequency scatter plots (c) and (d). This separation is significantly increased for CARS with narrowband excitation (d). Consequently, high spectral resolution increases the signal-to-noise ratio and allows for a lower detection limit. Finally, the last row shows the resulting CARS spectra of lipid droplets and cytoplasm of adipocytes measured at 30 cm^{-1} (e) and 1 cm^{-1} of spectral resolution (f) [14].

The chemical sensitivity of CARS microscopy is demonstrated by imaging adipocytes and collagen fibers of the connective tissue surrounding an artery at 30 cm^{-1} in panel 3.3(a) and at 1 cm^{-1} spectral resolution in panel 3.3(b). Two CARS images with an energy difference of the pump and Stokes wavelength of 2850 cm^{-1} (green) and 2930 cm^{-1} (blue) were overlaid. These resonances correspond to the characteristic CH-stretching vibrations of the methylene and methyl groups, respectively. Since the CARS signal intensity ratio of 2930 cm^{-1} and 2850 cm^{-1} is higher in proteins, areas where the protein density is high appear blueish, whereas lipid-rich areas appear green. Even if both images allow for the discrimination of

protein and lipids, the separation of both substances is significantly higher in the 2D-histograms of panels (a) and (b), i.e. in panels (d) and (c). This is indicated by the larger separation angle φ . In addition, the CARS spectra depicted in panels (e) and (f) (acquired by tuning the frequency difference from pump and Stokes at the locations indicated by arrows in (a) and (b)) are significantly better for the high spectral resolution light source. Hence it can be concluded, that a high spectral resolution of 1 cm^{-1} in comparison to 30 cm^{-1} resolution is also beneficial for resolving spectrally broad resonances in the C-H-stretching region. High spectral resolution imaging results in a lower detection limit and in a better discrimination of molecular markers, e.g., protein and lipids. A spectral resolution of 1 cm^{-1} corresponds to transform-limited Gaussian pulses of about 15 ps the wavelength region of $1\text{ }\mu\text{m}$.

3.1.3 Laser Power and Phototoxicity

The main limiting factor to achieve the highest signal-to-noise ratio during a measurement, or to achieve the fastest acquisition rate, is the phototoxicity. This has to be considered when choosing the wavelength, repetition rate, peak and average power of the laser source. There have been many studies aimed to at finding the nature of photo damage in living cells and its dependence on laser power [18–22]. The damage threshold at which the photo-induced destruction is likely to occurs is:

$$D = \hat{P}^n f_{Rep} \tau, \quad (3.1)$$

where \hat{P} is the peak power of the laser, f_{rep} the pulse repetition rate and τ the duration of the laser pulses. The exponent n depends on the non-linearity of the damage. If $n=1$, the damage is purely due to the average power of the laser, which means that the damage is related to the accumulated heat within the laser beam focus. For $n>2$ the damage is originating from multi-photon absorption. In this case two or more photons are absorbed by the medium. Together they excite an electronical state which causes chemical bonds to break and ultimately destroy the tissue. Therefore, these damage effects are highly dependent on the peak power and the pulse duration of the laser. It has to be noted that all of the peak power values depend heavily on the focus size. In case of biological imaging, we assume tight focusing and numerical apertures approaching 1. Fu et. al. [23] found in an CARS experiment that for $\hat{P}_{pump} = 74\text{ W}$ and $\hat{P}_{Stokes} = 23\text{ W}$ at a repetition rate of $f_{rep} = 3.9\text{ MHz}$, a NA of the objective of 1.2 and a pulse duration of $\tau_{pulse} = 2.5\text{ ps}$, damage effects are mostly linear ($n=1$). By increasing the peak powers to 277 W

3. Optimal Parameter Set of Laser Sources for Three-Photon Excited Fluorescence Imaging and Coherent Raman Scattering

and 86 W respectively, n increased to 1.8. Here the pump wavelength was fixed at 701 nm and the Stokes wavelengths were shifted from 843 to 888 nm. From this experiment, a lower threshold for the onset of damage effects can be set if the pump and Stokes wavelengths are shifted further into the infrared, as the linear absorption and also the multiphoton absorption is reduced at longer wavelengths around 1 μm . Hopt et. al. [18] used very short pulses (< 200 fs) and peak-powers of 200 W for multi-photon experiments pumped at 800 nm. In this case, n increases to 2.5.

The signal strength for CARS microscopy is (compare to equation 2.22):

$$P \sim \hat{P}_{pump}^2 \hat{P}_{Stokes} \tau_{pulse} f_{rep} \quad (3.2)$$

and for 3PEF:

$$P_{3PEF} \sim \hat{P}_{pump}^3 \tau_{pulse} f_{rep}. \quad (3.3)$$

Hence, both of these imaging modalities are dependent on the peak power to the power of three. Thus, since the damage D depends on the exponent n in the range of 1...2 for picosecond excitation and up to 2.5 for sub-picosecond excitation, the only way to maximize the signal strength for a given damage threshold D is to decrease the repetition rate f_{rep} and pulse duration τ_{pulse} [20–22,24] while increasing the pump and/or Stokes peak power. As the studies show, reducing the pulse duration is not very effective as it also increases the exponent n in the damage threshold equation 3.1. For CRS microscopy, the length of the pulse plays a crucial role, since it is inverse proportional to the minimal bandwidth a pulse can have. This relation is called the time-bandwidth product and it is: $\tau_{pulse} \geq 0.44/(\Delta\nu c)$, for Gaussian pulses with the FWHM (full width half maximum) bandwidth $\Delta\nu$. If the pulse duration becomes very short, the spectral bandwidth increases to a point where their it broader than the Raman bands. Consequently, the pulse width of the driving laser defines the maximal spectral resolution and contrast between two adjacent Raman lines that CRS microscopy can have [16]. In contrast, reducing the repetition rate allows higher pump and Stokes peak powers, which ultimately leads to higher signal strengths at the same phototoxicity level D . Figure 3.4 depicts the signal power P in the case of CARS microscopy at a constant damage threshold D for different CARS resolutions and repetition rates for transform-limited pulses plotted versus their bandwidth.

3. Optimal Parameter Set of Laser Sources for Three-Photon Excited Fluorescence Imaging and Coherent Raman Scattering

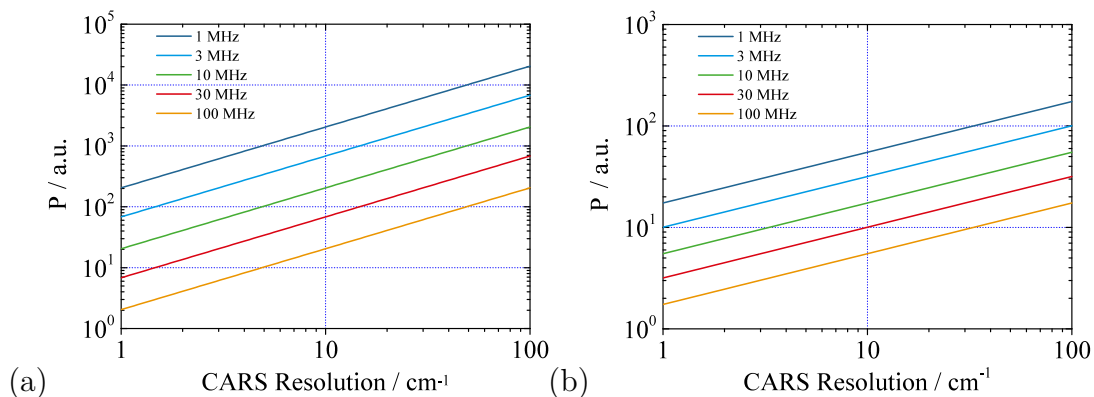


Figure 3.4: Signal strength P for Damage threshold exponents $n = 1$ and (b) $n = 2$

As the resolution in CRS microscopy should be better than 10 cm^{-1} to resolve closely spaced resonances with a high contrast, the pulse duration should be at least a few picoseconds. Depending on the exponent n in the damage threshold equation (between 1 and 2), the difference in signal power P in a CARS experiment pumped by a laser at 100 MHz and 1 MHz is a factor of 10 to 100 different. This means that at moderate peak powers, it is always better to choose the lowest possible laser repetition rate, in order to reach high signal strengths and spectral resolution at the same time. Of course, for high speed imaging the repetition rate also defines the minimum pixel acquisition rate. If the laser scanning microscope is synchronized to the laser and for each pixel only one laser pulse excites the sample, a video rate acquisition of 10 frames per second at a resolution of 500x500 pixel is possible with 2.5 MHz of pulse repetition rate. Compared to a standard free-space OPO with a repetition rate of 80 MHz, a signal increase of 5.6 dB at the same damage level ($n = 2$) can be expected. Alternatively, the bandwidth of the pump and Stokes pulses can be decreased in order to enhance the resolution of the CARS process. In this case, both the bandwidth and the repetition rate may be lowered by 5.6 dB to achieve the same signal intensity compared to an excitation with 80 MHz. As the pulse length increases by the same amount, the exponent n in the damage threshold equation also decreases. Therefore, by using pulses in the order of tens of picoseconds, higher pump and Stokes pulse peak powers can be used without causing photo-induced destruction of the tissue. In the end, the optimal repetition rate and pulse duration is determined by the desired pixel acquisition rate and chemical resolution.

SRS has a lower degree of non-linearity and, therefore, has to be treated differently (compare with 2.24 and 2.25).

$$P_{SRS} \sim \hat{P}_{pump} \hat{P}_{Stokes} \tau_{pulse} f_{rep}. \quad (3.4)$$

3. Optimal Parameter Set of Laser Sources for Three-Photon Excited Fluorescence Imaging and Coherent Raman Scattering

Depending on the exponent in the damage equation 3.1, the repetition rate of the laser should be either high ($n > 2$), does not have an effect ($n = 2$) or should be as low as possible ($n > 2$). As it has been shown earlier, n rises above 2 for very short pulses ($\tau_{pulse} < 1$ ps). In this case SRS would benefit from high repetition rates. It has also been established that for good chemical specificity and signal strengths, SRS should be driven with narrowband pump and Stokes pulses ($\Delta\nu < 5$ cm^{-1}). Therefore, the non-linearity of the damage should be lower than 2, which favors low repetition rates. Compared with CARS and MPI imaging, however, this effect is very small.

3.2 Coherent Anti-Stokes Raman Scattering Imaging

After the discussion of the influencing parameters on single-band CARS microscopy, the optimal parameters are summarized in table 3.1.

Parameter	Value
Wavelength range pump and Stokes	800 – 1400 nm*
Raman shift range	0 – 3500 cm^{-1}
Pulse duration (for 1 cm^{-1} resolution)	15
f_{rep} for video rate acquisition / 1 μ s pixel dwell time	8 MHz/1 MHz
Peak power at the sample	\sim 300 W**
Average power at the sample	\sim 30 mW**
Minimal output power	$>$ 100 mW per beam

Table 3.1: The Optimal parameter set for single band CARS microscopy. * Even though a 1400 nm excitation still allows for submicron spatial resolution utilizing high NA-objectives, there is, to the best of our knowledge, currently in this wavelength range no apochromatically corrected microscope objective available which covers the pump and the required Stokes radiation. ** Since the CARS signal depends on the peak intensity rather than on the peak power, this value is strongly affected by the NA of the microscope objective. The values stated are valid for high NA-objectives [16].

The repetition rate for video rate acquisition was chosen to be 8 MHz in order to support the acquisition of frames with a resolution of 500x500 px with at a rate of 24 frames per second.

Additionally, the intensity ratio of the CARS pump to the Stokes radiation should be 2 : 1 to generate the maximum signal strength [?].

3.3 Stimulated Raman Scattering Imaging

As it has been mentioned in chapter 2.2.3, SRS imaging has a much higher demand on the laser stability than CARS. Before the optimal values for SRS microscopy are presented the different origins of noise in a SRS experiment have to be identified.

Stimulated Raman scattering introduces extreme prerequisites on the laser. As it was discussed in chapter 2.2.3, the SRS signal is buried deep within the pump or the Stokes signal. By employing a lock-in detector, the signal at the modulation frequency can be separated. However, both the photo detector and the laser introduce noise, which becomes a background signal at the modulation frequency. This, depending on the detection speed, can be easily as strong as the SRS signal. Figure 3.5 depicts a scheme of a SRS experiment with the parameters that influence the final signal to noise ratio the most.



Figure 3.5: SRS principle and most influencing parameters on the signal voltage and background noise

The signal voltage from a lock-in detector in a SRS experiment is [25]:

$$V_{SRS} = \frac{1}{2} b_{SRS} \text{Im}(\chi^{(3)}) \frac{P_P P_S \tau_{SRS}}{A f_{rep} \tau_P \tau_s} G q s R_l, \quad (3.5)$$

with

$$b_{SRS} \approx \frac{2.8 \times 10^4 z}{n_p n_s \lambda_p}.$$

In b_{SRS} n_i is the refractive index at the signal and pump wavelengths λ and z is the Rayleigh length of the focused beam. In the general equation $\chi^{(3)}$ is the third order nonlinear susceptibility, which is dependent on the molecular resonance and the molecular density. P is the peak power, τ the pulse duration, A is the focus area of the focal spot, f_{rep} is the modulation frequency (we assume a duty cycle of 50%, which leads to the $1/2$ in the equation), G represents the photo diode response multiplied by the lock-in gain, s is the signal collection rate (the portion of the signal, which is collected by the photo diode) and R_l is the load resistance. The q -factor describes the spectral and temporal overlap of the pump and Stokes pulses [25]. The signal voltage is superimposed by noise originating from three different sources: The noise of the laser source, the shot noise and the Johnson noise of the detector. The noise of the laser at the modulation frequency creates a

3. Optimal Parameter Set of Laser Sources for Three-Photon Excited Fluorescence Imaging and Coherent Raman Scattering

background signal:

$$V_{LN} = G_{Lock-In} \sqrt{\frac{10^{\sigma_{RIN}/10}}{2\Delta t}} P_p G_{PD} q s R_l, \quad (3.6)$$

where σ_{RIN} is the relative intensity noise of the non modulated beam at the modulation frequency and Δt is the averaging time. In essence, this is the noise of the non modulated laser beam at the modulation frequency after the detection and amplification in the Lock-In over the load resistance R_l . The Johnson noise is white noise caused by the photo detector being at a temperature T:

$$V_J = G_{Lock-In} \sqrt{\frac{2k_B T R_l}{\Delta t}}. \quad (3.7)$$

Finally, the quantum nature of photons creates a lower boundary on the noise that a optical signal can have. The so-called shot noise is caused as only a finite number of photons can be detected. As the fluctuation of the detected power changes by at least the amount of energy a single photon is carrying, the shot noise depends on the average power of the detected signal.

$$V_{shot} = G_{Lock-In} \sqrt{\frac{e P_p G_{PD} q s}{\Delta t}} R_l, \quad (3.8)$$

For an exemplary SRS experiment the following parameters are assumed: $R_l = 50\Omega$, $s = 1$, $q = 1$, $\tau_{SRS} = \tau_P = \tau_s = 15ps$, $G = G_{Lock-In} G_{PD} = 50$, $P_P = P_S = 15mW$, $A = 0.09\mu m^2$, $n_p = n_s = 1.3$, $\frac{z}{\lambda_p} = 1$. For a strong resonance, $|Im(\chi^{(3)})| \approx 10^{-21} m^2/V^2$, the voltage of the generated SRS signal will be $V_{SRS} \approx 345mV$. For a typical relative intensity noise of a OPO of $-150dBc/Hz$ at the modulation frequency, the overall noise of the measurement is then [25]: $V_{noise,SRS} = \sqrt{V_{LN}^2 + V_J^2 + V_{shot}^2} = \sqrt{(7.7 \times 10^{-7})^2 + (0.6 \times 10^{-7})^2 + (4.0 \times 10^{-7})^2} = \frac{8.7 \times 10^{-7}}{\sqrt{\Delta t}}$. The signal-to-noise ratio is then $SNR_{SRS} = V_{SRS}/V_{noise,SRS} \approx 4 \times 10^5 \sqrt{\Delta t}$. In order to achieve a high SNR of 100, the integration time Δt needs to be about $0.06\mu s$. Therefore the pixel acquisition rate is limited to $\approx 16Mpx/s$. This value is high enough to reach video rate pixel acquisition frequencies. The maximum pixel acquisition rate with respect to the RIN at the modulation frequency is depicted in figure 3.6.

3. Optimal Parameter Set of Laser Sources for Three-Photon Excited Fluorescence Imaging and Coherent Raman Scattering

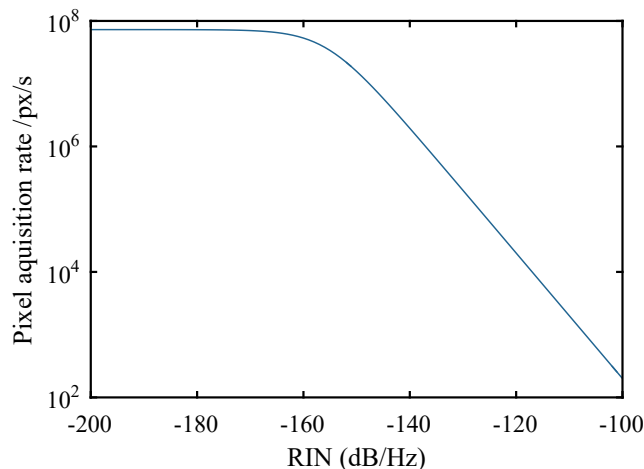


Figure 3.6: Pixel acquisition rate with respect to the RIN at the modulation frequency

The sharp decline in scanning speed for the RIN demonstrates the importance of the laser noise in a SRS measurement.

To reach higher rates, either part of the SNR needs to be sacrificed, or a higher RIN of the non modulated beam at the modulation frequency has to be achieved. In practice, s and q are not going to be unity, which will increase the background noise level caused by Johnson noise and shot-noise. Also, if the Raman resonance is weaker, V_{SRS} is going to decrease linearly. In this case higher integration times are needed. In any case, the SRS laser needs a RIN level better than -150 dBc/Hz in order to achieve fast imaging speeds. Table 3.2 summarizes the optimal parameters for SRS imaging.

Parameter	Value
Wavelength range pump and Stokes	800 – 1400 nm*
Raman shift range	0 – 3500 cm^{-1}
Pulse duration (1 cm^{-1} resolution)	15
f_{rep} for video rate acquisition / $1 \mu\text{s}$ pixel dwell time	8 to 20 MHz
Peak power at the sample	$\sim 300 \text{ W}^{**}$
Average power at the sample	$\sim 30 \text{ mW}^{**}$
Minimal output power	$> 100 \text{ mW}$ per beam
RIN at modulation frequency	$< -150 \text{ dBc}$

Table 3.2: The optimal parameter set for single band SRS.

3.4 Three-Photon Excited Fluorescence Imaging

Three-photon excited fluorescence is not chemically specific since it relies on fluorescence markers or auto-fluorescence. Therefore, the bandwidth of the pump photons is not a limiting factor and can be as broad as the transparency region described in subsection 3.1.1. The main limitation regarding the wavelength becomes the spectral position of the third harmonic signal which excites the fluorophor. If its wavelength is too short, absorption and scattering will weaken the signal severely. Thus, 3PEF excitation wavelengths in the range of 1300 and 1700 *nm* have been used to scan deeply into biological tissue [6, 26].

It has been established in subsection 3.1.3 that the order of non-linearity in the damage equation is > 2 for a few hundred of femtoseconds of pump pulse durations. There are no studies on the degree of non-linearity for pulse durations for only tens of femtoseconds. If the trend continues, one could expect a non-linearity of up to $n = 3$ which would make the choice of the repetition rate ambiguous. Xu et. al. proposes the use of low repetition rates for 3PEF in order to reach high peak powers at low average powers [27]. The optimal parameters for 3PEF are summarized in figure 3.3.

Parameter	Value
Wavelength range pump and Stokes	1300 or 1700 <i>nm</i>
Pulse duration	< 1 <i>ps</i>
Repetition rate	1 <i>MHz</i>
Peak power at the sample	~ 100 <i>kW</i>
Average power at the sample	~ 10 <i>mW</i>
Minimal output power	> 100 <i>mW</i> per beam

Table 3.3: The Optimal parameter set for single band SRS.

So far, the optimum parameters for MPI and CRS imaging have been established. The following chapter will supply the basic knowledge about optical fibers and fiber lasers to be able to understand the fiber laser concept that has been developed in this work in order to produce these laser parameters form a compact fiber laser source.

4 Fundamentals of Optical Fibers

In this chapter, the key elements of the physical background of optical fibers are covered in order to understand the behavior and design aspects of the laser concept that will be presented in chapter 5.

4.1 Optical Fibers and Photonic Crystal Structures

An optical fiber is a waveguide capable of transporting light [28,29]. To understand the guiding properties of so-called single-mode fibers it is necessary to solve the Maxwell equations with the boundary conditions appropriate for a fiber structure.

From the Maxwell equations it is possible to derive the basic wave equation describing the propagation of electromagnetic waves [30]:

$$\nabla \times \nabla \times \mathbf{E} = -\frac{1}{c^2} \frac{\partial^2 \mathbf{E}}{\partial t^2} - \mu_0 \frac{\partial^2 \mathbf{P}}{\partial t^2}, \quad (4.1)$$

where \mathbf{E} is the electrical field vector, \mathbf{P} the induced polarization of the material, μ_0 the vacuum permeability and c the speed of light in vacuum. To simplify the equation, the following assumption will be made: the polarization depends exclusively on the local \mathbf{E} field in the medium. Additionally, the non-linear part of the polarization vector is relatively small compared to its linear part, the losses in the fiber are small and the host material is isotropic. With these assumptions, it is possible to derive [30]:

$$\nabla^2 \tilde{\mathbf{E}} + n^2(\omega) \frac{\omega^2}{c^2} \tilde{\mathbf{E}} = 0, \quad (4.2)$$

where ω is the radial frequency of the carrier wave and n is the refractive index of the medium the wave is traveling through. In this work, short laser pulses within fibers are described, therefore, the optical wave will be described by the carrier wave and its envelope. If the relative rate of change of the pulse envelope ($\tilde{A}(z, \omega - \omega_0)$) is much smaller than the carrier oscillations ($\exp(-i\omega_0 t)$), the terms can be separated [31]. The radial field distribution within the fiber can then be

4. Fundamentals of Optical Fibers

solved by choosing the ansatz [30]:

$$\tilde{\mathbf{E}}(\mathbf{r}, \omega - \omega_0) = \mathbf{e}_P \cdot F(x, y) \cdot \tilde{A}(z, \omega - \omega_0) \cdot \exp[-i(\omega_0 t - \beta z)]. \quad (4.3)$$

with the Fourier transformation relation $\tilde{\mathbf{E}}(\mathbf{r}, \omega) = \frac{1}{\sqrt{2\pi}} \int_{-\infty}^{\infty} \mathbf{E}(\mathbf{r}, t) \exp(i\omega t) dt$.

The resulting solutions of the possible modes are distinguished by their propagation parameter β_{nm} and their transverse field distribution function $F_{nm}(x, y)$ [30].

$$\left(\frac{\partial^2}{\partial x^2} + \frac{\partial^2}{\partial y^2} \right) F + \epsilon(\omega) \frac{\omega^2}{c^2} F = \beta_{nm}^2 \cdot F \quad (4.4)$$

$$2i\beta_0 \frac{\partial}{\partial z} \tilde{A} + \left(\epsilon(\omega) \frac{\omega^2}{c^2} - \beta_{nm}^2 \right) \tilde{A} = 0 \quad (4.5)$$

These discrete solutions $F(x, y)$, which describe the propagation of light inside an optical fiber are called the Helmholtz equations. The meaning of the propagation constant β will be discussed in detail in the following section 4.2.

One of the most simple and at the same time most common optical fiber structures can be seen in fig. 4.1: the so-called step-index fiber, where the core index n_1 is higher than the cladding index n_2 . The index difference is set by doping the glasses. Depending on this difference $\Delta n = n_1 - n_2$, the core radius a and the mean wavelength λ of the light, a certain set of guided modes is supported by the core of the fiber satisfying equations 4.4 and 4.5. Usually, fused silica is the material of choice for guiding light in the visible and near-infrared spectral regions, due to the extremely low propagation losses in high quality silica glasses.

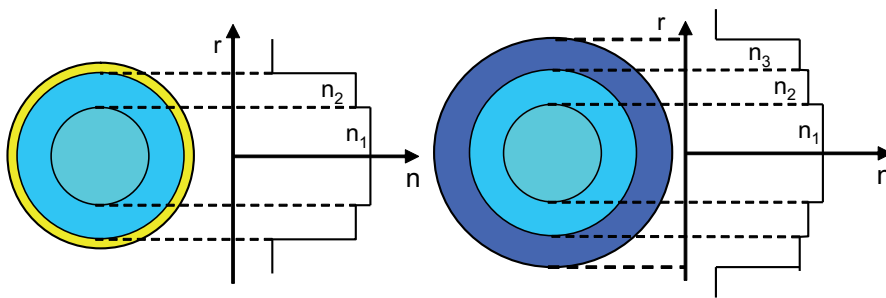


Figure 4.1: Step-index fibers with one and two claddings.

If only the lowest order, Gaussian-like mode profile shall be supported by the optical fiber, the index step Δn has to be small enough to exclude any higher order modes. In particular, to ensure this single-mode guidance, the fiber has to fulfill $V < V_C \approx 2.405$ with [30]:

$$V = \frac{2\pi}{\lambda} a \sqrt{n_1^2 - n_2^2}. \quad (4.6)$$

Due to the wavelength dependence of this condition, step-index single-mode fibers, as the one depicted in 4.1, will become multi-mode below a certain cut-off wavelength. Therefore, in order to ensure single-mode guidance in a broader spectral range a different kind of fiber design is necessary.

In 1996 a new kind of fiber was proposed and fabricated: the so-called photonic crystal fiber [32]. This fiber consists of a solid core and a periodic arrangement of holes which form the cladding. The structural parameters of the core and cladding design, namely the hole size, hole spacing and hole pattern, influence the waveguide properties greatly (see fig.4.2). One example of this is the so-called endlessly single mode fiber [33]. In this type of fiber the structural parameters can be chosen so that the single-mode guidance is maintained over the whole transparency window of fused silica and is only limited by bending losses at very short wavelengths.

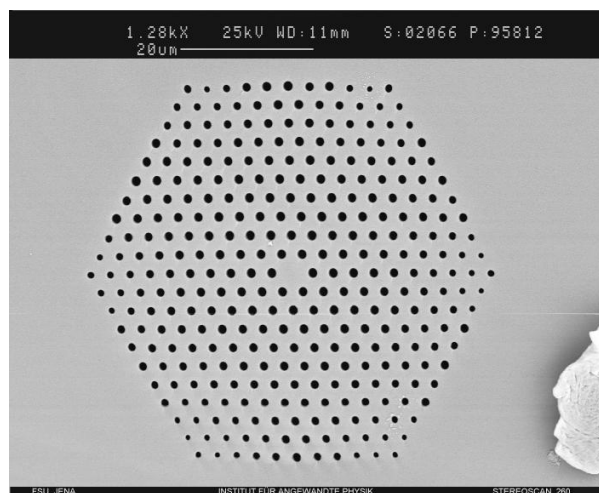


Figure 4.2: Structure of a photonic crystal fiber.

Over the years many different structures have followed enabling new paths in photonics research. One key design aspect is the manipulation of the dispersion properties of such fibers which will be introduced next.

4.2 Waveguide Dispersion

The chromatic dispersion reflects the fact that every wavelength may travel through an optical medium with a slightly different velocity ($n = n(\lambda)$). The refractive index $n(\lambda) = c/v(\lambda)$ is the ratio of the velocity of light in vacuum c compared to the

velocity of light traveling in the optical medium $v(\lambda)$ at a particular wavelength λ . This chromatic dispersion relation is different for every material and will be called material dispersion. If light is now confined in a waveguide and propagates in a certain mode, the dispersion relation is altered by the waveguide. This new dispersion term is called waveguide dispersion and it can be treated separately from the material dispersion.

The material dispersion is usually described by the Sellmeier equation, which gives insight into the origin of chromatic dispersion itself: The Kramer-Kronig's relation states that absorption causes dispersion, and since light suffers absorption of different strengths in the ultra-violet and the infrared spectral regions, chromatic dispersion is present in-between these spectral regions.

The general Sellmeier equation can be written as [30]:

$$n^2(\omega) = 1 + \sum_{j=1}^m \frac{B_j \omega_j^2}{\omega_j^2 - \omega^2}, \quad (4.7)$$

with $\omega = 2\pi c/\lambda$ being the angular frequency of the light. B_j corresponds to the strength of the absorption line and ω_j to the spectral position of the absorption; contributing to material dispersion.

The origin of waveguide dispersion is fundamentally different. To explain it, only the fundamental mode will be considered. From the Helmholtz equations 4.4 and 4.5 we know that most of the electrical field is confined in the core, but there is also some energy traveling through the cladding, called the evanescent field (which is an exponentially decaying field required to fulfill the boundary condition between the core and the cladding). The mode, therefore, experiences not only the refractive index of the core but also that from the cladding. The resulting overall refractive index is called the effective index n_{eff} . On top of that, the shape of the electrical field is slightly different for each wavelength, with longer wavelengths penetrating, in general, the cladding material more deeply, meaning their evanescent field reaches deeper into the cladding structure. Consequently, usually the relative overlap with the cladding increases with wavelength causing a change in the overall dispersion of the waveguide compared to its material dispersion. To describe the waveguide dispersion, the propagation of the electrical field of a lightwave traveling in the z direction is considered: $E = E_0 \cdot e^{i(k \cdot z - \omega \cdot t)}$ where the wave-number $k(\omega)$ is:

$$k(\omega) = n_{eff}(\omega) \frac{\omega}{c} \quad (4.8)$$

The dispersion relation of the wave-number can be approximated with a Taylor

4. Fundamentals of Optical Fibers

expansion centered around ω_0 by [30]:

$$k(\omega) = n_{eff}(\omega) \frac{\omega}{c} = \beta_0 + \beta_1 (\omega - \omega_0) + \frac{1}{2} \beta_2 (\omega - \omega_0)^2 + \dots, \quad (4.9)$$

with $\beta_j = \frac{\partial^j k(\omega)}{\partial \omega^j} |_{\omega=\omega_0}$.

These β_j are called the dispersion constants and reflect certain aspects of the traveling wave packet through an optical medium. $\beta_0 = n_{eff}(\omega_0) \frac{\omega_0}{c} = \frac{\omega_0}{v_P}$ describes the phase velocity v_P of the wave or, in other words, this is the velocity with which the carrier wave of a wave package is traveling. It is known from Fourier theory that waves which have a finite duration consist of many frequencies. This means that a wave package or a laser pulse can have a different velocity than its carrier wave, this is the so-called group-velocity. The relation between the phase and group velocity of a wave package is defined by [34]:

$$v_g \equiv \frac{\partial \omega}{\partial k} = v_p - \lambda \frac{\partial v_p}{\partial \lambda} \quad (4.10)$$

From this equation, the relation of β_1 to the group velocity can be derived:

$$\beta_1 = \frac{1}{v_g} = \frac{1}{c} \left(n_{eff} + \omega \frac{dn}{d\omega} \right). \quad (4.11)$$

As stated earlier, a light pulse has a limited spectral bandwidth as the velocity of each of the spectral components of the pulse is, in general, different. Therefore, the pulse is going to disperse, i.e. become longer, while propagating through a medium. The magnitude of this dispersion is described by β_2 :

$$\beta_2 = \frac{\partial}{\partial \omega} \left(\frac{1}{v_g} \right) = \frac{\partial \beta_1}{\partial \omega} = \frac{1}{c} \left(2 \frac{dn_{eff}}{d\omega} + \omega \frac{d^2 n_{eff}}{d\omega^2} \right), \quad (4.12)$$

This phenomenon is called group velocity dispersion (GVD) and it is often written as:

$$D = -\frac{2\pi c}{\lambda^2} \beta_2, \quad [D] = \frac{\text{ps}}{\text{nm} \cdot \text{km}} \quad (4.13)$$

stating how much longer a transform limited pulse with a certain spectral bandwidth has become after propagating a certain distance through a medium. If $D < 0$ the dispersion is defined to be anomalous and if $D > 0$ it is normal.

The next order of the dispersion terms is the third order dispersion:

$$TOD = \beta_3 = \frac{\partial \beta_2}{\partial \omega} |_{\omega=\omega_0} = \frac{1}{c} \left(3 \frac{d^2 n_{eff}}{d\omega^2} + \omega \frac{d^3 n_{eff}}{d\omega^3} \right). \quad (4.14)$$

which defines the change of the group velocity dispersion with the angular frequency. The manipulation of the dispersion e.g. in a photonic crystal fiber is of central importance and will be considered in chapter 5 [35].

4.3 Non-Linear Effects for Frequency Conversion in Optical Fibers

One of the most intriguing phenomena in waveguides is the onset of non-linear effects at relatively low peak powers. Usually their impact on the pulse is considered to be detrimental, but if light confined as a fundamental mode in a fiber experiences these effects in a predictable manner, they can also be understood as a toolbox for changing the pulse parameters to one's needs. As it was introduced in chapter 3, CRS imaging needs two spectrally separated pulses with a well-defined photon energy difference. Therefore, different fiber-based frequency conversion techniques will be explored here.

Each of the conversion techniques has its own advantages with respect to the application and the required pulse parameters. At first, self-phase modulation will be introduced, which is one of the most basic effects. Afterwards, Raman scattering in fused silica fibers will be covered and used as the basis to understand self-soliton frequency shift (SSFS). The next subsection presents super-continuum (SC) generation, which works for a high range of input pulse parameters. However, as the energy is almost evenly spread across a very broad spectral range, the spectral power density becomes quite low. Since both SSFS and SC generation suffer from broad spectral bandwidths, a technique called spectral self-compression may be employed. Finally, four-wave mixing in endlessly single mode fibers will be introduced and discussed. It offers the unique ability to convert light directly to new frequencies within a narrow spectral band. The pulses are easily generated with picosecond pump pulse durations, being optimal for CRS imaging.

4.3.1 Self-Phase Modulation

The most basic non-linear effect is the change of the temporal phase of a pulse due to the intensity-dependent refractive index change of a fiber. This effect is called self-phase modulation (SPM). If the intensity of the pulse is high enough to force the polarization vector of the medium to react in a non-linear fashion, the non-linear coefficient n_2 has to be taken into account. The nonlinear change of the refractive index is then given by [30]:

$$\Delta n = n_2 |E|^2(t). \quad (4.15)$$

and it is dependent on the absolute value of the amplitude of the electrical field E of the laser pulse. In the frame of this work this response will be considered to be instantaneous. Thus, the maximum change of the temporal phase after propagating a distance L through a fiber is:

$$\Delta\phi(0) = B = \int_0^L \frac{\omega_0}{c} \Delta n(0) dz = \frac{\omega_0}{c} L n_2 E^2(0) = \gamma P L, \quad (4.16)$$

where P is the peak power of the laser pulse and $\gamma = \frac{4n_2\omega_0}{\pi c} d_{eff}^2$, with d_{eff} being the effective mode-field diameter of the fiber. The value obtained in equation 4.16 is also called the B-Integral. Due to the rapid phase change occurring across the pulse (due to its temporal changing intensity), new frequency components are generated. Thus, the resulting bandwidth of a formerly transform-limited pulse after propagating a distance L in the medium is:

$$\Delta\omega(t) = \omega(t) - \omega_0 = -\frac{\partial}{\partial t} \left[\frac{\omega_0}{c} L \cdot n_2 E^2(t) \right]. \quad (4.17)$$

For a Gaussian-shaped pulse ($E(t) = E_0 \exp\left[-\frac{(t-t_0)^2}{\tau^2}\right]$), the pulse is broadened to [36]:

$$|\Delta\omega_{\max}| = \Delta\phi_{\max} \frac{2}{\tau} e^{-0,5} = \Delta\phi_{\max} \frac{1,21}{\tau}. \quad (4.18)$$

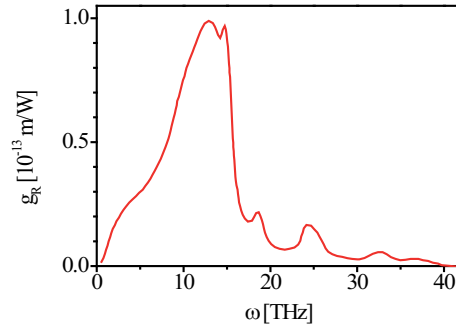
A measure of the strength of this effect is the nonlinear length [30]:

$$L_{NL} = \frac{1}{\gamma P_0} \quad (4.19)$$

. It determines the length of a certain fiber after which the pulse peak accumulated a phase of $B = 1$.

4.3.2 Raman Scattering

Raman scattering is the inelastic scattering of photons in a medium due to molecular vibrations. As the photons are scattered by molecules or the atom lattice of a solid, part of their energy is absorbed exciting molecular vibrations called phonons. This way, the scattered light is red shifted. Figure 4.3 depicts the Raman gain in fused silica with its peak at $13 THz$.


 Figure 4.3: Raman gain g_R . [37]

4.3.3 Soliton-Self Frequency Shift

The soliton self-frequency shift (SSFS) is a non-linear frequency conversion technique relying on the combination of dispersion, self-phase modulation and Raman scattering [30]. The idea is that an ultra-short pulse experiencing SPM is spectrally broadened. At the same time, if the pulse experiences anomalous dispersion, the pulse is constantly compressed towards its transform-limited pulse duration. The resulting pulses is called soliton since it is a stationary solution in a waveguide, which after its generation, is unchanged as it propagates in its host fiber. To generate a soliton of the order N , the dispersion length $L_D = \frac{T_0^2}{|\beta_2|}$ has to fulfill the following condition [30]:

$$N^2 = \frac{L_D}{L_{NL}} = \frac{T_0^2 \gamma P_0}{|\beta_2|}, \quad (4.20)$$

with a soliton pulse duration T_0 . The dispersion length can be seen as an analogy to the Rayleigh length. It causes an initially unchirped pulse of the duration T_0 to increase its duration to a factor of $\sqrt{2}$ [38]. The peak power of the soliton is related to its temporal duration and the group velocity dispersion of the fiber by:

$$P_0 = \frac{|\beta_2|}{\gamma T_0^2}. \quad (4.21)$$

To explain the basic shape of a soliton, the non-linear propagation of light in a fiber needs to be described. The basic propagation equation (eq.4.1) is rewritten and simplified by assuming a slowly-varying pulse envelope with respect to the oscillations of the carrier wave ($|\frac{\partial^2 A}{\partial z^2}| \ll |k \frac{\partial A}{\partial z}|$). The resulting equation considers

SPM and dispersion up to the second order [30]:

$$i\frac{\partial A}{\partial z} = \frac{\beta_2}{2}\frac{\partial^2 A}{\partial T^2} - \gamma N^2|A|^2A, \quad (4.22)$$

This equation is commonly called the non-linear Schrödinger equation (NLS). For the fundamental solution ($N = 1$), eq. 4.22 can be solved giving the temporal profile:

$$A(z, T) = \sqrt{P_0} \cdot \operatorname{sech}\left(\frac{T}{T_0}\right) \cdot \exp\left(\frac{iz}{2L_D}\right) \quad (4.23)$$

It can be seen that the temporal intensity profile of a soliton follows a sech^2 -function. Higher order solitons change their temporal and spectral shape periodically over a length related to the dispersion length $z_0 = \frac{\pi}{2}L_D$. After this cycle, the process starts over again. In real fibers, higher order solitons decay into several fundamental solitons by soliton fission, which happens after the so-called characteristic fission length [30]:

$$z_{\text{fiss}} = \frac{L_D}{N} = \frac{T_0}{\sqrt{|\beta_2| \cdot P_0 \cdot \gamma}}. \quad (4.24)$$

Therefore, for frequency conversion in optical fibers it is only practical to excite fundamental solitons. Therefore, the potential peak power of a frequency shifted soliton is ultimately defined by the conversion fiber. This simplified description has to be expanded by Raman scattering in order to explain the self-frequency shifting properties of solitons in real fibers.

Up to this point we have established the formation of fundamental solitons where the temporal soliton duration is determined by the dispersion properties of the fiber, the fiber material and its peak power. In typical highly-nonlinear single-mode PCFs, fundamental solitons have a pulse duration shorter than 100 fs. Consequently, their spectral bandwidth spans over tens of nanometers. Thus, the red part of their spectrum overlaps with the Raman gain in fused silica (fig. 4.3). In this context a spectrally broad soliton can simultaneously act as both the pump and the seed signal for the Raman scattering process. This phenomenon is also called intra-pulse stimulated Raman scattering and ultimately leads to a red-shifting of the soliton spectrum propagating along the fiber.

Equation 4.21, suggests that by decreasing the pulse duration of the soliton, its energy could be enhanced significantly. This is true to a point where the bandwidth of the soliton reaches a value at which the dispersion of the fiber is strongly influenced by the third order dispersion of the fiber. On the other end

of the energy scale, narrowband solitons in the picosecond time regime are also possible but lack the spectral bandwidth to enable intra-pulse stimulated Raman scattering and the self-frequency shifting of solitons.

Scaling the peak power of solitons in fused silica fibers, consequently, involves the scaling of the diameter of the mode [39, 40]. In order to achieve high conversion efficiencies of the pump pulse to the Raman shifted soliton, the pump field temporal shape should be as similar as possible to the final soliton shape, which demands sophisticated ultra-short pump sources [41].

4.3.4 Four-Wave Mixing

Four-wave mixing (FWM) is a nonlinear elastic interaction between four waves. If the pump photons have the same frequency, the process is called degenerate FWM. It is a $\chi^{(3)}$ process, which is the lowest order non-linearity occurring in isotropic media such as fused silica. In order for FWM to be efficient, energy and momentum conservation have to be fulfilled [30].

Energy conservation:

$$2\omega_{pump} = \omega_{signal} + \omega_{idler}, \quad (4.25)$$

Momentum conservation:

$$2\beta_{pump} = \beta_{signal} + \beta_{idler} + 2\gamma P_{pump}, \quad (4.26)$$

where γ is the nonlinear parameter (see 4.16) and P_{Pump} is the pump peak power. The momentum conservation can be expressed in a scalar equation because the waves propagate in only one direction in the fiber.

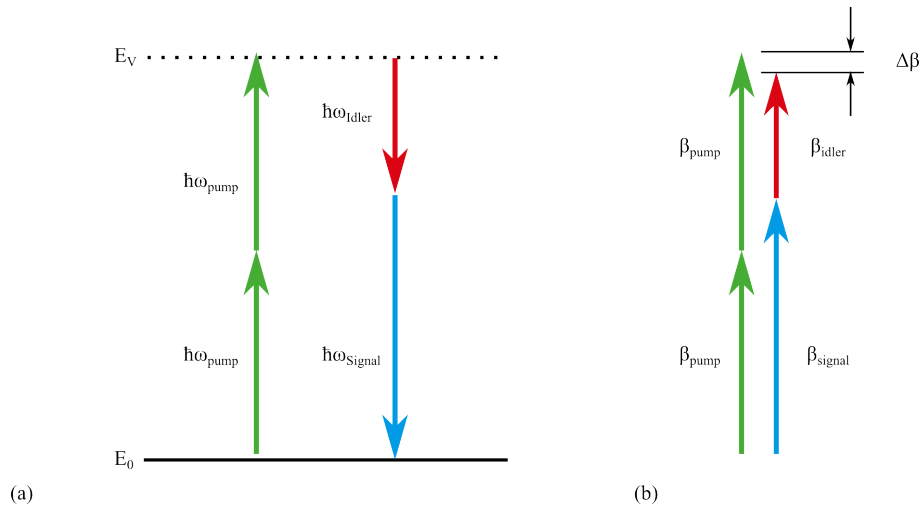


Abbildung 4.4: Phase-matching condition: (a) energy and (b) momentum conservation without the peak-power-dependent term.

Figure 4.4(a) schematically illustrates the energy conservation condition. Hereby, two pump photons are converted into a signal and an idler photon. E_V is introduced as a virtual state which acts as an excited state without lifetime. Figure 4.4(b) on the other hand, shows the scalar momentum conservation within the fiber with a small phase mismatch [30]: $\Delta\beta = \beta_{signal} + \beta_{idler} - 2\beta_{pump} + 2\gamma P_{pump} = \Delta\beta_0 + 2\gamma P_{pump}$.

Figure 4.7 depicts the phase-matching condition for different peak powers in an endlessly single mode fiber. For the extreme case of a vanishing peak power, the phase-matched wavelengths for the signal and idler meet at the zero dispersion wavelength (ZDW) of the conversion fiber. At this point four-wave mixing degenerates into SPM. On the normal dispersion side the signal and idler wavelengths allow for a wide spectral conversion range depending on the exact pump wavelength. When the peak power increases, the phase-matched signal and idler wavelengths shift apart. This also allows for conversion in the anomalous side of the dispersion, albeit over a much smaller spectral ranges. Traditionally, this conversion branch is called modulation instabilities and is regarded to be a limiting factor for narrowly spaced multiplexed fiber communications [42].

The four-wave mixing process itself is described by a set of coupled nonlinear Schrödinger equations. These equations describe the energy flow between the pump, signal and idler fields. This set of equations can be solved numerically [43]. If the pump suffers only a small relative perturbation during the conversion process, it is possible to derive an approximate analytical solution for the gain of the FWM conversion process. Thus, for the unsaturated single-pass amplification, the gain for the signal in a fiber with length L can be written in the form [30]:

$$G = 1 + \left(\frac{\gamma P_{pump}}{g} \right)^2 \sinh^2 (gL), \quad (4.27)$$

where $g = \sqrt{(\gamma P_{pump})^2 - (\Delta\beta/2)^2}$ is the parametric gain coefficient. The maximum parametric gain is obtained when there is perfect phase-matching ($\Delta\beta = 0$). In this case the FWM gain is

$$G = 1 + \sinh^2 (\gamma P_{pump} L) = 1 + \sinh^2 (B), \quad (4.28)$$

which has a spectral bandwidth that is dependent on the pump peak power P_{pump} . We define the bandwidth of the FWM gain to be the width where g drops to 0 due to the phase-mismatch $\Delta\beta$. The bandwidth is then:

$$BW_{FWM} = 2\Delta\beta_0 = 4\gamma P_{pump}. \quad (4.29)$$

The maximum small-signal gain is in the center of the gain bandwidth:

$$\Delta\beta_0 = -2\gamma P_{pump}. \quad (4.30)$$

It has already been established that the phase-matching condition has to be fulfilled in order to allow the FWM process to work. However, yet another condition has to be fulfilled to allow for efficient conversion. This condition is the overlap of the involved modes in the fiber. Depending on the spectral separation between the converted radiation and the pump light, the modal field diameters can vary strongly depending on the fiber design. For a standard step-index single-mode fiber with a cut-off wavelength of 800 nm, the mode-field diameter of the fundamental mode varies from 3.5 μm at 500 nm to 11 μm at 1500 nm [44]. In this case the mode-field area overlap integral becomes small for a large spectral separation between the pump light and the frequency converted signal, which results in a decrease of the conversion efficiency [45]. Consequently, the parametric gain factor has to be modified to include the effective mode-overlap:

$$G = 1 + \sinh^2 (\gamma P_{pump} L f_{ijkl}), \quad (4.31)$$

which includes the overlap integral between the four fiber modes involved in the FWM process:

$$f_{ijkl} = \frac{\langle F_i^* F_j^* F_k F_l \rangle}{[\langle |F_i|^2 \rangle \langle |F_j|^2 \rangle \langle |F_k|^2 \rangle \langle |F_l|^2 \rangle]^{1/2}}, \quad (4.32)$$

4. Fundamentals of Optical Fibers

where the angle brackets denote the integration over the transverse coordinated x and y [30]. Hence, to obtain an efficient frequency conversion over a broad spectral range, it is necessary to use a single mode fiber, in which the mode field diameter is nearly constant over a very large spectral bandwidths. As introduced in section 4.2, ESM fibers have this property ¹. In order to check this, the evolution of the mode field diameter with the wavelength was simulated in a single-clad PCF structure with a one-hole-missing design. The pitch of the fiber Λ (i.e. the hole to hole distance) structure was chosen to fulfill $d/\Lambda = 0.5$. d is the hole diameter and Λ is the hole-to-hole distance (see figure 4.5 (a)). Λ was now varied from 2 to 5 μm in steps of 0.25 μm and depicted in figure 4.5 (b).

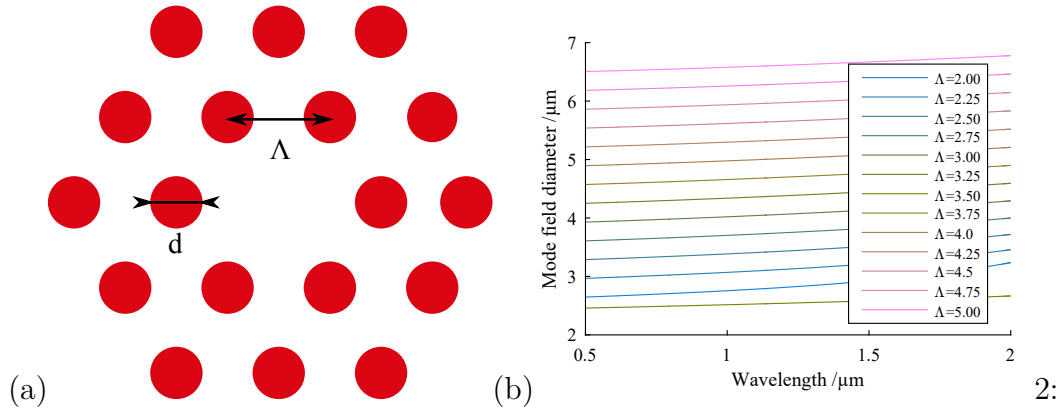


Abbildung 4.5: (a) ESM structure. (b) Effective mode-field diameter of different ESM structures versus wavelength with Λ varied from 2 to 5 μm (blue to pink).

It can be seen that the mode-field diameter changes very little with wavelength in comparison to a step-index fiber. Thus, light conversion via four-wave mixing is not limited by the mode-field overlap in the conversion fibers.

By altering the structural parameters of the ESM fiber in the same way as before, the effective refractive index n_{eff} can be influenced (see sec. 4.2). The resulting n_{eff} has been plotted in figure 4.6 (a), where the black line represents the pure material dispersion of fused silica. Again, the influence of the waveguide is more pronounced at smaller core dimensions and longer wavelengths, which has been already discussed in section 4.2. The resulting second-order dispersion of the different fiber structures has been plotted in 4.6 (b). The so-called zero-dispersion

¹Strictly speaking, ESM fibers are defined for $d/\lambda < 0.42$ [46, 47]. At this value the effective V parameter $V_{eff} < V_C$ in accordance with the definition for a single mode fiber. In practice even higher values for d/λ result in are effectively endlessly single-mode behavior as the cut-off wavelength for the lowest higher-order mode is extremely short in comparison to the wavelengths at which the fiber will be used. Additionally, as the propagation constants are substantially different from the one of the fundamental mode, mode coupling caused by microbendings and other perturbation are very weak. [48]

4. Fundamentals of Optical Fibers

wavelength (ZDW), at which the dispersion switches between normal and anomalous is shifted in the fiber towards shorter wavelengths and away from the ZDW of fused silica (4.6 (b)). For the smallest core dimensions a second ZDW emerges at longer wavelengths. For even smaller core dimensions, the two ZDWs would shift further into the blue and slide closer together. Finally, if additionally d/Λ is below 0.4, the fiber dispersion does not cross the zero dispersion line, which makes it a so-called all-normal dispersion fiber [49].

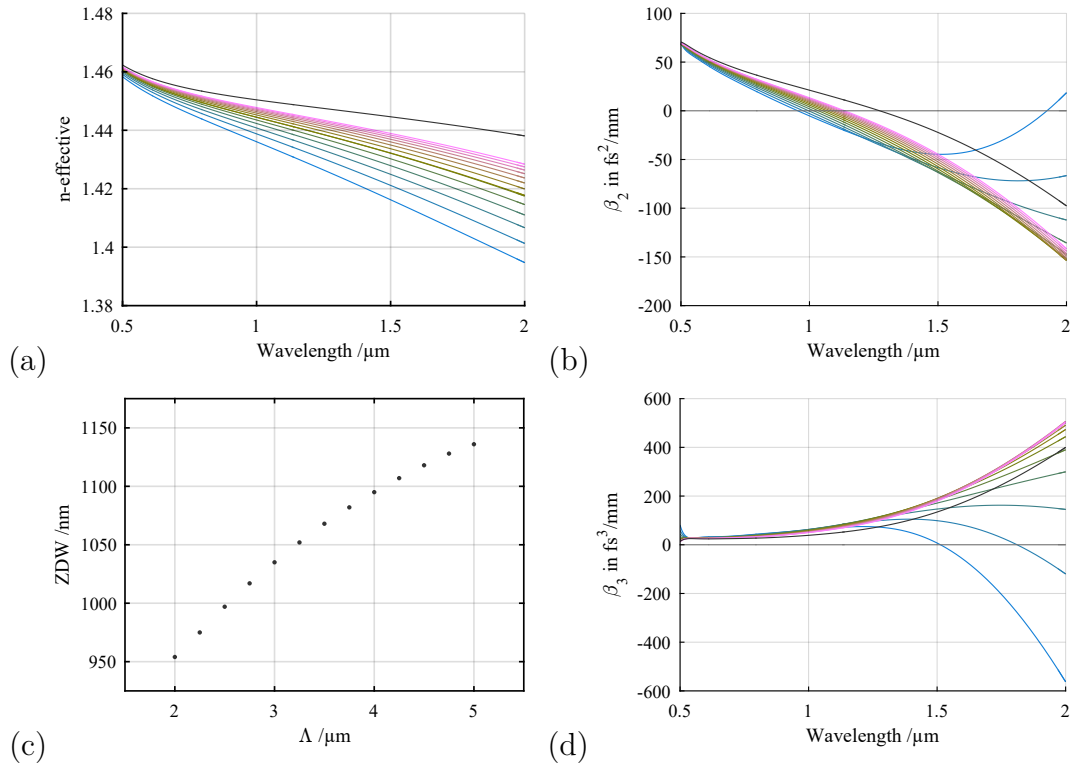


Abbildung 4.6: Effective refractive index n_{eff} for ESM structures versus wavelength with Λ varied from 2 to 5 μm (blue to pink) with constant $d/\Lambda = 0.5$. Also shown are (b) the resulting β_2 values, the (c) zero-dispersion wavelengths and (d) β_3 values. The black curves represent the material dispersion of fused silica.

The FWM phase-matching diagrams were calculated for the regarded fibers and plotted in figure 4.7 (a). It shows the phase-matched signal and idler wavelengths depending on the pump wavelength. At these wavelengths, the gain for the signal and idler has a local maximum. In this work, the spectral feature, which is generated at the short wavelength side is referred to as the signal and at the long wavelength side as the idler. It can be seen, that the ZDW is a crucial design aspect for the FWM process.

4. Fundamentals of Optical Fibers

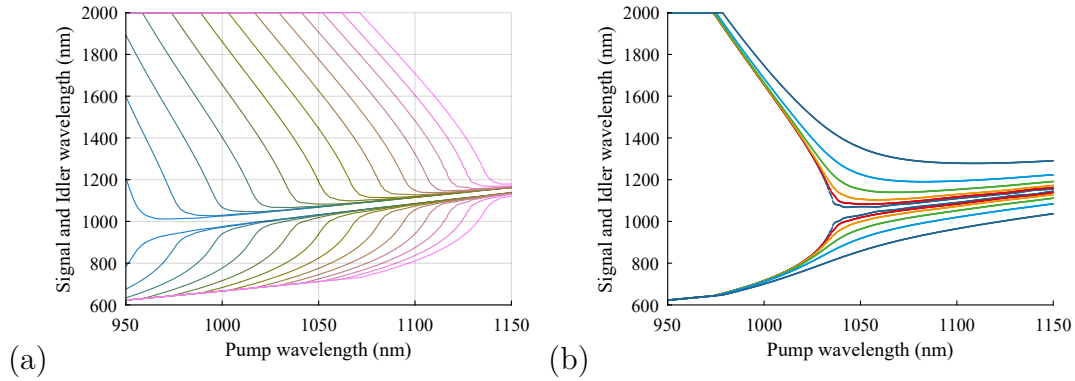


Abbildung 4.7: (a) Phase-matching diagrams for ESM structures versus pump wavelength with Λ varied from 2 to 5 μm (blue to pink) and constant $d/\Lambda = 0.5$ for a pump peak power of $P_{\text{pump}} = 1 \text{ kW}$ (b) Phase-matching diagrams for a ESM fiber with $\Lambda = 3.25 \mu\text{m}$ and $d/\Lambda = 0.5$ at different pump peak powers of 0.3, 1, 3, 10, 30, 100 kW .

By pumping these fibers within the Ytterbium gain bandwidth (see chapter 4.4), signal wavelengths starting from $\sim 600 \text{ nm}$ can be generated. The signal wavelengths can be generated close to the pump wavelengths when pumping close to the ZDW. As can be seen in figure 4.7, the idler wavelengths can easily reach wavelengths beyond $2 \mu\text{m}$, where the transparency window of fused silica starts to close. The influence of the peak-power on the phase-matching is shown in figure 4.7 (b). At low peak powers the signal and idler branches meet at the ZDW. At longer wavelengths, where the dispersion in the conversion fiber is anomalous, the spectral position of the gain peak for signal and idler conversion is mainly dependent on the peak-power P_{pump} . Theoretically, with a vanishing pump peak power, the gain peak for the signal and idler wavelengths falls exactly at the pump wavelength and the gain bandwidth becomes 0. FWM in the anomalous dispersion region is traditionally called modulation instabilities.

FWM in the normal dispersion region is, in contrast, much more dependent on the structure of the fiber and its ZDW. Here a change in peak power causes the gain-peak wavelength to shift only slightly.

In this study a single fiber design is identified which will be employed in a conversion setup to accommodate the requirements for a tunable fiber-laser source based on FWM. The commercially available EMS fiber called LMA 5-PM ($\Lambda = 3.25$) by NKT photonics is very well suitable for this task. Pumping this fiber with a peak power of 1 kW between 1025 and 1055 nm results signal wavelengths between 770 and 970 nm. Hence, Raman resonances between 3230 and 830 cm^{-1} can be addressed with the resulting signal and residual pump wavelengths.

4.3.5 Supercontinuum Generation

A super-continuum is commonly described as the generation of an ultra-broad spectral continuum from a narrowband pump laser. The origin of supercontinuum generation is strongly dependent on the pump pulse parameters and the conversion medium. In the case of optical fibers, the fiber material and its structure can influence and limit the conversion process, e.g. by material absorption. While SPM (chap. 4.3) and soliton fission (eq. 4.24) are the most important processes for femtosecond pump pulse durations, four-wave mixing and Raman scattering become dominant when the pump pulse duration is in the picosecond or nanosecond range [50–52]. Additionally, the spectral position of the pump with respect to the zero dispersion wavelength of the fiber is important [53]. After an appropriate narrowband filtering, super-continuum generation supports every possible wavelength combination for CRS applications. However, the filtered laser lines contain only a tiny fraction of the original pump peak power and average power.

4.4 Active Fibers

Another advantage of fibers is the ability to dope the core material with laser-active ions to create an amplifying waveguide. Usually, these fibers are pumped with diode lasers emitting at a wavelength which can, directly or indirectly, create inversion of the active ions. Common doping materials are Ytterbium (Yb), Erbium (Er) and Thulium (Tm), which are all rare-earth elements. Figure 4.8 depicts the absorption and emission cross-section of the Yb^{3+} ion in Germano-silicate glass. Yb has the advantage of having a very low quantum defect and a high quantum efficiency allowing for the operation with high average power and amplification efficiencies when pumped at 976 nm. This pump wavelength is also very attractive as there are high brightness pump diodes commercially available making Yb-doped fiber amplifiers the premier choice for compact high-power laser sources. Due to the low quantum defect², conversion efficiencies of 80% have been demonstrated [54].

²The quantum defect is one minus the energy ratio between the signal and pump photons and marks the maximum conversion efficiency in a laser process.

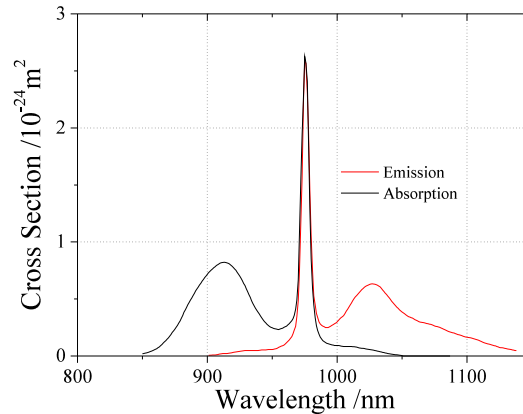


Figure 4.8: Absorption and emission cross section of the Yb^{3+} ion in Germano-silicate [?, 55].

Ytterbium-doped fiber lasers can be either core-pumped or cladding pumped. Core pumping means that a pump laser at 976 nm or around 915 nm is directly coupled to the core of an active fiber. If this fiber has single-mode guiding properties, the pump radiation also has to be spatially single-mode in order to couple the pump light efficiently to the active single-mode fiber. Today, single-mode pump diodes are limited to one semiconductor emitter. Therefore, the available pump power is limited to ≈ 1 W. The great advantage of such a pump scheme is that the pump is absorbed within a very short length of the active fibers, which allows the construction of extremely compact amplifiers with a very low accumulated B-Integral during amplification (eq. 4.16).

In contrast, cladding pumped amplifiers offer orders of magnitude higher average powers. The pump radiation propagates in the cladding of the fiber with a high numerical aperture (NA). Therefore, the pump light only needs to be focused to the pump core, which allows the spatial incoherent combination of many single diode emitters and, therefore, several kW of pump power. The pump light is penetrating the signal core with a rate equal to the ratio of the signal to pump core area. Therefore, the pump light is only absorbed efficiently if the active fiber length is much longer than in the core-pumped case. Hence, the accumulated B-Integral is much higher compared to the core-pumped scheme at the same converted signal power and pump power for a given core diameter.

Due to the broad emission spectrum of Yb, both broadband [?, 56] and also widely tunable laser sources have been demonstrated [57, 58]. Thus, the combination of FWM with a wavelength tunable Yb-based pump source is a promising choice to exploit the broadband phase-matching characteristics of ESM fibers.

4.5 Mode-Locked Lasers

Many applications such as CRS benefit from ultra-short pulses instead of continuous wave (cw) radiation. The pulses may have several kW of peak power with only mWs of average power. Thus, non-linear effects can be triggered without causing heat-related damage in the sample. To generate pulses with picosecond to femtosecond durations, a technique called mode-locking may be employed. To understand the physics of mode-locking, a laser cavity of length L with an optical path length of $L_{opt} = n_{eff}L$ is considered. If the gain bandwidth of the gain medium is much broader than the longitudinal-mode spacing $\Delta\nu = c/L_{opt}$ and the gain is higher than the losses in the cavity, several longitudinal modes can reach the oscillation threshold simultaneously. The resulting electrical field will be the sum of all of these modes and can be written as [30]:

$$E(t) = \sum_{m=-M}^M E_M \exp(i\phi_m - i\omega_m t) \quad (4.33)$$

where E_M , ϕ_m and ω_m are the amplitude, phase and frequency of the m -th mode within the cavity. The total number of modes is $2M + 1$. If the phases of the modes change randomly with time, the total intensity of the light field $|E(t)|^2$ will be time independent, which represents the case of cw laser operation. The situation changes if the phases of adjacent modes are locked to a constant difference $\phi = \phi_m - \phi_{m-1}$. The phase of the modes can then also be written as $\phi_m = m\phi + \phi_0$ and the mode frequency can be written as $\omega_m = \omega_0 + 2m\pi\Delta\nu$. If, for simplicity, every mode has the same amplitude eq. 4.33 can be written for the mode-locked case as [30]:

$$|E(t)|^2 = \frac{\sin^2[(2M+1)\pi\Delta\nu t + \phi/2]}{\sin^2(\pi\Delta\nu t + \phi/2)}. \quad (4.34)$$

The now time dependent intensity of the overall field is periodic with a period time of $\tau_r = 1/\Delta\nu$, which is the round-trip time of the oscillator cavity. The full-width half maximum (FWHM) pulse duration in the mode-locked operation is then $\tau_p \approx [(2M+1)\Delta\nu]^{-1}$. As $(2M+1)\Delta\nu$ corresponds to the overall bandwidth of the pulse, its temporal duration is inversely proportional to its bandwidth in accordance with Fourier theory.

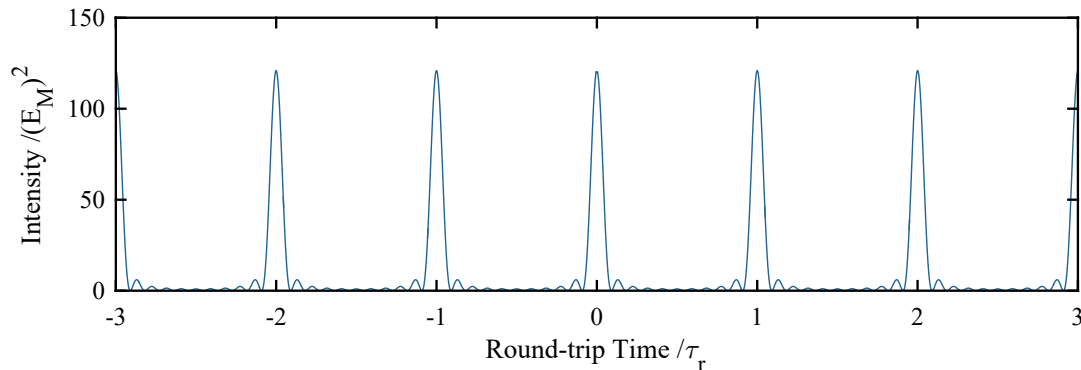


Figure 4.9: Mode-locked pulse train for 11 longitudinal modes of equal amplitudes

Mode-locking can be achieved by an active or passive element [59]. Active mode-locking can be achieved, for example, by using an acousto-optical modulator or an electro-optical modulator with a modulation frequency equal to the inverse of the round-trip time of the cavity. Passive mode-locking usually involves an element which has an intensity-dependent response to the light field. This way, an incoming pulse is absorbed at the pulse front more than at the pulse center, where the intensity is high enough to saturate the absorption. Thus, the pulse becomes shorter after transmission. In a laser cavity, this leads to a preference for short pulses over longer pulses, as shorter pulses minimize the losses of the cavity. One of the most simple and robust implementations of such an element is a saturable absorber mirror. Such an element consists of a Bragg-mirror with a high reflectivity for the signal wavelength on a semiconductor substrate made from e.g. GaAs. The mirror is covered by a layer of absorbing material which saturates at a certain fluence [60].

4.6 Similariton Lasers

There are many different operation regimes for mode-locked lasers depending on the sign and magnitude of the dispersion in the laser cavity at the operation wavelength. One of the most prominent laser concepts is the soliton laser, where anomalous dispersion and self-phase modulation balance each other out [61]. However, this operation regime limits the peak powers to < 1 kW and the pulse energy to ~ 0.1 nJ when operated in standard single-mode step index fibers. These limitations arise from the soliton fission in the presence of higher order dispersion (see Chap 4.3.3, eq. 4.24), but can be somewhat circumvented by adding two elements with high amounts of GVD with the opposite signs in the cavity. This results in a cyclic

stretching and compression of the oscillating pulse. Consequently, the average peak power is reduced during the oscillations allowing for higher compressed peak powers at the output. With these so-called stretched-pulse or dispersion-managed solitons, peak powers in the range of ~ 10 kW are feasible [62,63]. Another option is to use fibers with very large mode field diameters in order to reach high pulse energies from a fundamental soliton (see eq. 4.21). For example in [39] 15 nJ of pulse energy at 1700 nm and up to 45 nJ at 2100 nm were obtained. Although these values are very impressive, they were not demonstrated inside a laser cavity. In order to reach even higher output pulse energies, the ability to produce transform-limited pulses has to be sacrificed. In so-called all-normal dispersion lasers, the pulse is stretched throughout the laser cavity. In the steady state, the pulse duration monotonically increases during each round-trip. Simultaneously, SPM causes the pulse width to increase proportionally. Then, via spectral or temporal filtering, the chirped pulse is trimmed back to its initial pulse duration before completing the round-trip, this achieves consistency. The output of these laser has to be temporally compressed (e.g. via grating compressors) in order to reach its minimal pulse duration. This feature is not necessarily a disadvantage as the pulse duration in fiber amplifier systems is usually artificially increased anyways in order to keep the peak power low during amplification.

This kind of pulse generation is, therefore, quite different compared to soliton and dispersion-managed solitons. These pulses are called Similaritons as their temporal and spectral shape change in a self-similar fashion [64]. The resulting parabolic shaped pulses feature steep edges in the spectrum and a parabolic spectral phase. Therefore, these pulses can be easily compressed close to their transform-limited pulse duration. Pulse energies of 900 nJ with compressed pulse durations below 100 fs resulting in peak powers of 7 MW have been achieved by combining this operation regime with large mode area fibers [65].

The concept of normal dispersion fiber laser cavities have the potential to reach the highest pulse energies and peak powers and they will be combined in this work with the parametric gain provided by four-wave-mixing in order to generate tunable, energetic pulses for biomedical imaging applications (see chapter 4.3.4)

5 All-Fiber Widely Tunable Optical Parametric Oscillator

The goal of this work is to find an all-fiber solution able to fulfill the laser parameter requirements of CRS and MP imaging. Even though other concepts based on free space optics have already been able to deliver such parameters, but have proven to be widely impractical for applications outside specialized laser laboratories.

5.1 Narrow-Band Four-Wave-Mixing-Based Optical Parametric Oscillator

The key component for a tunable, narrow-band, FWM-based conversion is a highly dispersive optical parametric oscillator. In this work it consists of an input-coupler, a conversion fiber, an output-coupler and a relatively long feedback fiber. Since the dispersion of the cavity results in different round-trip times for each wavelength, either the FWM generated signal or the idler wavelength can be synchronized with the pulses of the pump radiation.

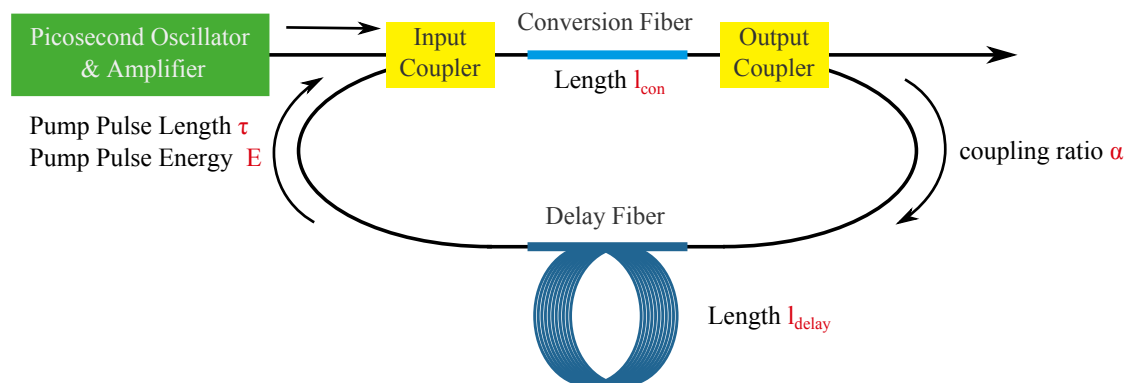


Figure 5.1: Scheme of a fiber-based OPO

If its wavelength fall within the normal net-dispersion region of the cavity, the pulses may be generated as in a mode-locked oscillator with a normal-dispersion

cavity, which has been discussed in chapter 4.6. The main difference here is that the gain is produced by FWM instead of by an active laser medium. Thus, for instance, if the signal after the round-trip in the FOPO cavity overlaps with one of the subsequent pump pulses, a stable solution may form provided that the losses in the cavity are compensated by the FWM gain and that the spectral and temporal shape of the signal is reproduced after one round-trip (for a stable, uniform output). Figure 5.1 shows the schematic setup of the FOPO and the main parameters that influence its behavior. In an attempt to gain a deeper insight in the operating principle of the cavity, a series of simulations have been done. However, first the function and design of the filter mechanism that ensures narrowband, tuneable wavelength generation is introduced.

5.1.1 Passive Dispersive Filter

In chapter 4.3.4 (equation 4.29) the bandwidth dependence of the parametrically generated signals on the pump wavelength and the pump peak power in a specific ESM fiber has been discussed. Additionally, it is known that narrow linewidth excitation is required to enable high chemical-sensitivity in CRS microscopy. Consequently, a spectral filter has to be used in order to decrease the spectral bandwidth of the signal and idler waves that are oscillating in the fiber cavity. Without this bandwidth reduction, the spectral bandwidth of the signal is in the order of 3 nm at 800 nm and a few tens of nm at 950 nm when pumped at 1030 nm [17,66]. The most straightforward way to reduce the spectral bandwidth is to use a narrow dielectric filter or a spatially dispersive element (prism or dielectric grating) to select a signal or idler wavelength. This method has been used in a FOPO to reduce the signal bandwidth and enable signal tuning [67]. The disadvantage of his approach is that the tuning of the signal is limited by the tuning range of such filters, which is usually much narrower than the tuning capabilities of FWM. Furthermore, there are high intrinsic insertion losses associated with these filters which are based on bulk optics and require fiber coupling to be compatible with the FOPO. Lastly, for a constant turning the realigning of the filter elements lead to complex and maintenance-intensive setups. Moreover, for dielectric filters, the bandwidths are, due to technical reasons, wider than the bandwidths required for CRS imaging. In the end, a fiber-based filter method is required, which has a low insertion loss and works for a wide spectral bandwidth. A filter that fulfills all these requirements is a passive dispersive filter [68,69].

The idea is to employ a long piece of polarization-maintaining optical fiber to

5. All-Fiber Widely Tunable Optical Parametric Oscillator

introduce a large amount of chromatic dispersion for the oscillating signal or idler pulse in the FOPO cavity. In the following description, the cavity has been assumed resonant to the FWM signal wavelength. The initial pump pulse generates both a signal and an idler pulse in the ESM fiber. These pulses are generated from noise and roughly cover the gain bandwidth of the FWM process. The main of this initially broad signal is coupled out of the cavity and the rest is fed back to the input-coupler through the feedback fiber. These pulses are consequently temporally stretched out by the chromatic dispersion they experience during their propagation along the fiber. For better understanding, the propagation time ($\tau = l_{fiber}\beta_1$) of light pulses (with very narrow bandwidths) at different wavelengths is plotted over their central wavelength after a propagation through 200 m of fused silica. In figure 5.2(a) it can be seen that, for instance, two pulses at 1200 nm and 600 nm will arrive with a 10 ns time difference at the end of the silica medium. This corresponds to a spatial separation of over three meters in air.

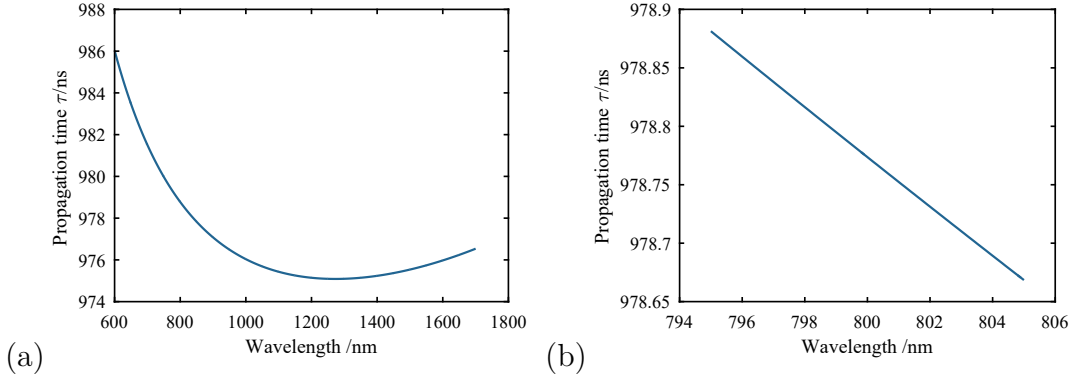


Figure 5.2: (a) Propagation time needed for different spectral components to go through 200 m of fused silica length. (b) detailed view around 800 nm.

This way, by adjusting the length of the feedback fiber, it is possible to force that either the signal or the idler pulses overlap in time with the next pump pulse. When this condition is fulfilled then we talk about a cavity resonant to the signal or to the idler pulse. On the other hand, the spectral components of a pulse with a bandwidth of 5 nm at 800 nm will be stretched in time by 100 ps. This means that a successive pump pulse with a typical pulse duration of 40 ps will only overlap with a section of the stretched pulse. Consequently, only part of the feedback pulse contributes as a seed for the parametric process. Thus, the following signal pulses will become more narrowband with each round-trip until the influence of the dispersion of the delay fiber becomes negligible (because its impact is proportional to the spectral bandwidth of the feedback pulse).

5. All-Fiber Widely Tunable Optical Parametric Oscillator

Parameter	Value, OPG	Value, OPO
ESM fiber length l_{con}	50 cm	50 cm
pump pulse energy E	100 nJ	80 nJ
pump pulse duration (FWHM) τ	40 ps	40 ps
pump wavelength λ_{pump}	1033 nm	1033 nm
feedback fiber length l_{delay}	-	200 m
Feedback ratio α	-	-20 dB

Table 5.1: Parameters for OPG and OPO operation

The filtering effect is, therefore, based on dispersion and temporal gain narrowing. Such a filter is virtually lossless and, depending on the fiber length, can become very narrow. As the filter works for any wavelength as long as the group velocity dispersion is significant, it can be used over a very large spectral range. It works purely within optical wave-guides and it is completely maintenance-free. On the down-side, the filter works only with parametric amplification or stimulated Raman scattering as the conversion has to be instantaneous. This filter method is, therefore, not applicable to classic laser active media. Furthermore, since the dispersion is in general different for each wavelength, the filter characteristic changes too. This can be advantageous if one wants to e.g. convert to pulses, supporting femtosecond durations (see section 6.2) near the zero dispersion wavelength (ZDW) of the cavity. On the other hand, if one operates the dispersive filter far from the ZDW, the relative change of the filter bandwidth becomes weak.

5.1.2 Reaching the Steady State

As it has been described earlier, pumping a suitable ESM fiber with a certain pump wavelength and a sufficient pump pulse peak power leads to the extinction of two pump photons and the generation of a signal and an idler photon. If there is no external seed within the gain bandwidth produced by FWM, the quantum noise of the matter acts as a seed signal, which is amplified by FWM. This so-called optical parametric generation (OPG) roughly fills the gain bandwidth of the FWM process. Figure 5.3 depicts a numerical simulation of the OPG process when using a ESM fiber with a $d/\Lambda = 0.5$ and a hole to hole distance $\Lambda = 3.25\mu\text{m}$ (see section 4.3.4) with the parameters given in table 5.1.

The simulation has been done 100 times in order to generate an average signal shape, where the quantum noise is randomly generated for each simulation. The average was fitted with a Gaussian curve in order to simulate the signal shape one could expect to measure with a spectrometer averaging over millions of pulses.

5. All-Fiber Widely Tunable Optical Parametric Oscillator

As the pump peak power increases, the spectral bandwidth becomes broader, due to the intensity dependent phase-matching condition (see equation 4.29). The signal and idler intensity increases until the the radiation is converted back to the pump again [45, 66]. The maximum conversion to the signal reaches under normal conditions $\approx 10\%$. One way to increase the efficiency is to absorb the idler radiation [70]. In this case the pump to signal conversion efficiencies can reach up to 35%.

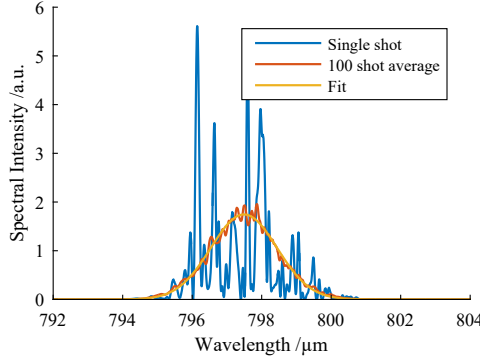


Figure 5.3: Optical parametric generation for parameters according to table 5.1. The blue curve represents one randomly chosen OPG signal. The red curve is the average of 100 OPG signals and the yellow curve is a Gaussian fit.

It is obvious that the OPG signal and idler are different for each pulse and, therefore, this spontaneous generation is not suitable for SRS measurements, where a low noise laser radiation is required. On the other hand, it is still possible to perform CARS measurements with a low chemical specificity as demonstrated in [66, 71].

Following the schematic setup shown in figure 5.1, a fraction α from the generated signal is sent back through the dispersive delay line and overlapped with one of the subsequent pump pulses. As described earlier, part of the initial OPG radiation seeds the next FWM conversion and, in the process, is filtered to a narrower signal and idler pulse. The evolution of the generated spectra over the first thirty oscillations is depicted in figure 5.4. It can be seen how the signal is generated, filtered to under 1 nm bandwidth and finally reaches a peak power where the propagation through the delay and conversion fiber leads to spectral broadening due to SPM (see also figure 5.5). The broadening effect is again limited by the dispersive filter. Finally, the steady-state is characterized by very clean pulses with very low pulse to pulse fluctuations after only 10 oscillations. It is already clear that this method offers a much better pulse stability than OPG.

5. All-Fiber Widely Tunable Optical Parametric Oscillator

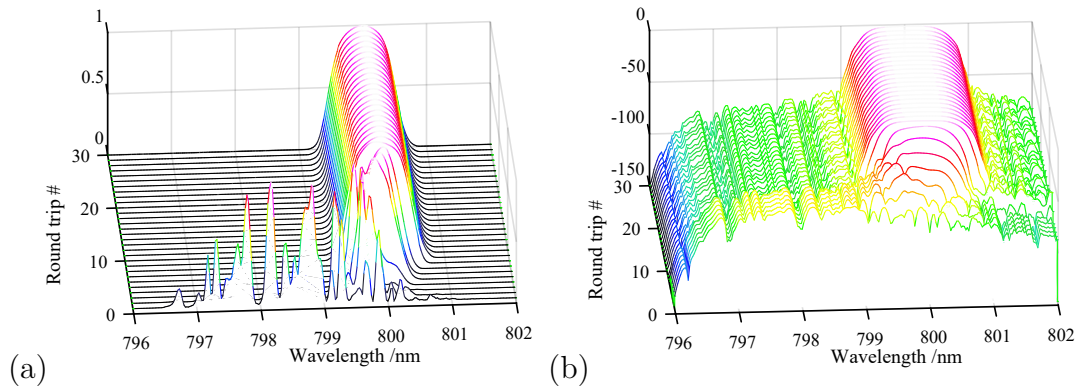


Figure 5.4: Optical parametric oscillations for parameters according to table 5.1. (a) Linear and normalized spectra of the signal pulse for the initial thirty oscillations. (b) The same spectra in logarithmic scale

The bandwidth settles at 1.0 nm which is much narrower than the gain bandwidth of the FWM process.

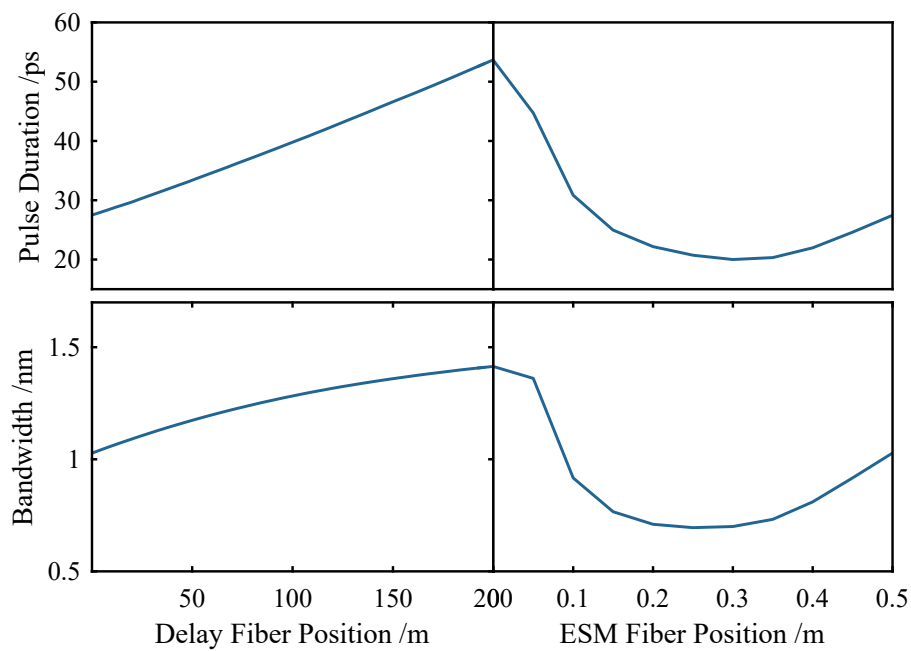


Figure 5.5: Bandwidth and pulse length evolution of the signal pulse within a single round-trip in the steady-state.

To gain further understanding of the pulse dynamics within a single round-trip, the signal bandwidth and the length of the signal pulse have been plotted in figure 5.5.

The simulation starts at the output-coupler, where 99% of the signal power is coupled out and 1% is sent back through the dispersive delay line. SPM broadens

5. All-Fiber Widely Tunable Optical Parametric Oscillator

the pulse to a bandwidth of 1.4 nm and dispersion stretches it to a pulse duration of 53 ps. When the feedback pulse is superimposed to one of the subsequent pump pulses (40 ps pulse duration), only part of the pulse will be amplified and, therefore, due to its temporal chirp, become more narrowband. After 25 cm of propagation in the ESM fiber, the bandwidth of the pulse reaches a minimum of 0.7 nm. Up to this part of the fiber the pump is still undepleted and the gain is purely exponential. Afterwards, as the pump pulse is depleted the wings of the pulse are amplified stronger than its center and, as a result, the pulse becomes broader and longer, and recovers its original bandwidth and pulse duration of 1.0 nm and 28 ps respectively. The circulating pulse, therefore, dynamically changes its spectral width and duration. The cavity behaves, in part, as a normal dispersive fiber oscillator [72] (see section 4.6) where the gain is provided by FWM and the necessary spectral filtering happens in the ESM fiber.

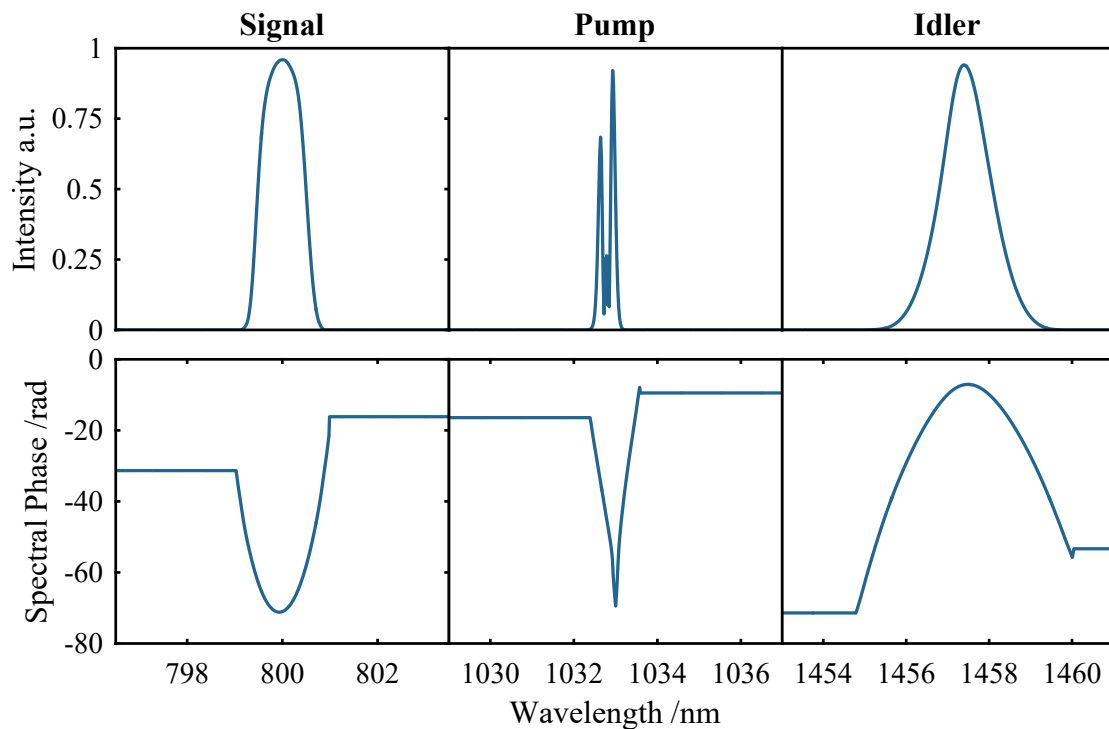


Figure 5.6: Spectral intensities and phases at the output of the FWM-driven FOPO cavity for the signal (left column), the pump (center column) and the idler (right column).

A pulse with a linear chirp exhibits a spectral phase with a parabolic shape. The FWM-based FOPO shows the same behavior as a normal dispersion fiber oscillator as it is shown in figure 5.6. Figure 5.6 depicts the spectral intensity and phase of the FOPO signal, pump and idler at the output of the cavity. The

spectrum of the signal pulse (left column) features steep spectral edges, which are typical for normally dispersive laser cavities, and the aforementioned parabolic spectral phase. The depleted pump pulse features side-lobes, which are typical for SPM broadened pulses (center column). Finally, the idler pulse (right column) also features a parabolic spectral shape but with a different sign. The idler pulse compensates for the phase of the signal pulse. This feature is called optical phase conjugation [73, 74]. Now that the behavior of a typical FOPO cavity has been discussed, its wavelength tuneability is explored.

5.1.3 Tuning the FOPO

In the simulation of the previous section, the dispersive filter was tailored to generate a signal at 800 nm by setting the velocity of the moving frame in the simulation to the group velocity of the signal pulse at 800 nm. This way, the desired signal wavelengths remains in the center of the temporal simulation window. The pump pulse is then superimposed at the center of this moving frame. One could also say that the repetition rate of the signal at 800 nm has been synchronized to the pump repetition rate. In practice, the tuning of the signal wavelength is accomplished either by changing the pump repetition rate or by changing the FOPO cavity length. The FOPO remains oscillating if the signal is still within the FWM gain bandwidth provided by the pump and if the gain at this signal wavelength is still able to compensate for the losses in the cavity.

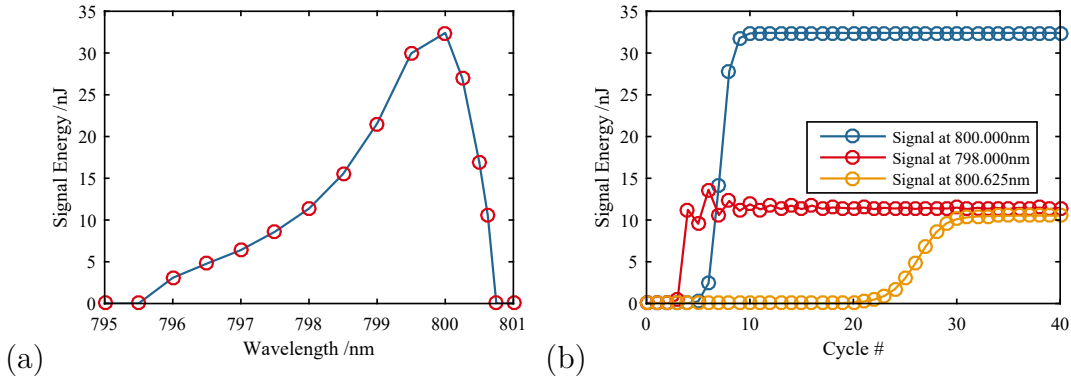


Figure 5.7: (a) Signal energy tuning curve for the FOPO parameters defined in 5.1. (b) Signal energy evolution for different signal wavelengths.

Figure 5.7(a) depicts the signal energy for different group velocities of the signal pulse with respect to the pump pulse in the delay fiber. It might be surprising that the tuning curve of the extracted pulse energy is not symmetric as the OPG spectrum. The asymmetry can be explained by phase-matching at high conversion

efficiencies. In the high gain/low conversion efficiency case (see eq. 4.30), the phase-matching only depends on the peak power of the pump. In the case of high conversion efficiencies, however, the phase mismatch also depends on the peak power of the signal and idler waves [75]:

$$\Delta\beta = \Delta\beta_0 + \gamma(2P_{pump} - P_{signal} - P_{idler}). \quad (5.1)$$

For higher signal and idler powers, the power difference in the brackets in equation 5.1 becomes smaller. Thus, $\Delta\beta_0$ also becomes smaller to fulfill the phase-matching condition at $\Delta\beta = 0$. As it was introduced in equation 4.30, $\Delta\beta_0$ corresponds to the location of the gain peak. Consequently, the gain maximum shifts for high conversion efficiencies from the center of the phase-matched spectral region towards the pump wavelength [76].

The transient response is, therefore, quite different for signal wavelengths close to or far from the pump wavelength within the FWM gain spectrum as can be seen in figure 5.7b. In the simulation both filter positions at 798.000 and 800.625 nm lead to a signal pulse energy of about 10 nJ. At 798.000 nm (red curve in figure 5.7(b)), however, the initial signal increase is fast as the signal wavelength is close to the small-signal gain peak. In this situation it takes only 4 cycles to achieve significant conversion. During following cycles, the signal energy oscillates about its final value and converges slowly to its steady state value. This oscillation occurs because a high seed-signal energy causes the gain peak to shift away from 798.000 nm which results in a lower signal gain. Consequently, the next cycle starts with a lower seed signal which experiences now a higher gain. At 800.625 nm the picture is very different. The small-signal gain at this wavelength is very small and it takes many signal round-trips in order to shift the gain peak towards higher wavelengths (yellow curve in figure 5.7(b)). The signal energy then becomes stronger and saturates. Figure 5.7(b) shows the evolution of the pulse energy of the signal over the initial 40 cycles at both wavelengths. At 800.000 nm (blue curve) at which the highest signal conversion efficiency is reached, the initial signal gain is small compared to the signal at 798.000 nm but higher than at 800.625 nm. The gain peak then shifts with the signal energy towards 800.000 nm leading to a fast onset of the steady state. The stability is consequently the highest at this wavelength. This shift of the gain maximum is important for the FWM-based conversion as the effects of gain and non-linear phase (second term in equation 5.1) depends both on χ^3 -non-linearities. Therefore, both effects are equally important. Compared, for instance, to parametric conversion processed based on χ^2 -non-linearities, the

non-linear phase during the conversion plays a minor role and can be neglected.

5.1.4 Influence of the Feedback Fiber Length

One of the easiest parameters to analyze is the length of the feedback fiber. Its length influences the bandwidth of the dispersive filter and enables the synchronization of the signal oscillation frequency in the FOPO cavity with the pump repetition rate. By increasing the fiber length, the bandwidth of the dispersive filter becomes narrower. This is due to the increased dispersion and, therefore, to the longer feedback pulse length. The signal, consequently, becomes narrower not only due to the filtering alone, but also due to the reduced effective feedback ratio caused by the filter¹. Figure 5.8 depicts the FWHM bandwidth of the signal for fiber lengths from 1 to 1000 m in logarithmic scale.

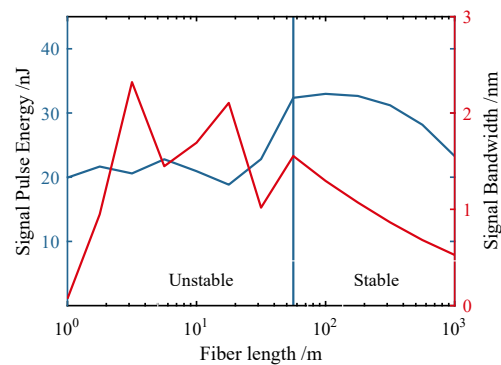


Figure 5.8: Influence of the feedback fiber length on the signal bandwidth.

If the fiber length is not long enough, the dispersive filter is too weak and the oscillation is unstable. When the fiber length reaches about 50 m, the FOPO becomes stable. At this point the signal bandwidth reaches its maximum of 1.5 nm while longer feedback fibers lead to narrower signal pulse spectra.

As mentioned before, for the tuning to work, it is not important whether the repetition rate of the pump pulses or the FOPO cavity length is changed. In practice, the FOPO cavity length may be chosen to be much longer than it would be necessary due to the pump repetition rate. For instance, in order for the FOPO cavity to be resonant with a pump repetition rate of 10 MHz, the delay fiber length only needs to be about 20 m. However, if the delay fiber length increases by multiples of 20 m, multiple signal pulses oscillate in the cavity at one time. In this

¹Since the temporal overlap with the pump pulse decreases with an increase of the feedback pulse length, the effective seed energy decreases as well.

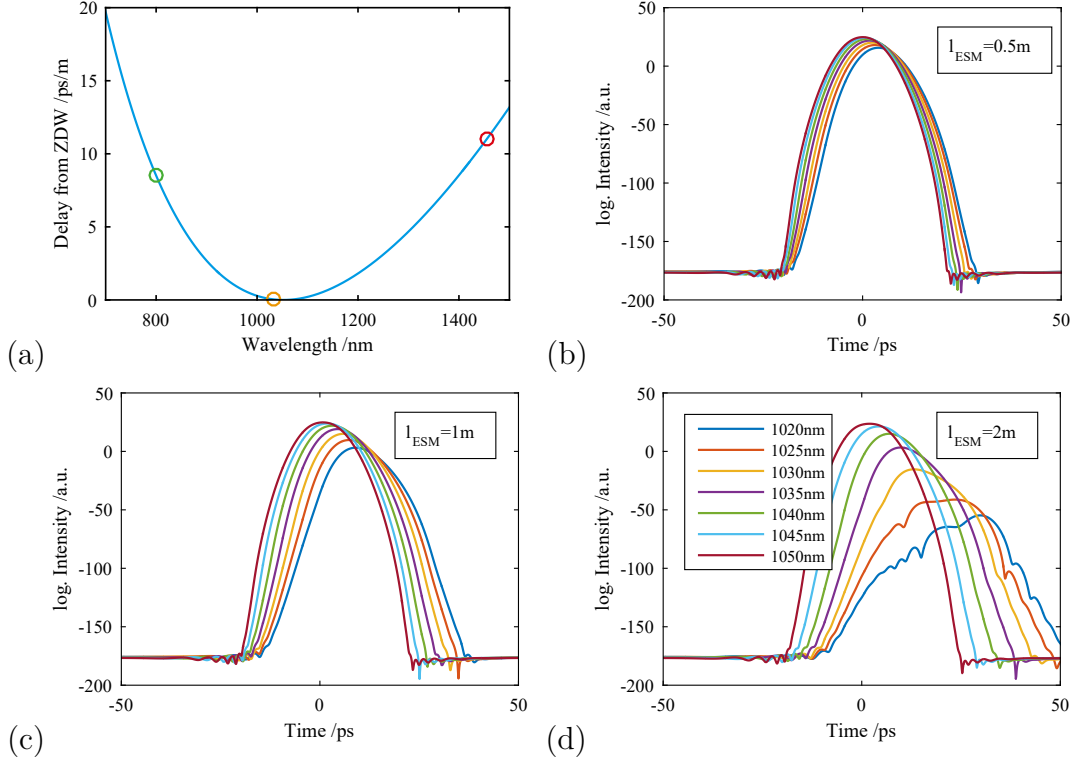
case, the signal pulse is not fed to the first following pump pulse but to one the pulses following it.

5.2 Temporal Walk-Off During Conversion

Up to now the length of the conversion fiber has been kept constant. Equation 4.28 states that the FWM small-signal gain is only dependent on the B-Integral within the ESM fiber. Thus, if the B-Integral $B = \gamma P_{pump} l_{con}$ is kept constant, the FWM gain should also be preserved. The nonlinear parameter $\gamma = \frac{4n_2\omega_0}{\pi c} d_{eff}^2$ depends only on the fiber parameters and on the central wavelength. Therefore, the conversion fiber length can be changed if the pump power is also altered accordingly. Of course, other parameters such as the gain bandwidth are primarily depend on the pump peak power and are, thus, not going to be constant. If the conversion efficiency is constant, it would be straightforward to maximize the signal energy by using a short piece of conversion fiber and increase the pump power accordingly. In essence, this was one of the aspects exploited in the development of the FOPO for multi-photon imaging [77]. On the other hand, if the pulse peak power is limited by the amplifier system, one could suggest to simply increase the conversion fiber length to reach the necessary FWM gain value. This is where the temporal walk-off of the signal with respect to the pump plays an important role.

This issue is caused by the different group velocities of the pump and the signal light. The transit time through the ESM relative to the minimum (obtained at the ZDW) is plotted in figure 5.9. After 1 m of such a fiber the pump and signal pulses at 1033 nm and 800 nm, respectively are shifted from one another by over 8 ps. If the pump pulse duration is in the order of this delay, the effective conversion fiber length is reduced below its physical length. Figure 5.9 depicts the change of the OPG signal for different ESM fiber lengths at constant B-Integrals. While for a fiber length of 0.5 m the conversion efficiency at different pump wavelengths deviates only by a small amount (see figure 5.9(b)), longer conversion fiber lengths result in a stronger walk-off and, therefore, in a decreased conversion efficiency (see figure 5.9(c) and (d)).

5. All-Fiber Widely Tunable Optical Parametric Oscillator



Pump Wavelength /nm	Signal Wavelength /nm	Walk-off /ps/m
1020	745	13.0
1025	764	11.0
1030	785	9.5
1035	810	7.4
1040	839	5.7
1045	873	3.6
1050	915	2.1

(e)

Figure 5.9: (a) Transit time relative to that at the ZDW group-velocity. (b-d) Effect on the OPG signal for different pump wavelengths and resulting walk-off lengths after 0.5, 1 and 2 m of ESM fiber with constant B-Integral. The pump pulse length is 40 ps and the pump peak power set to 4 kW for 0.5 m of ESM fiber. (e) Walk-off between the pump and signal pulses.

For 2 m of conversion fiber and a pump wavelength of 1030 nm, there is a signal decrease of 35 dB compared to the conversion in 0.5 m. This difference is caused only by a change in walk-off from 4.75 to 19.0 ps (see figure 5.9(e)). Consequently, the choice of the conversion fiber length in a FOPO is highly dependent on the pump pulse length. While a length of 50 cm of conversion fiber is short enough for wide spectral conversion with pump pulse lengths of 40 ps, shorter pump pulses can only convert efficiently within proportionally shorter fiber lengths.

In the end a minimum amount of *pump energy* is required to be able to convert light over a wide spectral range. If the pump pulses are long, the conversion fiber can be long in order to convert light with a required pump peak power. If the pump pulses are chosen to be short, the length of the conversion fiber has to become shorter in order to avoid the detrimental walk-off effect. Short conversion lengths, on the other hand, require more peak power to generate the same FWM gain. Therefore, it does not matter how long the pump pulses are, there is always a certain amount of pump pulse energy required to avoid a strong walk-off induced-FWM loss of gain within the appropriate conversion fiber length. This fact has severe consequences when working with all-fiber components and limited pump energies. If the application requires a certain pulse repetition rate (e.g. 20 MHz for SRS imaging), the amplifier system needs to provide a certain amount of average power, which is technically limited. In the end, the FOPO concept is limited by the amplifier system.

5.3 Influence of Self-Phase-Modulation Broadened Pump Pulses on the Conversion Process

Up to this point, the pump radiation was considered to be transform-limited. This means, for example, that a Gaussian pump pulse with 40 ps of duration has a spectral bandwidth of only 40 pm (at 1 μm central wavelength). As the main goal of this thesis is the construction of an all-fiber laser source for CRS imaging, the pump pulse generation and amplification is accompanied with a significant propagation through optical single-mode fiber. In the previous section, it was established that the widely tuneable generation within a FOPO cavity requires a certain amount of pulse energy. Therefore, a large amount of SPM might broaden the pump pulses before they reach the input of the ESM fiber. In a standard optical single-mode fiber at $\lambda = 1030 \text{ nm}$, the nonlinear parameter is $\gamma = 0.008 \frac{1}{\text{Wm}}$. The non-linear phase accumulated by a pump pulse with a peak power of 1.8 kW, which propagates half a meter from the last amplifier to the ESM fiber, can reach values around $B = 30 \text{ rad}$. With the help of equation 4.18 it is possible to calculate the pump pulse broadening to 0.33 THz or 1.2 nm. Thus, each spectral slice of the broadened pulse becomes phase-matched to a different signal wavelength. Additionally, as the SPM broadening causes the pump pulses to become chirped, the phase-matched amplification happens at different temporal sections of the pulse. Together with the already complex signal generation in the FOPO cavity, this premise leads to an

5. All-Fiber Widely Tunable Optical Parametric Oscillator

even more complex temporal and spectral pulse evolution to and during the steady state. The influence of this effect was simulated by first imposing a nonlinear phase to a transform-limited pump pulses of 40 ps duration. The maximum phase was varied from 0 to 30 *rad* and the spectral intensity of the resulting pulse has been plotted in figure 5.10a.

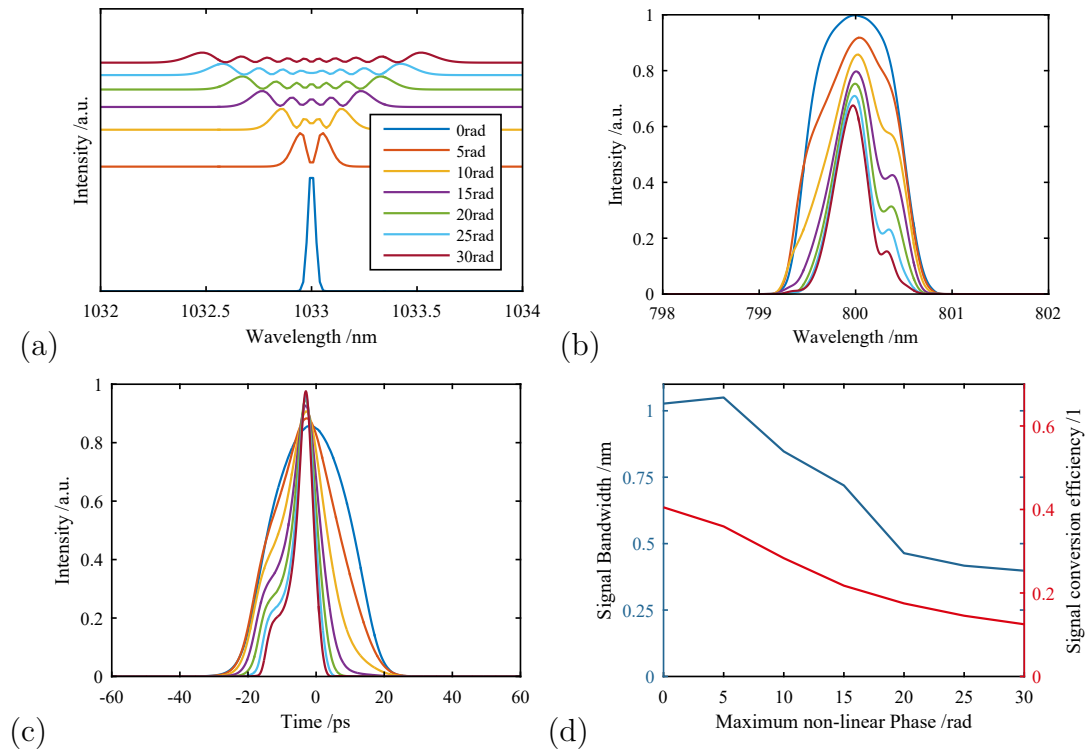


Figure 5.10: Influence of the non-linear phase accumulated in the amplifiers: (a) on the pump pulses, (b) on the signal spectrum, (c) on the temporal signal pulse shape and (d) on the signal conversion efficiency.

The resulting behavior of the signal pulse is illustrated in figure 5.10 (b-d). With the increase in accumulated phase of the pump pulses, the signal pulses become shorter and the conversion efficiency decreases. This effect becomes clear when the limited phase-matching of the broadband pump pulses is considered. If the FOPO cavity is resonantly pumped to an oscillating signal wavelength at 800 nm, only a narrowband part of the chirped pump pulses is phase-matched to this signal wavelength. Consequently, the generated signal pulse length is becoming significantly shorter than the pump pulses. The decrease in signal pulse duration increases the filter effect of the dispersive delay line, which lets the signal pulses become even more narrowband. This results in shorter and more narrowband pulses compared to signal pulses which are generated from transform-limited pump pulses,

but also in a decrease in conversion efficiency as a large part of the pump pulses is not taking part in the conversion process. The decrease in signal bandwidth and the slight increase of signal peak power are both beneficial for CRS imaging.

5.4 Influence of the Pulse Shape on the Conversion Efficiency and Bandwidth

The previous section has illustrated the strong influence of the pump pulses on the FOPO based conversion. A possibility to circumvent the effect of SPM without sacrificing the entitlement of an all-fiber setup, is the alteration of the pump pulse shape. Up to now, Gaussian shaped pulses were used to pump the FOPO cavity, which broaden as they propagate through a nonlinear medium. While this is true for any pulse shape, the effect on the generated bandwidth can be quite different depending on the shape. Equation 4.17 states that the change in intensity with time causes the generation of a non-linear phase. For a Gaussian-shaped pulse, the intensity changes over the course of the whole pulse. In contrast, for a rectangular pulse the intensity changes only at the edges of the pulse. Thus, at the pulse edges the accumulated phase is much larger than at any section of a comparable Gaussian shaped pulse. The plateau part of the rectangular pulse, on the other hand, is ideally unaffected by SPM. Therefore, the majority of the pump pulse reaches the conversion fiber of the FOPO unbroadened. Figure 5.11(a) shows the spectral difference between a transform-limited pulse with a rectangular temporal shape and one with a Gaussian temporal shape with a FWHM of 40 ps after accumulating 15 *rad* of non-linear phase.

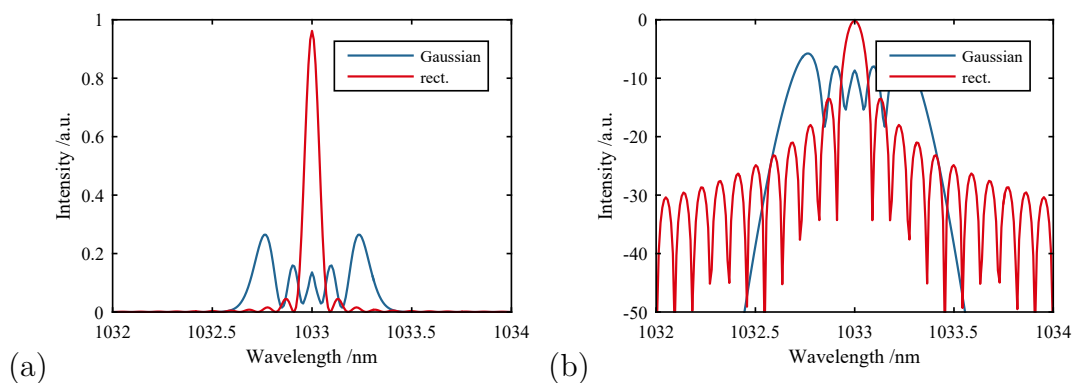


Figure 5.11: Influence of SPM on rectangular and Gaussian temporal pulse shapes in (a) linear scale and (b) logarithmic scale

The initial bandwidth of the rectangular pulse is 80 pm, which is virtually

5. All-Fiber Widely Tunable Optical Parametric Oscillator

Parameter	Value
ESM fiber length l_{con}	12 cm
pump pulse energy E	400 nJ
pump pulse duration (FWHM) τ	65 ps
pump wavelength λ_{pump}	1034.2 nm
feedback fiber length l_{delay}	275 m
Feedback ratio α	-30 dB

Table 5.2: Parameters for the rectangular pulse shape FOPO

unaffected by SPM. The spectral width of the Gaussian pulse, on the other hand, is increased from 40 pm to 600 pm. A logarithmic plot of the spectrum (5.11(b)) reveals the broad pedestal of the rectangular pulse which does not contribute to the conversion process.

It has also been shown that the SPM-broadened pump pulses cause pump depletion only within a limited part of the pulse. In fact, even a transform-limited Gaussian shaped pulse is only partially depleted in the FOPO as only the central part of the pulse is strong enough to cause efficient conversion. In this regard, rectangular shaped pulses have a two-fold advantage: because nearly the whole pulse can be converted by a FOPO and the pump pulses reach conversion fiber nearly undistorted.

A model of a FOPO pumped with a rectangular temporal pulse shape and a short conversion fiber length was simulated to show the increase in efficiency and decrease in bandwidth. The pulse parameters have been chosen in order to reflect the parameters used in the experiment described in [78], which will be further discussed in chapter 6. The parameters are listed in table 5.2.

The initial 40 oscillations are simulated and plotted in figure 5.12.

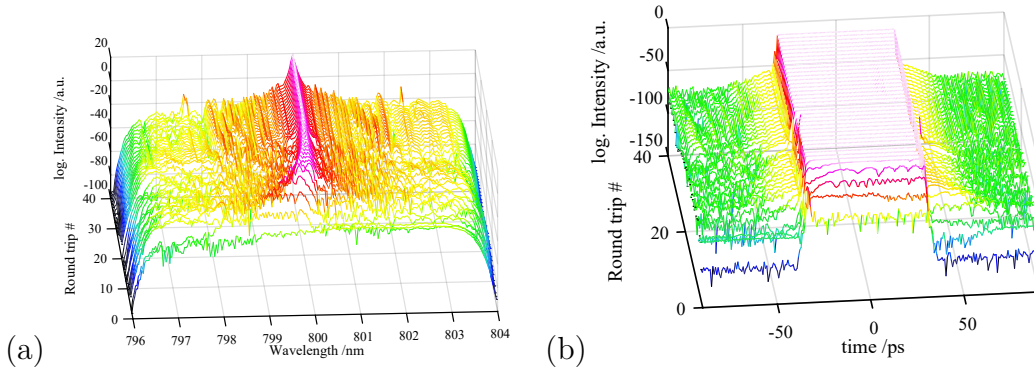


Figure 5.12: Pulse evolution to the steady state in a FOPO pump with rectangular pump pulses. (a) Depiction of the spectrum and (b) the temporal shape of the signal pulse in logarithmic scale.

5. All-Fiber Widely Tunable Optical Parametric Oscillator

The signal pulse duration settles at 63.4 ps which is nearly identical to the pump pulse duration. The bandwidth of the signal is 43.6 pm and virtually transform-limited for a rectangular pulse of this duration. The total conversion efficiency of the pump pulses to the signal and idler pulse is 90.3%, which results in a signal conversion efficiency of 63.4%. In the actual experiment [78], the conversion efficiencies were significantly lower due to the only nearly rectangular temporal pulse shape after amplification. The extremely narrowband signal pulses can be understood as a feature of the rectangular pulses. In a Gaussian FOPO, the feedback fiber and the conversion fiber can cause significant amounts of non-linear phase to the oscillating pulse. The signal pulse is, therefore, broadened and becomes temporally stretched. Thus, the signal pulse portion which seeds the next pump pulse becomes smaller. In the rectangular FOPO, the temporal signal pulse is generated with a rectangular temporal shape which, if the temporal phase of the pulse aligns to form a narrowband signal spectrum, is only minimally stretched by dispersion in the feedback fiber. The temporal overlap with the next pump pulse is then maximized and preferred by the system. Narrowband signal pulses are, therefore, preferred by the rectangular FOPO. The pulse shape of the signal before and after the feedback fiber in the steady-state is depicted in figure 5.13(a).

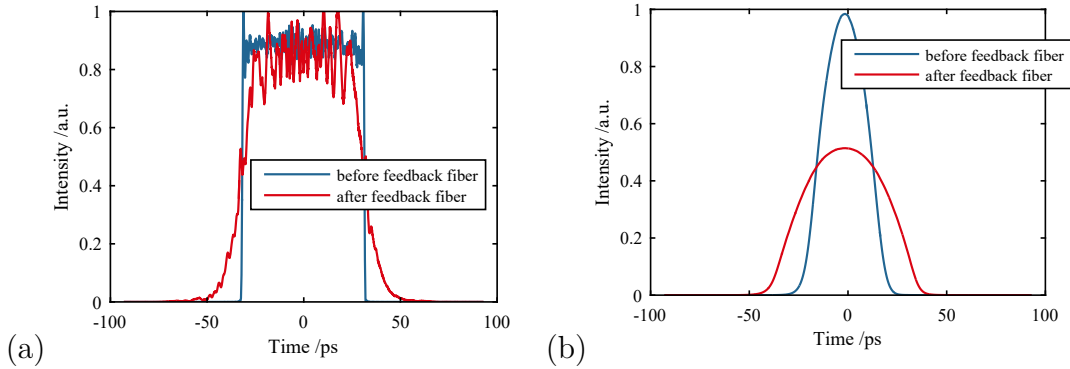


Figure 5.13: (a) Simulation of the temporal shape of the rectangular FOPO signal and (b) the Gaussian FOPO signal before and after the feedback fiber.

The rectangular signal is nearly unaffected by the feedback fiber as its bandwidth is only 45 pm. After the feedback fiber the spectrum is nearly unchanged with a bandwidth of 48 pm. The fine modulations on the rectangular temporal pulse shape are associated to the rectangular pulse shape itself. The downside of this method is the complicated pulse generation. The method which was used in ref. [78] involved the generation of a broadband signal from which a narrowband portion was extracted by a unapodized fiber-Bragg grating (FBG) (Chapter 6.1). The

5. All-Fiber Widely Tunable Optical Parametric Oscillator

resulting pulse shows a nearly rectangular pulse shape. As the FBG is fixed to a certain wavelength, tuning it by the amount needed for a widely tuneable source (e.g. by stretching the FBG) is not possible. For comparison, the signal evolution of a Gaussian signal through the feedback fiber from the FOPO of section 5.1.3 is depicted in figure 5.13(b). As can be seen, the feedback pulse is dispersed from a pulse duration of 27 ps to 63 ps and broadens from 1.0 nm to 1.4 nm.

6 Implemented Laser Sources for Multi-Photon and Coherent Raman Scattering Imaging

In the previous chapter light conversion in a four-wave-mixing-based optical parametric oscillator (FOPO) has been discussed and analyzed. At the beginning of this thesis, the FOPO was built having exclusively CARS imaging in mind. The application to multi-photon imaging and SRS of this laser concept was done only after realizing its potential. Therefore, the organization of this last chapter will follow the historical steps: first, the FOPO for CARS imaging will be presented, which features rectangular shaped pump pulses, short conversion fiber lengths and a high conversion efficiency at a repetition rate of ≈ 1 MHz. This setup contained many free-space sections which allowed for a detailed characterization of this laser concept. Subsequent simulations of this source revealed the linear chirp of the signal and idler pulses. Thus, after the optimization of the bandwidth of the idler pulses and subsequent compression to femtosecond pulse durations, three-photon excited fluorescence imaging could be carried out with the source described in section 6.2. The development continued by implementing the tuneable Ytterbium-doped oscillator and increasing the repetition rate to ≈ 10 MHz in order to support widely tuneable and fast SRS imaging in conjunction with a secondary low noise laser output (section 6.3). This marked the final step in developing an all-fiber OPO for applications outside a laboratory environment.

6.1 Fiber OPO for CARS Imaging

According to the optimal parameters for CARS imaging given in section 3.2, the goal of this development was to support CARS imaging at pixel-dwell times in the microsecond range for fast single-frame imaging with high chemical resolution. The setup is depicted in figure 6.1.

6. Implemented Laser Sources for Multi-Photon and Coherent Raman Scattering Imaging

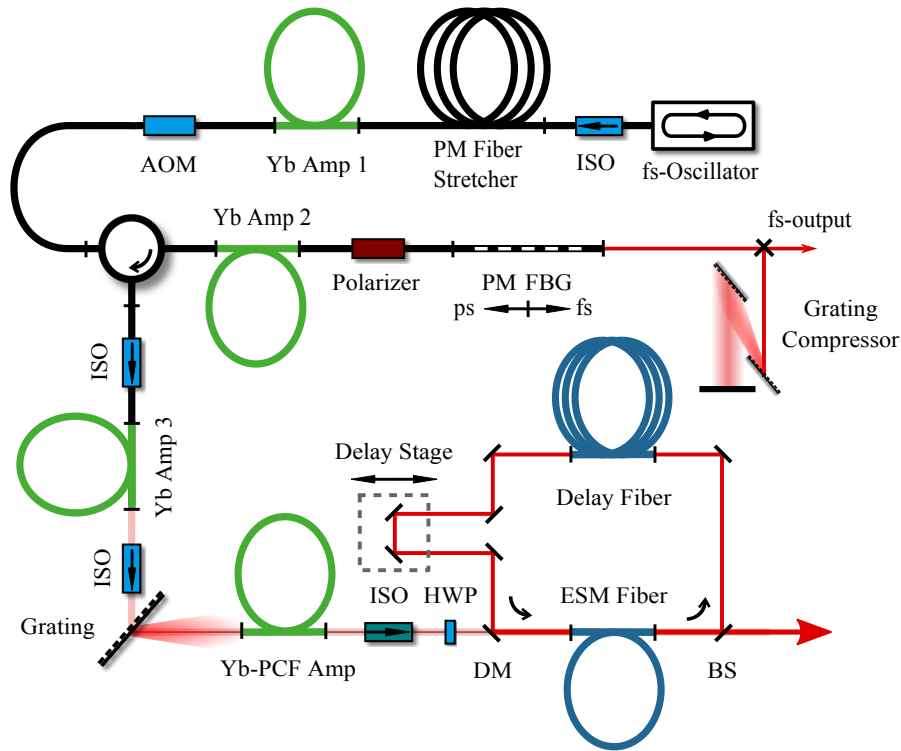


Figure 6.1: Setup for the free-space FOPO. ISO: Optical isolator, PM fiber Stretcher: 20 m of polarization-maintaining single-mode fiber, Yb Amp: single-clad Ytterbium doped amplifiers, PM FBG: polarization-maintaining fiber-Bragg grating, Yb-PCF Amp: Ytterbium-doped double-clad photonic crystal fiber 170 μm pump core and 40 μm signal-core, DM: dichroic mirror, BS: beam splitter, ESM fiber: endlessly single-mode fiber.

The front-end was based on a broadband mode-locked femtosecond oscillator emitting chirped pulses with a duration of 7 ps and a bandwidth of 11 nm. The bandwidth of the oscillator supported a compressed pulse duration of 200 fs. The uncompressed pulse was stretched in time with 20 m of polarization-maintaining (PM) fiber to a pulse duration of 24 ps in order to mitigate SPM later in the amplifier chain. An acousto-optical modulator (AOM) reduced the pulse-repetition rate of the pre-amplified oscillator pulses from 25 MHz to 780 kHz. Then, a circulator was used to insert a fiber-Bragg grating, which was used to filter out a narrowband portion of the broad oscillator spectrum reflecting it back to the circulator. A double pass amplifier was used to compensate for the losses of the components and the filter. The remaining part of the broad spectrum was coupled out and compressed to 240 fs. The compressed pulses were used to conduct a cross-correlation of the filtered pulses. By overlapping both pulses in a birefringent nonlinear β -barium borate crystal to generate the sum frequency and by shifting the relative delay of the pulses, the temporal shape of the filtered pulses could be measured. Due to the

6. Implemented Laser Sources for Multi-Photon and Coherent Raman Scattering Imaging

short probe pulses, a high temporal resolution of 240 fs could be reached. Figure 6.2(a) depicts the results of the measured pulse shape.

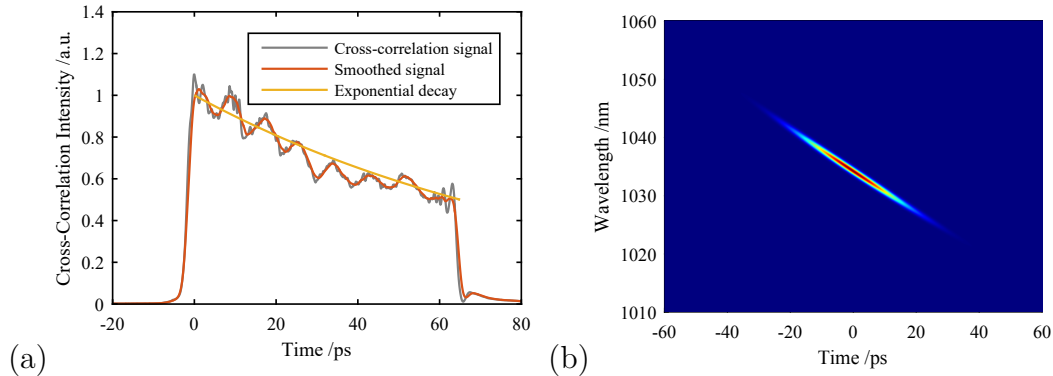


Figure 6.2: (a) Cross-correlation trace of the rectangular-shaped pulse. (b) Spectrogram of a simulated pulse with 11nm bandwidth and a chirped pulse duration of 24 ps.

The pulse shape features very steep edges and a long plateau, which are the key features of a rectangular pulse. The generation of such a pulse shape takes place in the FBG used for filtering the chirped incoming pulse. In a highly chirped femtosecond pulse each frequency component is located at a certain time slice. To illustrate this, the spectrogram of a femtosecond pulse with a spectral bandwidth of 11 nm, which has been chirped to a pulse length of 24 ps, is displayed in figure 6.2(b). It is obvious, that within the chirped pulse, only a short part of the pulse is present at each wavelength. To find out how long this pulse section is, a gaussian spectral filter with different FWHM was applied to the pulse. At a filter bandwidth of 1.2 nm the pulse duration reaches a minimum at 1.7 ps. The interaction with the FBG narrowband is, therefore, locally confined to only this pulse duration. Thus, the temporal characteristic of the reflected pulse was a convolution of the longitudinal reflectivity of the FBG and the duration of a single wavelength slice of the chirped pulse. The grating had a length of ≈ 7 mm, which means that the resulting pulse duration of the reflected pulse had a duration of $\tau = 2nl/c = 70$ ps, fitting the measurement very well. The decay of the temporal intensity with time is due to the reflectivity of the FBG. The orange curve in figure 6.2(a) shows the simulated exponential decay of a linear reflecting medium ($I_R = I_0 e^{-\alpha t}$, $\alpha = 0.00785 \frac{1}{\text{ps}}$), where 50% of the incoming intensity is reflected after 70 ps. The overall reflectivity value fits very well the measured reflectivity provided by the manufacturer (IPhT Jena). The steepness of the pulse edges correlates to the instantaneous pulse duration of the chirped pulse at the center wavelength of

6. Implemented Laser Sources for Multi-Photon and Coherent Raman Scattering Imaging

the FBG. This kind of pulse shaping method is a very versatile way to shape pulses on a picosecond scale. In fact, this is a much faster pulse shaping method compared to active pulse shapers such as EOMs and with a much higher temporal resolution than Fourier-based filters (for narrow ps pulses). The pulse shape can be controlled by the strength of the grating over its elongation, thus, such a method can enable precise pulse shaping in an all-fiber fashion. The characterization method of the pulses is part of a publication presented in [13]. The rectangular pulse shape allows for highly efficient conversion via FWM as it was described in section 5.4.

The generated seed pulses at 1032 nm were amplified in Yb-Amp 3 and filtered by a single diffraction grating to eliminate the amplified spontaneous emission of the previous amplifier stages. The diffracted light is afterwards coupled into a double-clad PCF with a mode-field diameter of 33 μm and a pump core diameter of 170 μm . At the output of the amplifier, output powers in the order of a few Watts could be obtained with a pulse repetition rate of 750 kHz. The pump pulses were coupled to the cavity through a dichroic mirror and into a ESM fiber with a length of 12 cm (one-hole-missing design, $\Lambda = 3.25 \mu\text{m}$, relative hole size of 0.5). The conversion process has been simulated in chapter 5.4 which explains the narrow-band conversion supported by the rectangular pulses. Figure 6.3 shows the close match between the simulation and the experiment.

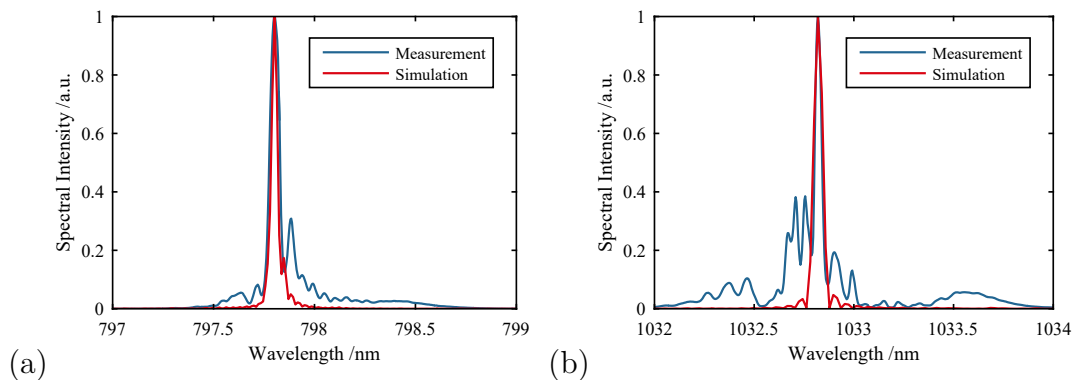


Figure 6.3: Comparison of the measured and simulated (a) signal and (b) pump pulses after conversion in the rectangular pump-pulse driven FOPO cavity.

The narrow-band main feature of the signal pulse and the residual pump pulse were very well reproduced by the simulation model. This model could also explain the spectral ripples originating from the temporal rectangular pulse shape, which transforms to a sinc^2 intensity shape in frequency space. The residual features in the experiment can be attributed to the imperfect rectangular pulse shape of the pump pulses (see figure 6.2). The signal and residual pump bandwidth

6. Implemented Laser Sources for Multi-Photon and Coherent Raman Scattering Imaging

were measured to be below 60 pm which translates to an extremely high chemical (spectral) resolution better than 1 cm^{-1} .

The signal wavelength was tuned by moving a translation stage in the FOPO cavity. In section 5.1.3 the tuning mechanism was already explained and simulated. By changing the cavity length, the signal wavelength which is resonant to the new cavity length, shifts. If the FWM process provides enough gain to compensate the losses in the cavity at this new wavelength, the new signal wavelength keeps oscillating. The resulting signal and pump pulse average powers are depicted in figure 6.4.

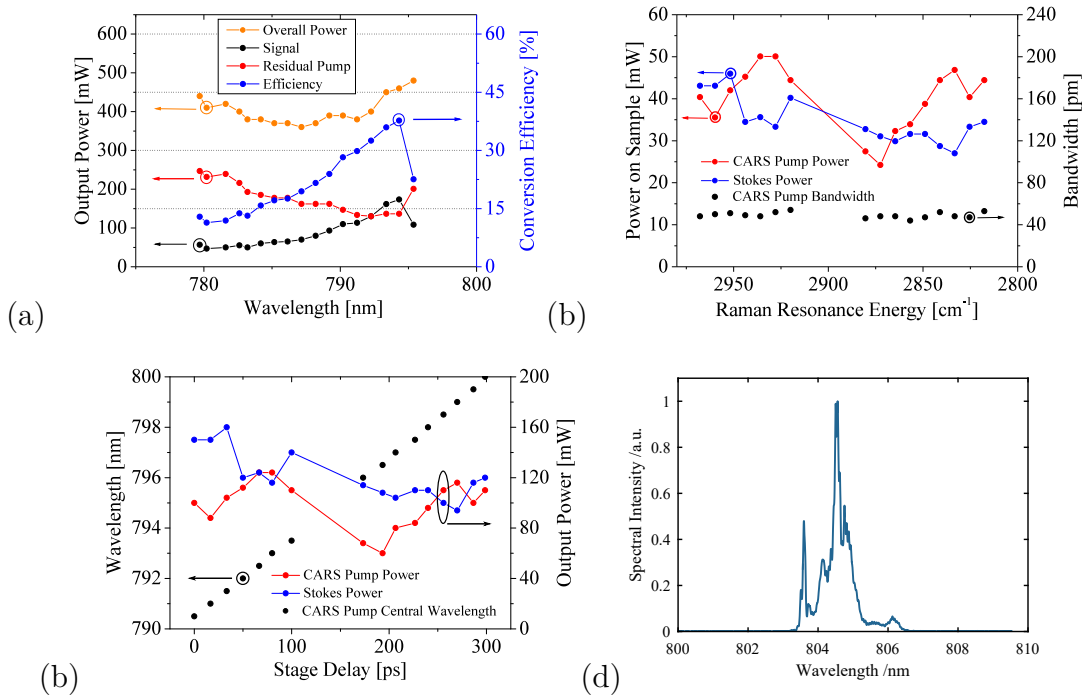


Figure 6.4: (a) Output average power of the signal (black) and residual pump (red) and the overall average power (orange). The conversion efficiency between the pump and signal pulses is plotted in blue. (b) CARS pump (red) and Stokes power (blue) at the sample of the final experiment and the CARS pump bandwidth (black). (c) Tuning behavior of the FOPO in respect to the delay stage position and the corresponding average powers of the CARS pump (red) and Stokes (blue) directly at the FOPO output. (d) Signal output at 80% total conversion efficiency.

Compared to the signal tuning curve in section 5.1.3(a), the resulting pulse energy behavior over signal wavelength closely followed that predicted by the simulation. The wavelength with the highest conversion efficiency was shifted strongly towards the pump wavelength at high conversion efficiencies. There, the residual pump pulses reached their minimum and, if the pulse duration is taken into account,

the optimal peak power ratio of 2:1 between signal (CARS pump) and the pump (Stokes) pulses has been achieved [?]. The conversion efficiency could be increased to 50 %, which corresponds to a total conversion efficiency of over 80 % when the pump pulse energy was increased further. In this state the signal pulses were broad and structured (see figure 6.4(d)). In order to avoid this, the FOPO was driven a moderate pump powers and conversion efficiencies.

The available signal and pump pulse average power superseded the requirements for CARS microscopy. Therefore, for the sake of long-term stability, the conversion fiber length was increased to 20 cm to allow the FOPO working at lower pump powers. As a result, the tuning bandwidth was also decreased due to the decreased pump peak power. In this early experiment, a wavelength tuneable pump source was not available, thus, in order to regain some of the tuning bandwidth, the second polarization axis in the polarization maintaining conversion fiber was exploited for conversion. Usually, only the so-called slow axis of this fiber is used for conversion. However, if the input polarization was rotated by 90° , the light was coupled to the so-called fast axis of the fiber, which exhibited a slightly different dispersion. In this particular fiber, this led to a shift of the gain peak of about 5 nm. Figure 6.4(b) displays the resulting signal tuning curves of the two polarization states in the conversion fiber. Depending on the input polarization and the position of the delay stage (figure 6.4(b)), the signal radiation (the CARS pump) could be tuned between 790 and 793 nm and between 796 and 800 nm (figure 6.4(c)). The FWHM bandwidth stayed below 50 pm over the whole tuning range, which enabled high resolution CARS microscopy.

Together with a laser scanning microscope, which was provided by the non-linear imaging group of the IPhT in Jena, the laser source was used for CARS microscopy. Since the CARS pump and Stokes (the residual pump) waves emerge from the same fiber, both pulses were passively synchronized and overlapped in space (due to the common fiber) and time (due to the FWM process and the low relative walk-off in the fiber). Therefore, the fiber output of the source could be directly coupled to the laser scanning microscope (see figure 6.5).

6. Implemented Laser Sources for Multi-Photon and Coherent Raman Scattering Imaging

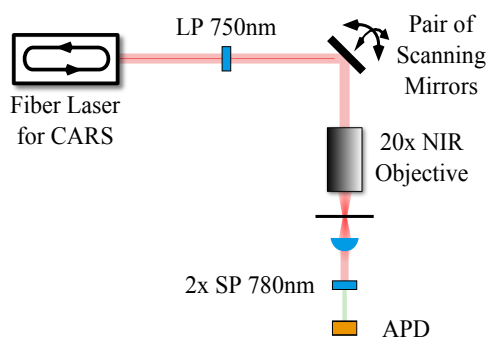


Figure 6.5: Setup of the imaging system. LP: long pass filter, SP: short pass filter, APD: avalanche photo diode.

A long-pass filter at 750 nm was placed into the laser beam in order to filter any unwanted radiation emerging from the FOPO. To focus the beams, a 20x magnifying objective optimized for NIR was used. After the condenser lens, two short-pass filters at 780 nm were used to block the residual pump and Stokes radiation. Moreover, to avoid the signal originating from two-photon excited fluorescence (TPEF) or second harmonic generation (SHG) of the Stokes radiation, a long-pass filter with an edge wavelength of 530 nm was placed in the setup. Thus, the anti-Stokes radiation around 645 nm without averaging with a pixel dwell time of 2 μ s was detected, which resulted in an acquisition time of 32 seconds for a picture with a resolution of 4096x4098 pixels. Figure 6.6 depicts a high spectral resolution CARS image at 2850 cm^{-1} (CH₂, orange) and 2930 cm^{-1} (CH₃, green) of a human perivascular tissue sample. Lipid filled adipocytes were contrasted in orange against the greenish protein fibers of the connective tissue demonstrating discrimination of lipids and proteins by CARS imaging at two wave-number positions. Furthermore, by slightly changing the resonator cavity length with the translation stage, the CARS pump wavelengths can be tuned across these resonances to maximize the contrast between the two CARS signals.

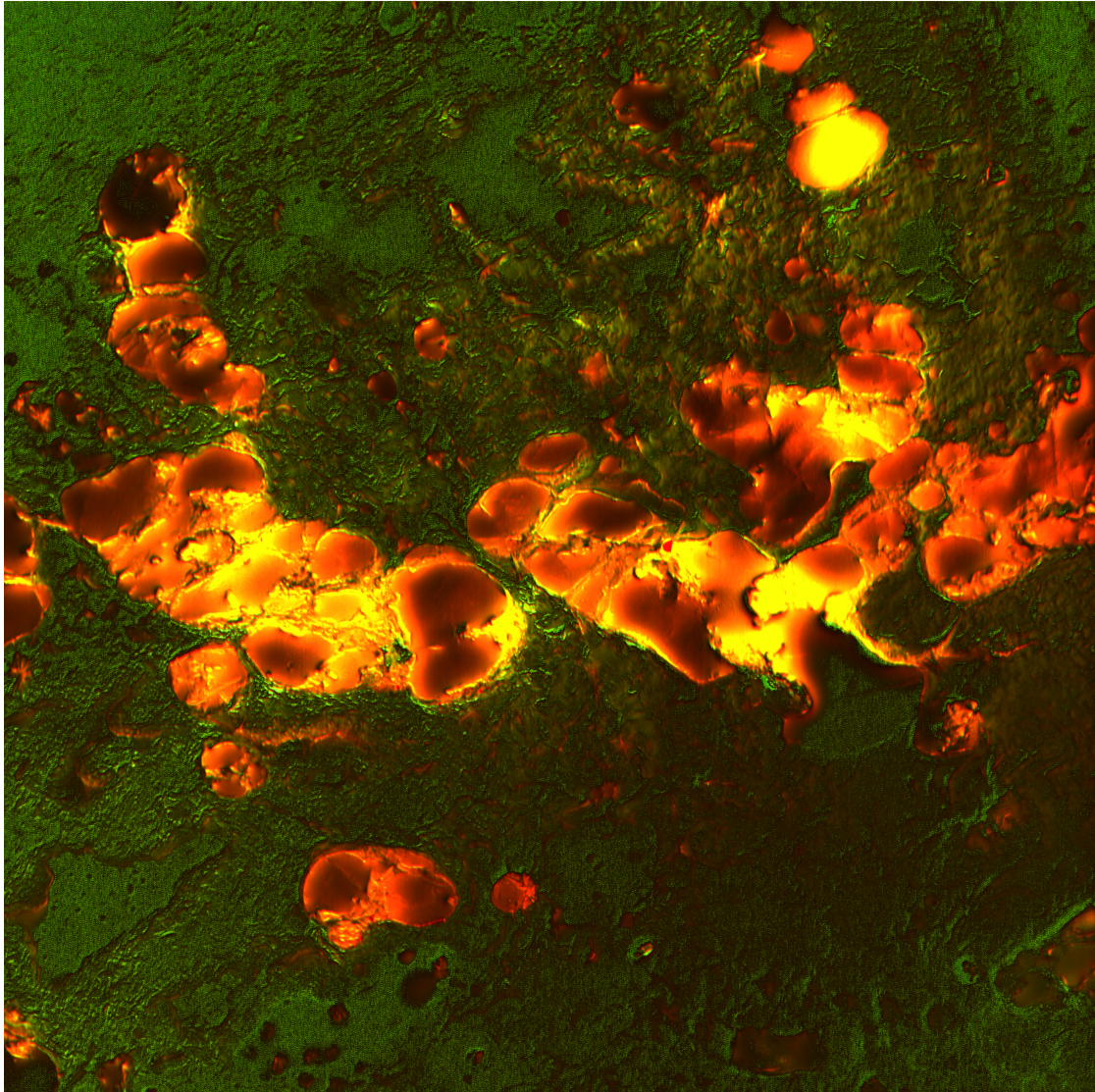


Figure 6.6: Superposed and color-coded CARS signals probing CH_2 at 2850 cm^{-1} (orange) and CH_3 at 2930 cm^{-1} (green). The picture size is $1\times 1\text{ mm}^2$ [78].

The fiber-based optical-parametric oscillator delivered an unprecedented high signal strength and chemical selectivity due to its narrow-band CARS pump and Stokes radiation. According to the parameters discussed in section 3.2, the source delivers the ideal parameters for single frame CARS microscopy and also sparked the interest to use this concept for other non-linear imaging applications. This source including the imaging experiment has been published in optics express [78]. This source was also compared, in an exhaustive comparison, to other fiber based CARS sources in a review paper [?]. It could be concluded that the highly dispersive FWM based FOPO offered the highest spectral (chemical) resolution at an exceptionally high peak power enabling a superior imaging quality and chemically selectivity

6. Implemented Laser Sources for Multi-Photon and Coherent Raman Scattering Imaging

in the CH-region ($\sim 2930 \text{ cm}^{-1}$). The final comparison chart from this review is depicted in figure 6.7.

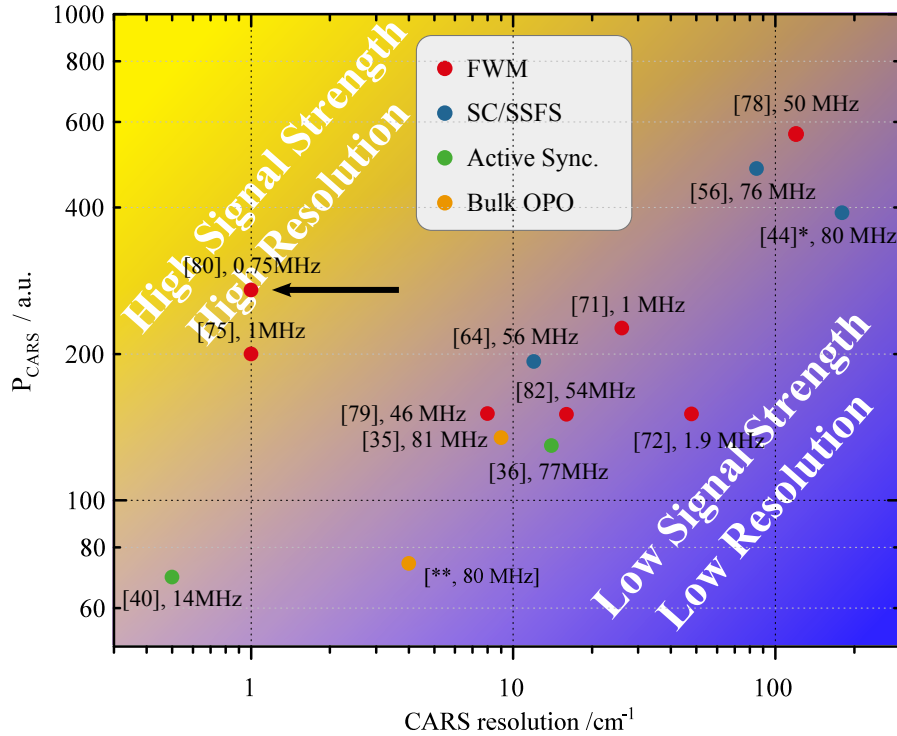


Figure 6.7: Comparison of fiber laser sources for narrow band CARS microscopy [?]. The presented light source is marked with a black arrow.

6.2 Fiber OPO for Three-Photon Excited Fluorescence (3PEF) Imaging

In a second experiment the possibility to compress the converted signal and idler waves to sub-picosecond pulse durations was explored. As a prove of concept, the converted signal pulses were compressed via dielectric gratings to a duration of 3 ps. In order to reach useful parameters for multi-photon imaging, the goal was to decrease the pulse duration as far as possible. Simulations revealed that the effective bandwidth of the dispersive filter in the cavity and the gain bandwidth are the main limiting factors for achieving broad signal bandwidths, which ultimately determine the minimum compressed pulse duration of the pulse. The optimal laser parameters for three-photon excited fluorescence were identified in section 3.4. Even though the demanded peak-power is much higher than for CARS microscopy, it does not require narrow excitation. Therefore, short pulses with high energy are needed. To avoid photo-induced damage, the average power had to be limited,

6. Implemented Laser Sources for Multi-Photon and Coherent Raman Scattering Imaging

which means that the repetition rate of the driving laser had to be as low as possible [6]. On the other hand, a minimum repetition rate has to be employed, in order to ensure rapid image acquisition (the pulse repetition rate limits the pixel acquisition rate). Therefore, a repetition rate of roughly 1 MHz was used again. Thus cavity length of the FOPO had to be at least 200 m in order to be resonant to the pump repetition rate. However, the cavity dispersion had to be minimized to achieve broader spectral bandwidths and shorter compressed pulses. Consequently, the spectral region around 1250 nm was chosen for the idler, since in this region the absorption in biological tissue reaches a local minimum and a standard PM fibers exhibit a low positive 2nd-order dispersion. Therefore, the cavity was tuned to be resonant to the idler pulses so that these pulses become positively chirped and compressible in a compact dielectric grating pulse compressor. The realized setup is depicted in figure 6.8.

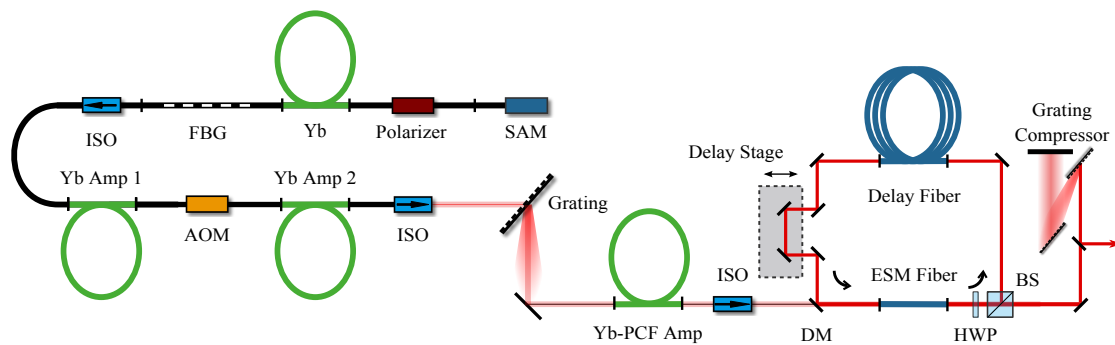


Figure 6.8: Setup of the short pulse FOPO. SAM: saturable absorber mirror, Yb: Ytterbium-doped single-clad fiber, FBG: fiber Bragg-grating, ISO: Isolator, Yb Amp 1&2: Ytterbium-doped single-clad fiber-amplifier, AOM: acousto-optical modulator, Yb-PCF Amp: Ytterbium-doped double-clad photonic crystal fiber amplifier, DM: dichroic mirror, ESM fiber: effectively single-mode fiber, HWP: half-wave plate, BS: beam splitter.

The pulse generation was done in a different way than in the last experiment in order to generate Gaussian shaped pump pulses for the FOPO cavity. Here, the pulses were directly generated in a narrow-band Yb-doped fiber laser cavity, which incorporates a SAM and a FBG (as shown in figure 6.8). The polarizer ensured stable mode-locking in only one polarization axis. The pulse duration is defined by the bandwidth of the FBG, which is acting as one of the end-mirrors of the laser cavity and ensures a narrow-band operation in the steady state by reflecting only a bandwidth of 40 pm at 1040 nm. The FBG also serves as an output-coupler featuring a transmission of 60%. The resulting pulse duration was measured via auto-correlation to be 60 ps. The radiation was pre-amplified in

6. Implemented Laser Sources for Multi-Photon and Coherent Raman Scattering Imaging

single-clad amplifiers, picked to a repetition-rate of 780 kHz and amplified in a double-clad PCF with a MFD of 33 μm . The source delivered up to 2.5 μJ of pump pulse energy. Since the target idler wavelength was 1250 nm, the pump pulses were coupled to an ESM fiber with slightly smaller dimensions than the one used in the first FOPO (one hole missing core design, hole diameter 1.55 μm , hole to hole distance 3.1 μm). This resulted in a lower frequency shift in the FWM process without the need for longer pump wavelengths, which would be far off the gain peak of the Ytterbium ion. Without the feedback of the FOPO cavity, the radiation produced from amplified quantum noise indicates the gain bandwidth of the FWM process. The resulting OPG signal was recorded for pulse energies ranging from 1.15 to 1.66 μJ and plotted in figure 6.9(a).

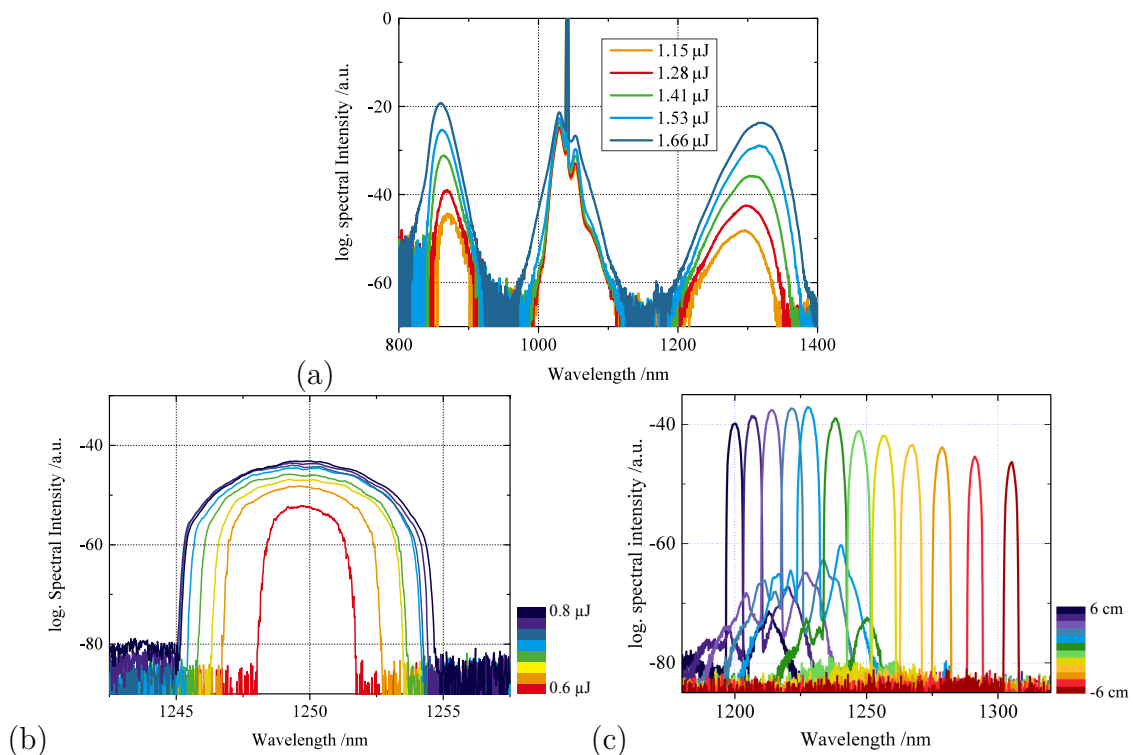


Figure 6.9: (a) OPG signal at different pump pulse energies. (b) Bandwidth dependence of the idler pulses with respect to the pump pulse energy with the FOPO cavity closed. (c) Idler spectra for different FOPO cavity lengths [77].

The central wavelength of the OPG signal shifted with increasing pump peak power away from the pump wavelength as predicted by equation 4.30 and depicted in figure 4.7. Due to the high peak power (~ 30 kW) of the pump pulses, which central wavelength laid close to the ZDW of the ESM fiber, the bandwidth of the OPG signal and, therefore, the FWM gain bandwidth was very broad.

The FOPO cavity consisted of 11.5 cm of ESM fiber, a half-wave plate and a

6. Implemented Laser Sources for Multi-Photon and Coherent Raman Scattering Imaging

polarization dependent beam-splitter for out-coupling and a 250 m long piece of single-mode fiber to form a cavity, which was resonant to the pump pulse repetition rate. To adjust the cavity length, a linear delay-stage was inserted into the cavity. When the cavity was closed, the oscillator produced broad spectra (see figure 6.9(b)) which were widely tuneable (figure 6.9(c)). The pump pulse energy required to lock the FOPO cavity was strongly decreased compared to the open loop. The FWM gain overcame the cavity losses at 1250 nm when the ESM fiber was pumped with 600 nJ. Increasing the pump energy resulted in a broadening of the idler radiation up to a bandwidth of 6.5 nm (see figure 6.10(b)). Increasing the bandwidth beyond this point generated narrow spectral features while the bandwidth remained constant. This might be due to the temporal shape of the signal pulse to develop a flat top when the conversion saturates. This would enable narrow-band rectangular pulse shapes as it was described in section 5.4.

By changing the cavity length of the FOPO in steps of 1 cm, the idler radiation could be tuned from 1200 to 1300 nm. Due to the decreased gain at the edges of the tuning range, the idler radiation became narrower. The spacing between the recorded spectra increased for longer wavelengths owing to the decrease in 2nd-order dispersion towards the ZDW of the delay fiber. The tuneable bandwidth could be increased by increasing the pump energy and decreasing the conversion fiber length in order to reach the same gain in the cavity (see eq. 4.28) while increasing the gain bandwidth (see eq. 4.29). The conversion efficiency of the pump to the idler pulse energy was 4.7%, which corresponds to an overall efficiency of just 8%. This is only a fraction of the efficiency of the narrowband FOPO. Consequently, the tuning curve is not as lopsided (see equation 5.1).

The subsequent compression of the broad idler pulses was done by using a pair of diffractive gratings with a line density of 1250 lines/mm with a distance of about 250 mm. After a double pass over the grating pair the pulses exhibited an auto-correlation length of 800 fs (see figure 6.10(c)). The simulation of the pulses and comparison with the auto-correlation trace confirmed a pulse duration of 560 fs FWHM. The simulation also revealed a large contribution of 3rd-order dispersion in the residual phase (see figure 6.11(d)). As a side note, the relative contribution of this 3rd dispersion order increases for idler wavelengths near the ZDW of the overall cavity dispersion (which in this case is dominated by the feedback fiber). To enhance the relative contribution of the 3rd order dispersion an experiment that was later carried out with a tuneable seed source (see section 6.3). The pump wavelength was shifted to longer wavelengths in order to generate gain for longer idler wavelengths in the vicinity of the ZDW. Since the 2nd order dispersion vanishes towards this

6. Implemented Laser Sources for Multi-Photon and Coherent Raman Scattering Imaging

wavelength, the spectral position of the idler becomes extremely sensitive to cavity length alterations and temporal fluctuation which alter the refractive index of the fiber. Figure 6.10(a) depicts two sample spectra around the ZDW of the fiber cavity. These pulses are dominated by 3rd-order dispersion which leads to the modulations in the spectrum. The ZDW of the fiber cavity is therefore at about 1411 nm.

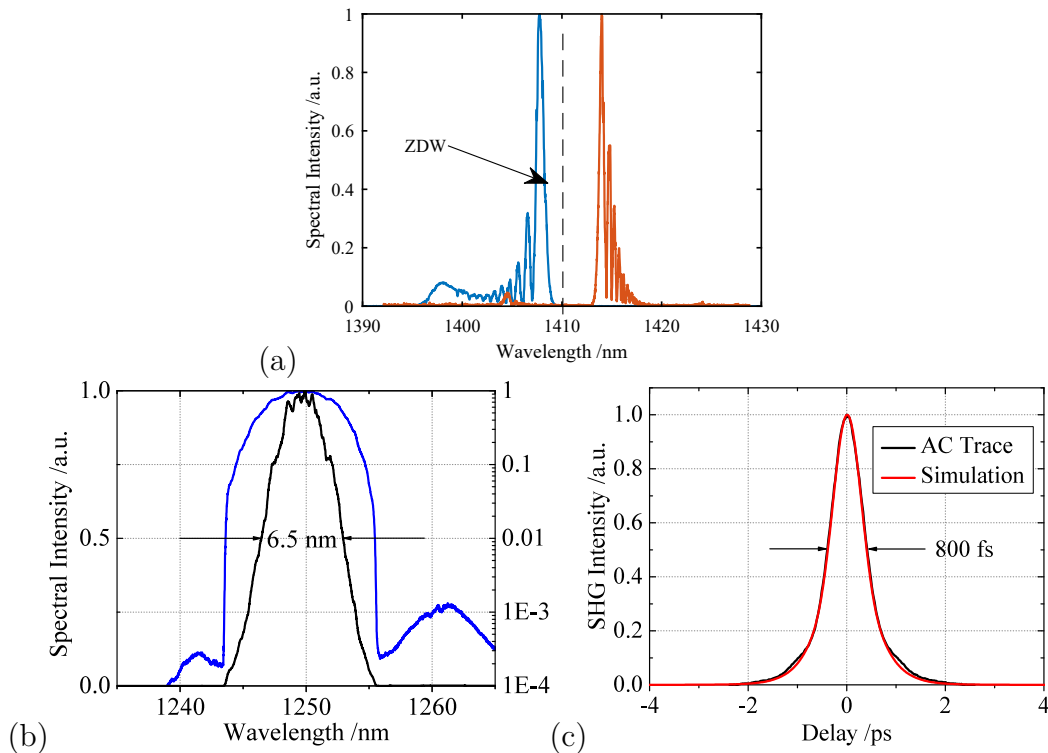


Figure 6.10: (a) Sample spectra around the ZDW of the FOPO cavity. (b) Spectrum of the idler pulses at the output in linear scale (black line) and log. scale (blue line). (c) Measured auto-correlation trace of the idler pulses and the simulated trace in red.

The conversion around 1250 nm is very similar to the ideal FOPO from section 5.1.2. As the FWM gain bandwidth is very broad compared to the situation described in section 5.3, the gain is virtually independent of the chirp of the pump pulses and the spectral bandwidth of the driving pulse has little influence on the FOPO dynamics.

6. Implemented Laser Sources for Multi-Photon and Coherent Raman Scattering Imaging

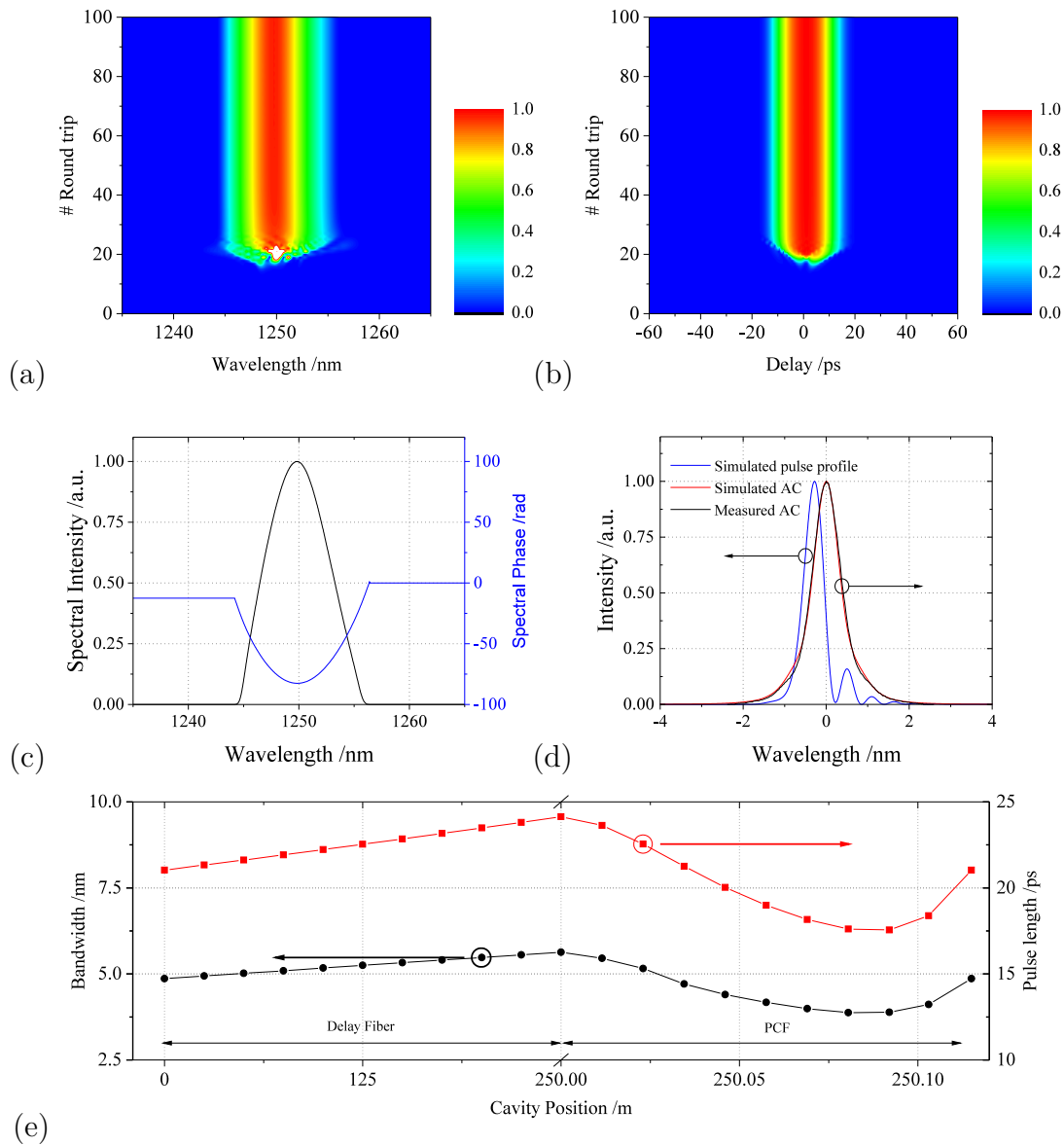


Figure 6.11: Idler pulse evolution (with each round-trip) of (a) the spectrum and (b) its temporal profile. (c) Spectral intensity and phase in the steady state at the output. (d) Simulated temporal pulse profile (blue) with the corresponding simulated (black) and measured (red) AC. (e) Pulse evolution within a single round trip in steady state.

A numerical simulation of the FOPO cavity has been conducted in order to gain insight into the pulse dynamics during the pulse build-up and the steady-state. The cavity was simulated according to the experiment. The energy of the pump pulses was set to 250 nJ and with a duration of 60 ps. The conversion fiber was set according to the experiment to 11.5 cm and the feedback fiber to 250 m with a 6 μm core diameter. Figure 6.11(a) shows the evolution of the output spectra

of the FOPO during the first 100 round trips. The steady state was reached after 30 round-trips. A bandwidth of 6.7 nm FWHM was obtained, which is in good agreement with the experimental results. The temporal evolution of the pulse is displayed in figure 6.11(b). The pulse duration settles at 21 ps FWHM, which corresponds to a reduction to 35% of the initial pump pulse duration of 60 ps. The pump energy required in the experiment could not be reproduced in the simulation (only ~50% of the pulse energy was needed in the simulation compared to the experiment). The additional power requirement in the actual experiment might be due to non-linear polarization rotation of the pump light in the conversion fiber. This would lead to an increase in the demand for pump power and to a lower conversion efficiency. Such polarization effects were not considered in the simulation and are, therefore, only speculative and at this point. Figure 6.11(c) depicts the spectrum of the idler pulses in the steady-state. The spectral phase of the idler pulses has been plotted in the same graph revealing its parabolic shape. By compressing the pulses with grating pairs with the same line density as in the experiment (1250 lines per mm), the measured auto-correlation shape (red line in Fig. 6.11(d)) could be faithfully reproduced (blue line in figure 6.11(d)). This allows estimating the temporal profile of the compressed pulses (see black curve in figure 6(d)). As stated earlier, the residual phase is dominated by 3rd order dispersion mostly originating from the delay fiber. Note that the obtained pulse duration of 560 fs is just ~18% longer than the transform limit of 475 fs. Lastly, figure 6.11(e) depicts the pulse evolution within a single round trip in steady state. In the feedback fiber the fed back pulse was continuously lengthened by dispersion and broadened by SPM. Afterwards the FWM gain led first to a narrowing of the spectrum due to the dispersive filtering effect (see section 5.1.1). As the pulse was linearly chirped, the pulse duration decreased as well. When the gain saturated, the pulse was becoming broader again and the pulse length recovered.

In order to further increase the idler pulse energy, the conversion fiber length was reduced to 6 cm. To reach sufficient gain in the conversion fiber, the pump pulse energy was increased to 2.3 μ J. For stable conversion the feedback ratio was reduced in order to correct for the additional spectral broadening in the feedback fiber by the larger non-linear phase. This also leads to a higher gain and stronger temporal filtering effect of the dispersive delay line during each oscillation. Therefore, the bandwidth reduced to only 4.7 nm. The pulses were compressible to an auto-correlation width of 1.6 ps. A simulation of the cavity suggests a compressed pulse duration of 960 fs. The large auto-correlation width is due to the uncompressed 3rd order dispersion. The conversion efficiency of pump to idler radiation was enhanced

6. Implemented Laser Sources for Multi-Photon and Coherent Raman Scattering Imaging

to 10.9%, which corresponds to an extracted idler average power of 200 mW and a pulse energy of 250 nJ. After pulse compression (40% efficiency), a peak power of 104 kW was obtained. The experimental results are depicted in figures 6.12(a) and 6.12(b).

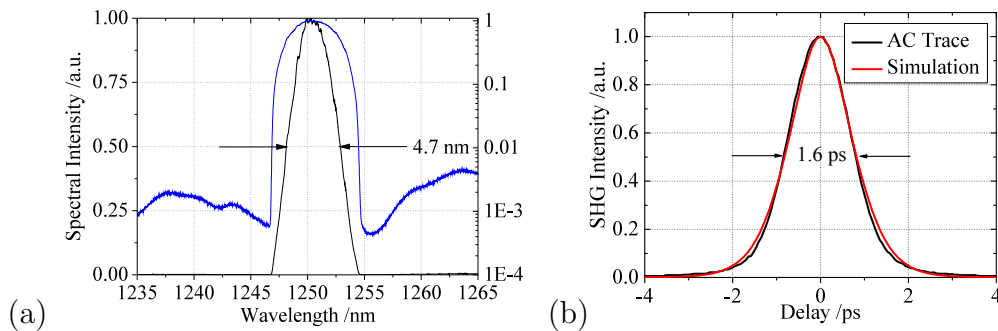


Figure 6.12: Idler spectrum at the output of the cavity in linear (black) and logarithmic scale (blue). (b) Simulated (red) and measured (black) auto-correlation traces.

The experiment was adopted from the experimental conditions presented in a three-photon excited fluorescence imaging experiment conducted in [79]. In this study, 1.5 nJ pulse with a duration of 140 fs at 1280 nm and a repetition rate of 80 MHz were used to scan up to 1.6 mm deep into a mouse cortex. Assuming a two-photon absorption photo-damage mechanism as discussed in section 3.1.3, up to 27 nJ of pulse energy can be used for ~ 1 ps pulses at the same level of photo-damage, since higher pulse peak powers can be used at 0.78 MHz than at 80 MHz pulse repetition rate. In order to acquire the image in figure 6.13, a laser scanning microscope (by the IPhT in Jena) was equipped with a 0.40 NA objective. The signals were collected in forward detection. As a proof-of-principle experiment we used a sample without any fluorescent markers, unlike in [79]. Figure 6.13 depicts a section of a rabbit aorta combining 3PEF (green), third harmonic generation (THG, blue) and second harmonic generation (SHG, red) images. The laser was blocked after the sample using a short pass filter at 750 nm (Semrock). In addition, the 3PEF signal was filtered by a bandpass filter ($\lambda_{center} = 460$ nm, $\Delta\lambda = 80$ nm, Semrock). For recording the THG signal a bandpass filter centered at 415 nm was used ($\lambda_{center} = 415$ nm, $\Delta\lambda = 3$ nm, Semrock). The second harmonic generation signal at 625 nm was isolated with another bandpass filter ($\lambda_{center} = 625$ nm, $\Delta\lambda = 20$ nm, Semrock).

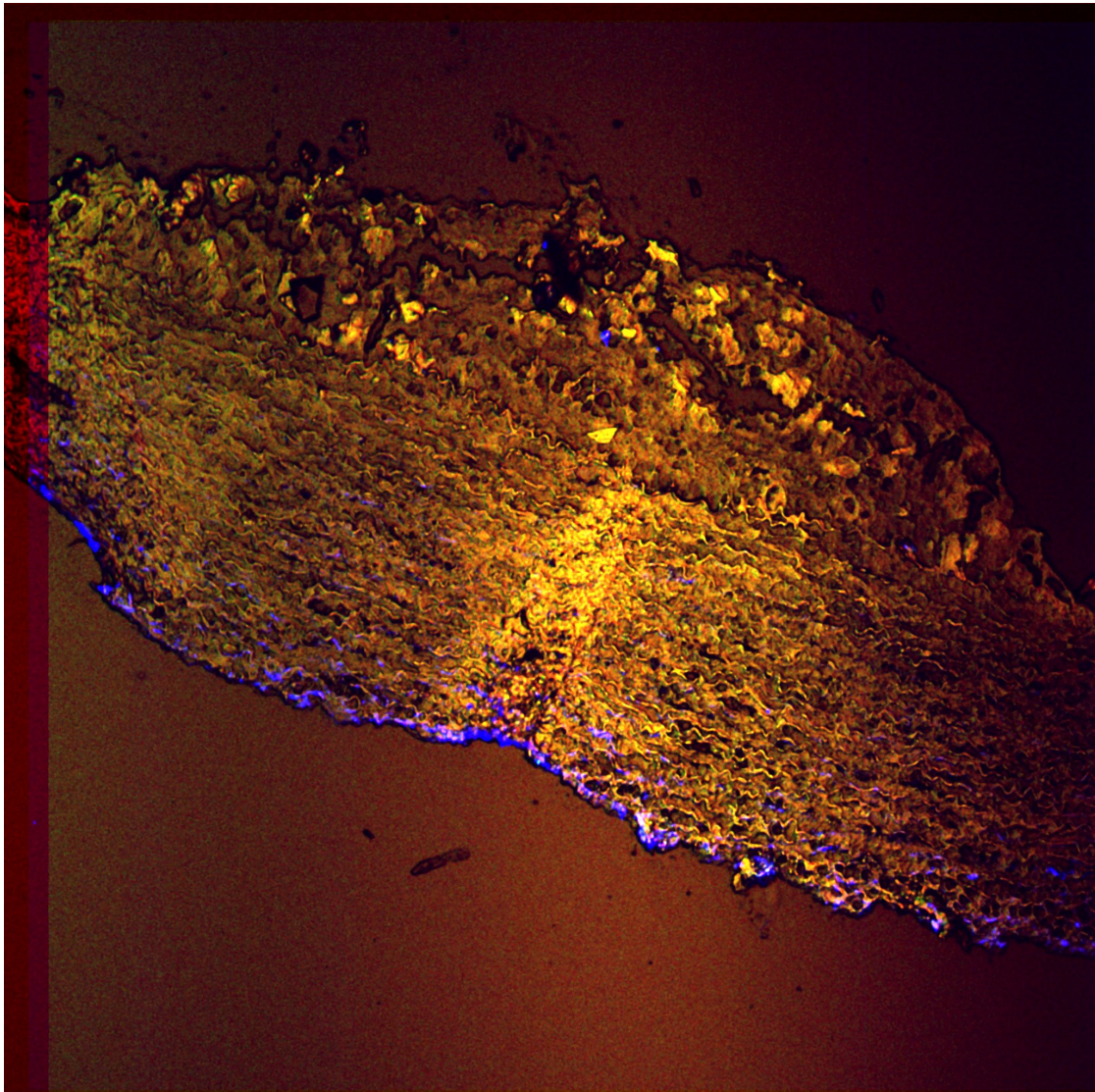


Figure 6.13: Colored and overlaid images combining 3PF (red), third harmonic generation (yellow) and SHG (blue) of an artery cross section from a rabbit model for atherosclerosis.

Even without using a fluorescent label, the (much weaker) auto-fluorescence process could be clearly detected. As discussed above, this fiber-laser source can potentially provide even higher signal powers than the bulk-laser system used in [79], if the sample is similarly labeled using high intensity fluorescent markers. Therefore, it is believed that this laser source could allow imaging tissue layers buried up to 1 mm deep below the surface as demonstrated in [79] when utilizing an appropriate sample preparation and imaging setup. This source including the imaging experiment has been published in optics express [77].

6.3 Fiber OPO for SRS Imaging

The final iteration of the FOPO concept in the scope of this thesis combines the development of an all-fiber widely-tuneable version of the initial FOPO design with the goal to generate the pulse parameters needed for SRS imaging. The pulse parameters for fast-SRS imaging are very similar to the parameters for CARS imaging except for the repetition rate and laser stability. A suitable laser system also needs a secondary laser output which radiates at one of the two wavelengths required for addressing the Raman shift. This output needs to be modulated in order to detect the SRG or SRL in the other wavelength after the interaction with the sample via lock-in detection at the modulation frequency.

In section 3.3, it was concluded that the SRS works well at a higher repetition rates. On the one hand, modulating the beam means that the pixel acquisition rate has to be at least a factor of two lower than the pulse repetition rate. On the other hand, SRS does not benefit as strongly from low repetition rates as CARS and 3PEF does (see equation 3.4). In SRS, the modulation frequency of the modulated beam is imprinted, in the presence of a resonant medium, onto the unmodulated second beam. The weak modulation in the photo diode signal of this beam is filtered out e.g. by a lock-in detector. Therefore, the noise at this frequency has to be extremely low in order to detect the SRS signal quickly and, thus, enable fast image detection (see figure 3.6). The design of the SRS FOPO follows the demand for a low noise FOPO with high repetition rate.

As the gain bandwidth of the four-wave mixing process limits the addressable wavelengths, the pump wavelength has to be tunable in order to unlock a wider spectral range. Figure 6.14 shows the phase-matching of a typical endlessly single-mode fiber similar to the one which was used in the conversion process. To reach energy differences in the range of $900 - 3200 \text{ cm}^{-1}$, the pump wavelength of the oscillator has to be tuned in order to gain access to a signal wavelength range which corresponds to this frequency shift (relative to the pump wavelength) needed for SRS imaging.

6.3.1 Widely tuneable all-fiber FOPO for SRS

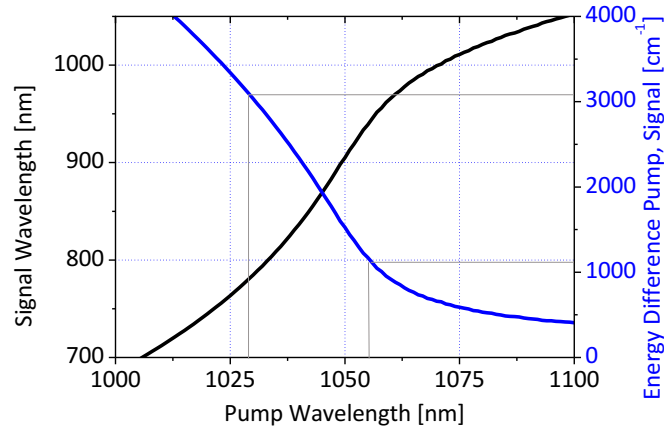


Figure 6.14: Phase-matching diagram for a typical endlessly single mode fiber used for FWM based conversion.

According to figure 6.14, a wavelength tuneable oscillator between 1030 and 1055 nm is needed. On top of that, according to table 3.2, a pulse repetition rate of at least 20 MHz is required to support video rate imaging. An oscillator concept that can provide narrow-band picosecond pulses at such a repetition rate is a passively mode-locked laser similar to the one used in the previous experiment. In such a laser the spectral bandwidth of the emission is inversely proportional to the pulse duration and the bandwidth of such a laser is defined by the bandwidth of a filtering element.

In the case of the generation of narrow-band pulses with durations of tens of picoseconds, the bandwidth of the filtering element is the limiting factor. In order to generate a pulse duration in the range of 40 ps, a filter bandwidth of < 100 pm is required. The simplest, yet most effective way of constructing a tunable narrow filter is to use a diffraction gratings. Such a filter comprises a collimation lens, a grating pair, an 1:1 telescope, a tilt mirror and a focusing lens which couples the filtered radiation back into a fiber. The bandwidth of this kind of filter is defined by the focal length f of the lenses, the grating period Λ of the diffraction gratings, the mode field diameter of the fiber d and the wavelength of the filtered light λ . For a Gaussian beam, the bandwidth can be calculated by [80]:

$$\Delta\lambda_{FWHM} = \sqrt{\ln 2} \cdot \frac{2d\Lambda}{f} \sqrt{1 - [\lambda/2\Lambda]^2} \quad (6.1)$$

The filter bandwidth for a fiber with $d = 6.6 \mu\text{m}$, with collimation and focusing

6. Implemented Laser Sources for Multi-Photon and Coherent Raman Scattering Imaging

focal lengths of $f = 35$ mm and a grating period of $\Lambda = 625$ nm has been plotted in figure 6.15a. The beam path of such a filter is shown for 1000, 1050 and 1100 nm for the parameters given above and depicted in figure 6.15b through d. The tilt of the mirror has to be adjusted by about $\pm 5^\circ$ as the signal wavelength is changed. A fiber integrated version of this filter was purchased from WL-Photonics and inserted into the laser cavity.

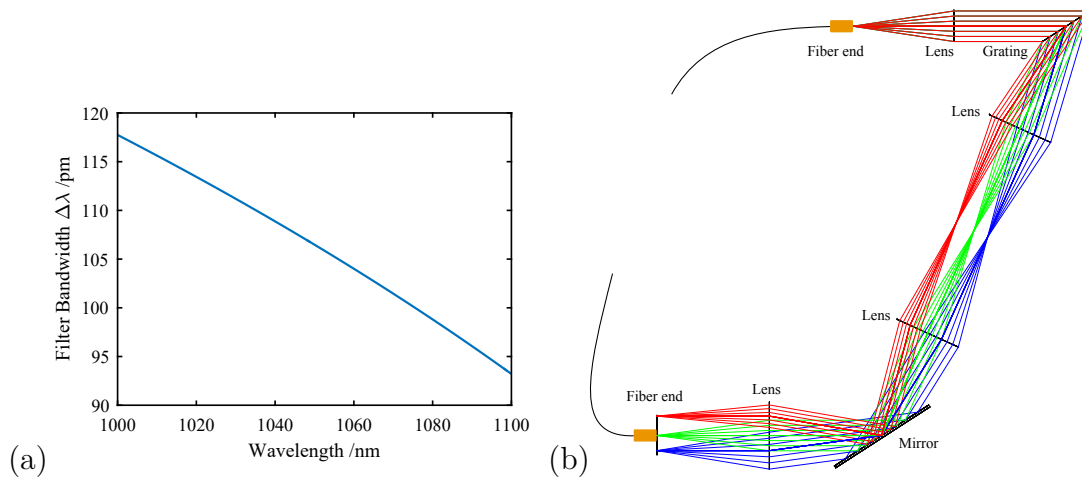


Figure 6.15: (a) Evolution of the spectral bandwidth of a diffraction grating-based narrowband filter with respect to the central wavelength. (b) By adjusting the tilt of the mirror (bold line) the central wavelength of the filter can be set.

The laser cavity was adopted from a positive dispersive mode-locked oscillator [81]. The goal of this cavity was to generate ultra-short laser pulses from a saturable absorber based cavity with a relatively high pulse energy. Figure 6.16 depicts the altered tunable and narrow-band version. The tuneability is achieved by placing the tuneable filter described above inside of the cavity. The saturable absorber mirror (SAM) initiates the mode-locking (see section 4.5) when a certain intensity threshold is reached (which saturates the absorption of the device). The initial light originates from amplified spontaneous emission (ASE) which arises when the Ytterbium-doped fiber is pumped. In order to benefit from the high conversion efficiency of Ytterbium, a diode laser with a pump wavelength of 976 nm was used (see section 4.4), which is coupled into the laser cavity through a wavelength division multiplexer (WDM).

6. Implemented Laser Sources for Multi-Photon and Coherent Raman Scattering Imaging

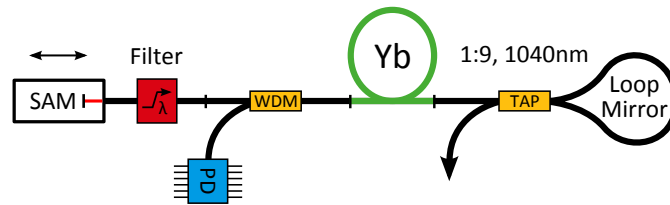


Figure 6.16: Setup of the tunable Ytterbium-doped fiber oscillator. The components of the setup from left to right: SAM: saturable absorber mirror, Filter: the narrow-band tunable filter, WDM: wavelength division multiplexer, PD: single-mode pump diode, Yb: Ytterbium-doped single-clad polarization-maintaining step-index fiber, TAP: tap coupler with two in and output ports and a coupling ratio of 1:9.

The tap-coupler in the setup acts as a semi-transparent out-coupling mirror and is based on a Sagnac interferometer. This so-called linear-loop mirror splits the incoming laser field in two beams that propagate in opposite directions to the opposing ends of the loop. After their propagation through the loop, the two fields interfere with one another. Depending on the split ratio of the tap coupler, the out-coupling ratio can be set between 0 and 1. The dependence of the effective reflectivity of the linear loop mirror on the coupling ratio of the tap-coupler α is given by $R = 4\alpha(1 - \alpha)$ [82] and it has been plotted in the graph 6.17(a).

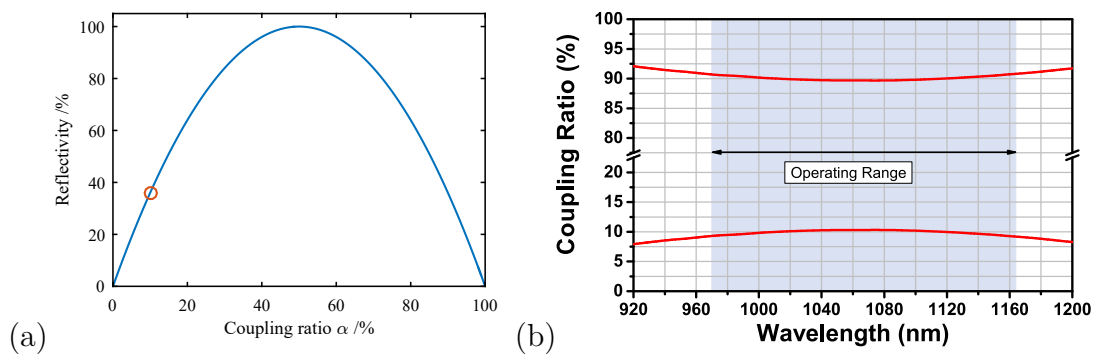


Figure 6.17: (a) Reflectivity of the linear loop mirror as a function of the coupling ratio. (b) Spectral behavior of the coupling ratio of a typical wideband tap-coupler [83].

By choosing a coupling ratio of 10% (red circle in figure 6.17a), the reflectivity of the loop mirror mimics the chirped fiber Bragg grating end-mirror of the setup described in ref. [81], which had an out-coupling ratio of about 33%. This out-coupling mirror works for a wide spectral range (figure 6.17b), is completely fiber-integrated and even has a fiber output that can be directly spliced to an amplifier. The second cavity mirror is the SAM which also works over a wide

6. Implemented Laser Sources for Multi-Photon and Coherent Raman Scattering Imaging

spectral range. The cavity has, therefore, a uniform round-trip loss over a broad wavelength range, which is only limited by the gain bandwidth of Ytterbium. Within this limit, the wavelength of the oscillator can be chosen freely with the narrow-band filter.

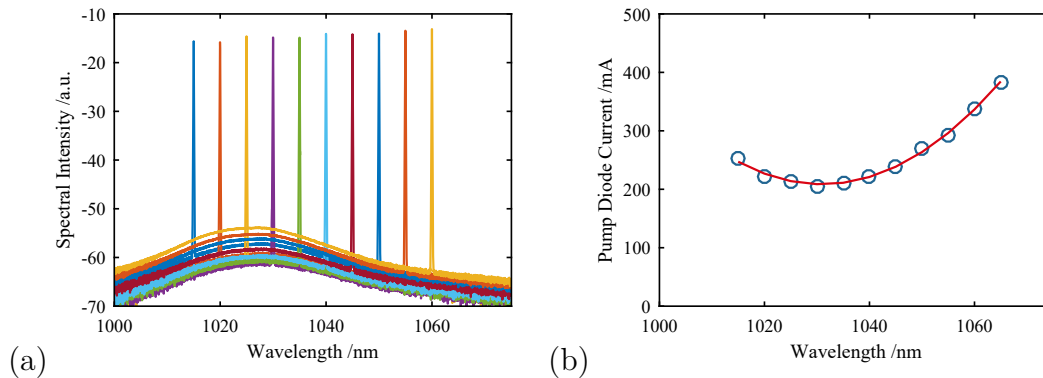


Figure 6.18: (a) Sample spectra at the tunable oscillator output. (b) Required pump current for a constant spectral bandwidth of 70 pm.

Figure 6.18(a) shows the output spectra of the oscillator for different filter positions. The wavelength can be chosen freely between 1015 and 1065 nm. The required pump current for the mode-locked state, in which the oscillator emits with a spectral bandwidth of 70 pm, is shown in figure 6.18(b). It is can be seen that the Ytterbium-doped fiber is most efficient at the gain peak for Ytterbium at 1030 nm and less efficient towards the edges of the tuning range. It is also visible how the ASE content becomes more and more significant at wavelengths oscillating away from the gain peak. The output power of the oscillator was between 5.0 mW at 1015 nm and 6.5 mW at 1065 nm. The small deviation might be due to a small wavelength dependence of the coupling ratio of the tap-coupler, the SAM and/or the WDM. The SAM was mounted on a linear delay stage which granted repetition rate tuneability of the oscillator. The cavity length could by altered by 30 mm or by 108 kHz. This feature is used to tune the signal light in the FOPO.

This tunable oscillator was used to seed an amplifier system, which delivered up to 75 nJ pulse energy at a repetition rate of 9.5 MHz (down from the original repetition rate of 19 MHz, see figure 6.19). An acousto-optical modulator spliced between the two amplifier stages was used to reduce the repetition rate and introduce the modulation, which is needed for detecting the SRS signal. Due to the relatively long pump pulse duration (40 ps), the amplification was accompanied by only moderate amounts of non-linear spectral broadening even without the use of pulse stretchers and compressors. The fiber OPO cavity consists of a 0.5 m long photonic crystal

6. Implemented Laser Sources for Multi-Photon and Coherent Raman Scattering Imaging

fiber (PCF, one-hole-missing core design, Yb core diameter 1.55 μm , pitch 3.1 μm) used for light conversion and amplification via four-wave mixing FWM, an output coupler and a 200 m long piece of polarization maintaining single-mode step-index fiber (PM 780).

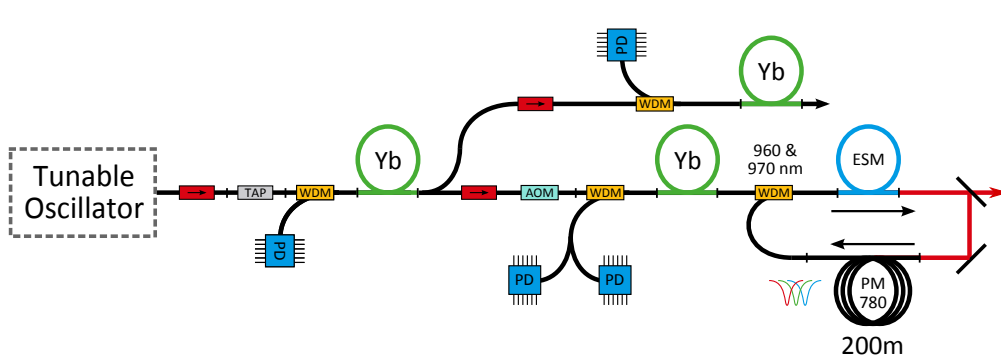


Figure 6.19: Setup of the all-fiber widely-tuneable FOPO for SRS microscopy. The oscillator was isolated and sampled in the tap coupler (Tap) to generate the modulation signal used to drive the acousto-optical modulator (AOM) and to reduce the repetition rate of the laser before it reached the FOPO cavity. In between, single-mode core-pumped amplifiers consisting of a pump diode (PD) at 976 nm, a wavelength division multiplexer (WDM) for coupling the light of the pump diodes to the signal and a Ytterbium doped fiber (Yb) was inserted in order to amplify the signal light were inserted. After the first amplifier, the secondary output was split and amplified again. The FOPO consisted of a broadband WDM that allowed the signal light from the feedback fiber (PM780) with the pump light to overlap. The feedback signal is seeding the FWM conversion of the pump in the endlessly single mode fiber(ESM).

It was demonstrated that changing the cavity length of the feedback loop in the FOPO cavity shifts the signal and idler wavelengths within the spectral gain region provided by the FWM process when pumped at a given pump wavelength. The same effect can be obtained if the cavity length of the Yb-doped fiber oscillator is changed. Finally, by tuning the wavelength of the oscillator and by adjusting its repetition rate, it is possible to address the wavelength range between 785 and 960 nm for the signal and 1177 and 1500 nm for the idler. Figure 6.20(a) depicts the signal and idler wavelengths that were obtained for different pump wavelengths when the repetition rate of the Yb-laser was set to be in resonance with the signal wavelength which produced the highest signal conversion efficiency. The corresponding resonant repetition rate is depicted in figure 6.20(b).

6. Implemented Laser Sources for Multi-Photon and Coherent Raman Scattering Imaging

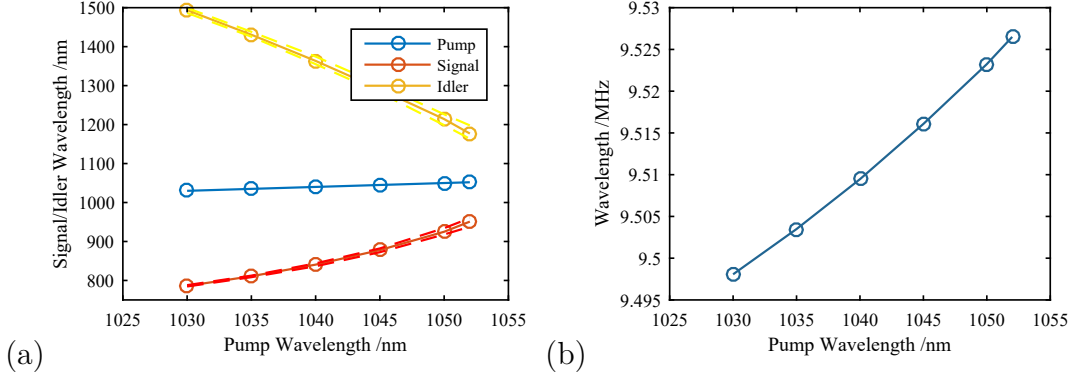


Figure 6.20: (a) Signal and idler generation at the resonant pump repetition rate (b). The dashed lines in (a) represent the edges of the tuning range, where the signal dropped to 50% of its peak value.

Tuning to a different signal or idler wavelength, therefore, only required the correct positioning of the translation-stage, which controlled the repetition rate of the Ytterbium laser and the setting of the narrow-band filter to set its wavelength to generate FWM gain at the desired signal and idler wavelength. This tuning method does not involve heating of crystals to adjust the phase-matching condition (which is usually done in free-space OPOs) and, therefore, a motorized version could set the desired central wavelengths of the pulse pairs in a couple of seconds.

On a side note, an even faster tuneable version of this FOPO could be accomplished by inserting a broadband chirped FBG into the ytterbium laser so that the repetition rate is automatically set to the repetition rate shown in figure 6.20(b) when the wavelength of the laser is set to a certain wavelength without the need of mechanical alteration of the cavity length. On top of that, if one could construct a fast tuneable filter, which has a filter bandwidth in the order 100 pm (e.g. a narrowband acousto-optical tunable filter, AOTF), the conversion could be controlled fully electronically and almost instantaneously. With the simulation depicted in figure 5.7 in mind, where it has been shown that the FOPO needs roughly 10 oscillations to reach the steady-state, it should be in principle possible to tune to a random wavelength within 10 μ s.

The tuning range of the signal towards longer wavelengths was limited by the spectral characteristic of the WDM and, therefore, it could be optimized to access even lower Raman shifts. The conversion efficiency (pump light to signal) was around 20%. Considering that comparable bulk OPO systems require a frequency doubled pump laser, the conversion efficiency of the system is on par with the overall conversion efficiency of state-of-the-art OPO systems. As the pump power requirements are low enough to allow for the use of single-mode pump diode

6. Implemented Laser Sources for Multi-Photon and Coherent Raman Scattering Imaging

modules, no water cooling was necessary. The overall system size was, therefore, of the order of a shoebox and may be easily integrated to existing laser scanning microscopes. Using an intensity auto-correlation it was determined that the signal pulse duration was around 20 ps (assuming a Gaussian pulse shape) at the peak conversion efficiency. We have measured a signal average power of 70 to 100 mW corresponding to a pulse energy of 7.8 to 11 nJ. The generated bandwidths were in the range of 0.4 to 1 nm FWHM. Frequency shifts between the generated signal and residual pump (910 to 3030 cm^{-1}) granted access to resonances in the CH-stretch region, the fingerprint region and deuterium or alkyne tag resonances for CARS. To enable SRS imaging, part of the pump radiation was split at an early stage in the amplifier chain. The RIN of the output at the modulation frequency of 9.5 MHz was measured to be -150 dBc (if the background noise of the RF spectrometer is removed).

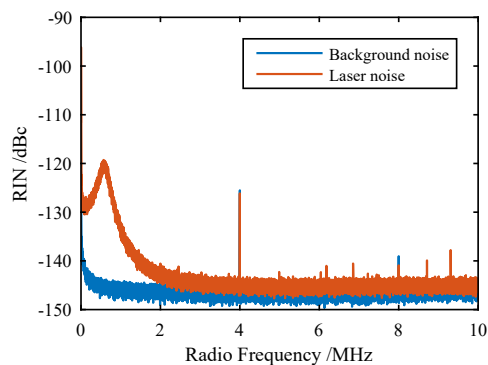


Figure 6.21: RIN measurement of the secondary output

With this RIN value, SRS imaging should be possible with a pixel dwell time of less than $1\text{ }\mu\text{s}$ enabling imaging at 4 frames per second at $500\times 500\text{ px}$ resolution (see 3.3). If necessary, additional noise reduction methods, such as a balanced signal detection could be applied for higher frame rates [84].

6.3.2 Linear Cavity FOPO

In order to eliminate the need for the free-space feedback and, therefore, to create a truly all-fiber FOPO cavity, the layout of the setup is altered. Even though it would be possible to employ a second WDM in order to split part of the generated signal, this method would require another splice between the EMS fiber and the signal-mode fiber of the WDM and, thus, produce unnecessary losses for the converted signal (such splices usually have an insertion loss of 1dB). A more elegant way is

6. Implemented Laser Sources for Multi-Photon and Coherent Raman Scattering Imaging

to use the already existing Fresnel reflection at the end-facet of the ESM fiber. The reflected signal travels back through this fiber and through the WDM goes into the delay fiber. At the end of the delay fiber the signal needs to be reflected by a broad band reflector to form a linear FOPO cavity. The down-side of this method is the need for an isolator for the pump radiation between the last amplifier stage and the FOPO cavity. Without this isolator the back-traveling FWM pump light, which is also reflected at the end-facet, would reach the last amplifier. The back-traveling light would be amplified and absorbed by the next isolator and would deplete partially the gain of the amplifier. The forward traveling light, which pumps the FOPO cavity would, consequently, become weaker which would also result in a drop in signal conversion efficiency. This, on the other hand, would lead to a decrease in signal and residual pump feedback which would allow the next pump pulse to be amplified to a higher pulse energy again. In the end, the output signal would fluctuate chaotically and the conversion would become inefficient. That is why the additional isolator is inserted in front of the FOPO to prevent this behavior. This also generates a higher accumulated non-linear phase in the pump pulses, since the amplified light needs to propagate through the isolator at full power before it reaches the FOPO. Consequently, this leads to an intensification of the behavior described in section 5.3, which works favorable for CRS imaging. Finally, the pump power requirements decrease since the feedback ratio is much higher and the less FWM gain is required to reach the steady state. The setup of the realized linear FOPO cavity can be seen in figure 6.22.

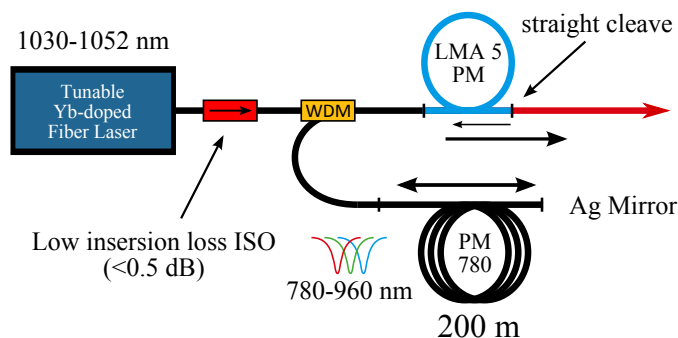


Figure 6.22: Setup of the linear FOPO cavity.

The FOPO setup, therefore, works without the need for any free space propagation which makes the setup extremely stable and alignment-free.

This setup has been built first as a laboratory prototype and later as a pre-commercial prototype to enable SRS imaging in real-world applications. The handling in the second installment is completely computer-controlled. By setting a

6. Implemented Laser Sources for Multi-Photon and Coherent Raman Scattering Imaging

desired Raman resonance, the computer sets the wavelength of the Ytterbium-doped fiber oscillator and its repetition rate via an electronically controlled narrowband filter and a linear delay-stage where the SAM is mounted on. The combination of both parameters determines the parameters of the conversion of the amplified radiation in the FOPO cavity, which is needed to realize the frequency shift requested by the user. To demonstrate the tuneability and performance of the laser system, the output spectra (figure 6.23a and b) and pulse parameters (figure 6.23c and f) of both outputs have been recorded between 922 and 3322 cm^{-1} in steps of 200 cm^{-1} .

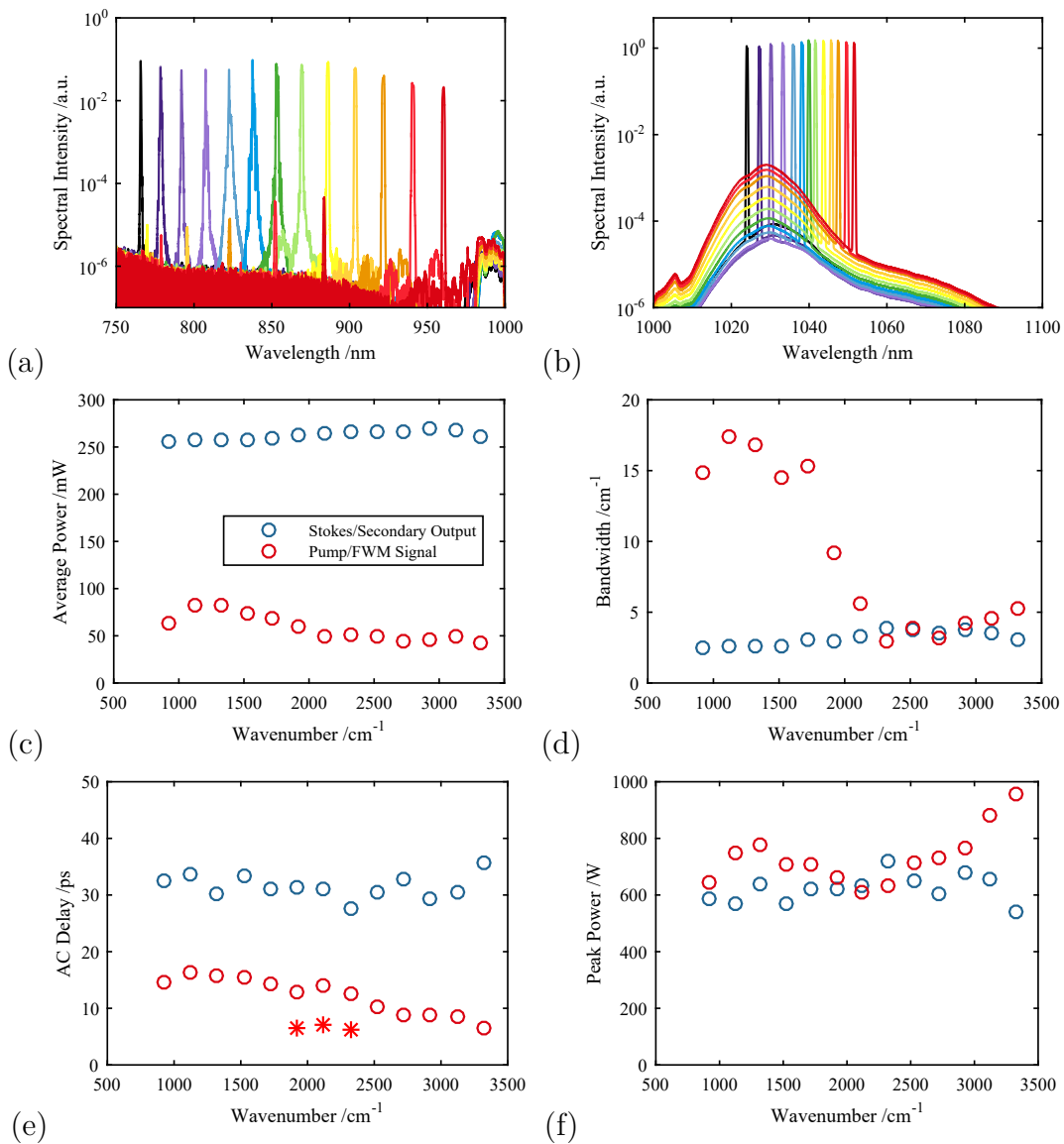


Figure 6.23: Output spectra and pulse parameters of the automated FOPO for the SRS laser system.

With the pulse parameters in mind, the wavelength and repetition rate of the oscillator are simultaneously tuned to deliver signal pulses with the highest peak power and small bandwidths. In this setup, the its generation is, again, heavily influenced by the SPM broadened pump pulses. To describe the pulse generation at different frequency shifts, a distinction between three different regions will be done. The first region is between 3322 and 2322 cm^{-1} and allows for narrow-band, short-pulse signal generation at moderate average powers. The second region between 2322 and 1722 cm^{-1} , can be characterized as a transition between the first and third region and features double pulses. The third region (below 1722 cm^{-1}) finally delivers broader and longer pulses but with at a higher average power. The main difference between these regions is the way the different gain bandwidth of the FWM conversion process allows a partial or a full conversion of the pump pulses. In section 5.3, it has been discussed that, for SPM-broadened pump pulses and narrow gain bandwidths, only a part of the pump pulse can be converted to a resonant oscillating signal in the FOPO cavity. If the bandwidth of the pump pulse is too large, the central wavelengths of the FWM gain spectra generated by the extreme components of the pump do not overlap. The conversion then becomes less efficient in terms of converted pulse energy but allows for short and narrow-band signals. This is because only a short and narrow-band part of the pump pulse is converted at each time. The peak-power conversion efficiency is not influenced by this effect (see 5.10c). A pump pulse which suffered strong SPM broadening but underwent a relatively weak dispersion ($L_{NL} \gg L_D$) (see eq. 4.20) has its highest spectral intensity at its wings [30]. This means that the front and back of the SPM broadened chirped pulse contains a relatively narrow but intense portion of the overall pulse spectrum. The FWM gain is, therefore, strong and narrow-band for the front and back temporal portion of the pump pulse. In the first region, where the conversion bandwidth is narrow, it is possible to convert only the front or back of the pump pulse, which results in narrow-band and short pulses (see 6.23d and e).

6. Implemented Laser Sources for Multi-Photon and Coherent Raman Scattering Imaging

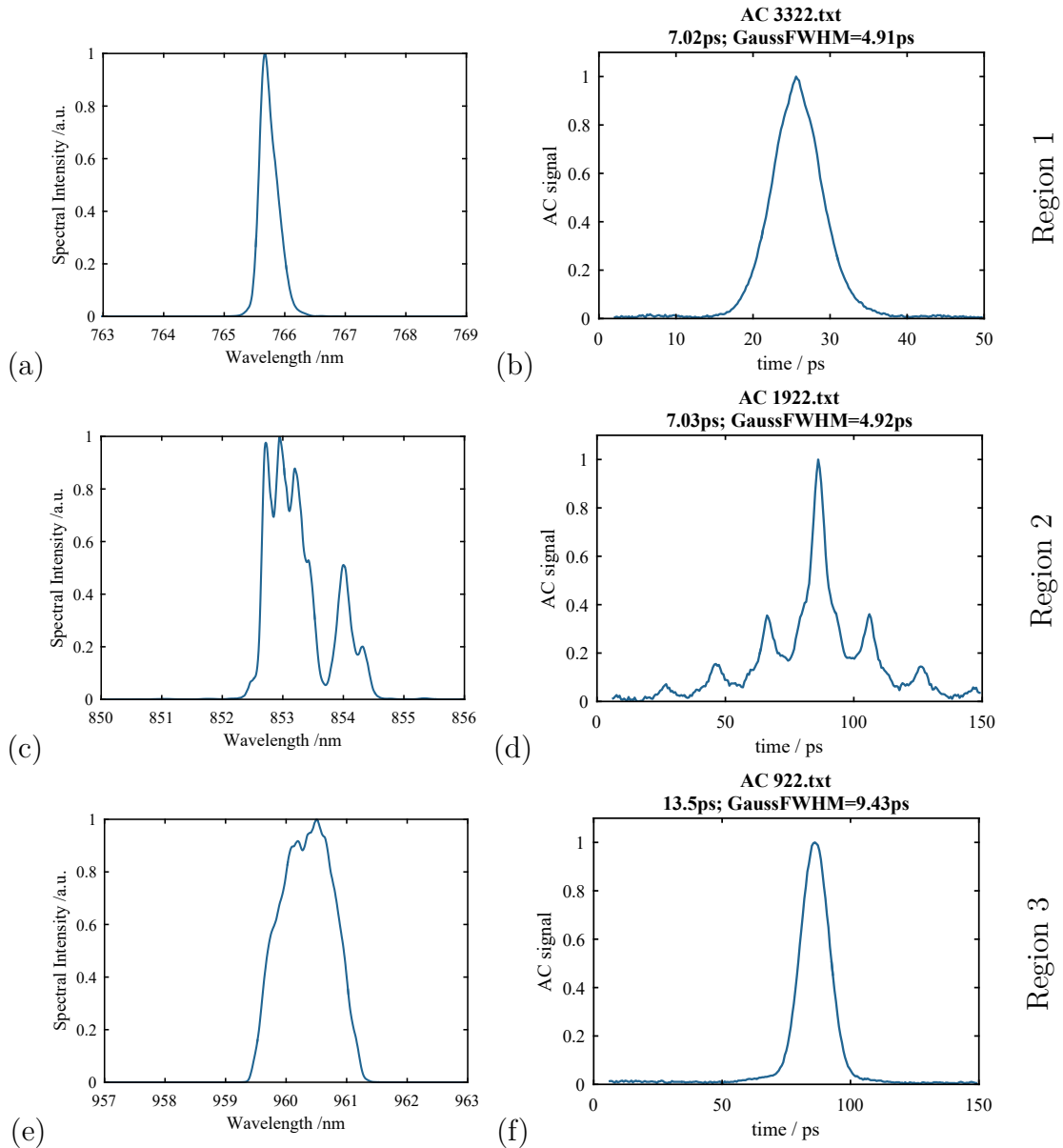


Figure 6.24: (a,c,e) Selected signal spectra at 3322, 1922 and 922 cm^{-1} . (b,d,f) Corresponding AC traces

One could say that, the pumping of the FOPO cavity with spectrally broad pump pulses results in an increase of the effectiveness of the dispersive filter of the cavity. In other words, the broadened pump pulses are only partially matched to a resonantly oscillating signal pulse. This is also why a conversion efficiency of only 12% was reached, which translates to a signal average power of about 50 mW in this region. In the third region, on the other and, the gain bandwidth is much broader which allows the whole pump pulse to contribute to the amplification of the oscillating signal. The output pulses are, therefore, much longer compared to the first region. The pulse generation in this region is then very comparable to the

conversion of pump pulses which were only slightly broadened by SPM (the FWM bandwidth is much broader than the pump pulse bandwidth). In the second region (the transition region), the bandwidth of the pump pulses and the (via the phase-matching condition) corresponding bandwidth of the FWM gain are comparable. Here it is possible that both the pulse front and back contribute to the conversion, but they pump a different part of the converted pulse. The result is a signal pulse with a hole in the middle of its spectrum. As the overall pulse shape is still chirped, the signal output can be understood as double pulses. If the conversion shifts further towards lower frequency shifts, the spectrum fills up and the pulse shape characteristic for region 3 forms. The resulting average power, therefore, increases towards lower frequency shifts since the whole pump pulse can be converted. At the lowest frequency shift of 922 cm^{-1} , the amplifier system becomes limited by amplified spontaneous emission, which results in lower conversion at this point. The overall average power of the secondary output (see panel 6.23d) is nearly constant. The recorded widths of the intensity auto-correlation (AC) reveal a decrease in pulse duration towards higher frequency shifts of the FWM signal. In the transition region, the AC reveals the generation of double pulses in the cavity, which is marked by a star in figure 6.23e. The effective pulse duration of these pulses is marked as red circles. These pulses are very short with an AC width of only 6 ps and are separated by about 20 ps, which corresponds well to the temporal separation of the spectral extrema of the pump pulses (it can be shown that this separation is at about 80% of the FWHM pulse duration for a Gaussian shaped pulse, see appendix 7). For comparison, the AC widths of the secondary output are in the range of 32 ps with an AC shape, which is very close to a Gauss. The pulse duration can be, therefore, estimated to be around 22.7 ps. The temporal separation between the edges of the pulse spectrum are then 19.3 ps apart, which matches the AC measurement very well. The resulting peak power of both outputs at each frequency separation can be seen in panel 6.23f. Even though the pulse generation of the signal can be very different depending on the frequency shift of the FWM based conversion, the resulting peak power over the whole range is quite uniform and higher than 500 W.

6.3.3 Application to CRS imaging

The laboratory prototype of the linear cavity was used to image different kinds of samples in order to compare the imaging quality using the CARS and the SRS imaging modality. The laser was set to 40 mW at 799 nm with a measured signal

6. Implemented Laser Sources for Multi-Photon and Coherent Raman Scattering Imaging

FWHM bandwidth of 0.35 nm. The transmitted signal power on the sample was 20 mW. The radiation at 1034 nm was compressed to maximize the overlap between the signal and pump wavelength. The main pulse feature of the signal was simulated to be 6 ps which is much shorter than the secondary output of the laser system at 40 ps. The secondary output, emitting at 1034 nm, was amplified to 300 mW which resulted in a bandwidth of 0.4 nm. The subsequent pulse compression used reflective gratings with 18001/mm with a separation of 75 mm, which resulted in a compressed pulse duration of 6 ps (confirmed by auto-correlation).

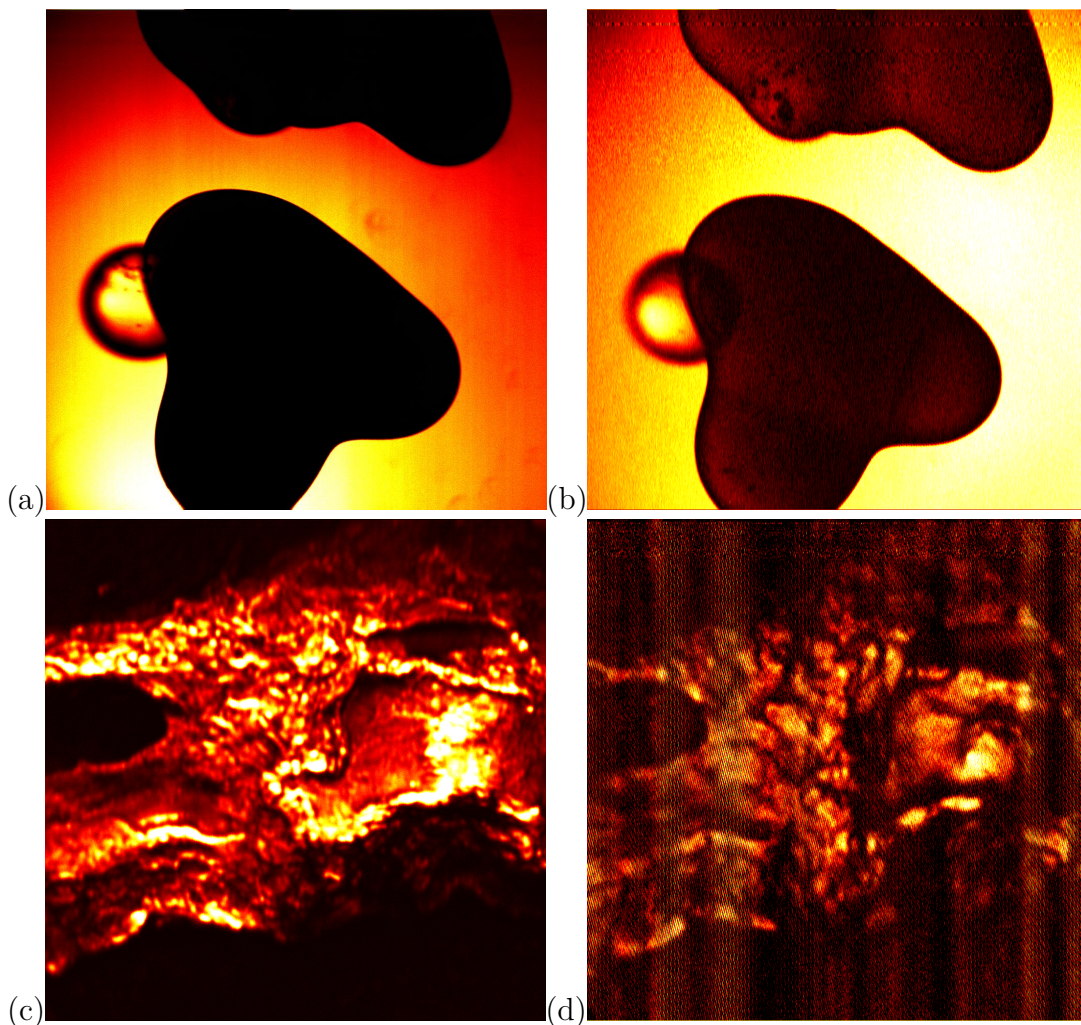


Figure 6.25: (a) CARS and (b) SRS measurements at 2850 cm^{-1} of glass beads in Cyclohexan. (c) CARS picture of a human aorta at 2850 cm^{-1} compared to the same section measured with SRS (d).

The compressed pulse was sent to the laser scanning microscope where 70 mW of the power reached the sample. Keeping in mind that this output has double the repetition rate of the SRS pump at 799 nm, the peak power ratio between the

6. Implemented Laser Sources for Multi-Photon and Coherent Raman Scattering Imaging

interacting pulses is fairly matched. Since biological tissue is less sensitive to light at around $1\ \mu\text{m}$, it is sensible to shift the peak power ratio slightly in favor of the radiation there [?].

The contrast of the CARS signal in the picture between the non-resonant glass beads and the cyclohexan is extremely high with a value of 80. The SRS signal offers still a good contrast of 8 at the fastest pixel acquisition rate of the employed laser scanning microscope of only $1\ \mu\text{s}/\text{pixel}$. At roughly the same resonance, a biological tissue sample similar to the one used in the CARS experiment above was scanned to map the lipid concentration in the sample. At the time of writing this thesis the digital lock-in caused strong interferences with the scanning signal, which gave rise to the appearance of stripes in the final SRS image when the gain in the lock-in was increased to detect the comparatively weak signal from the biological tissue sample. This is also the reason why the source was not used to image even weaker resonances in the fingerprint region. An improved imaging system should solve these issues in the near future.

7 Conclusion

In this thesis, the basic properties and advantages of multi-photon imaging and coherent Raman scattering (CRS) imaging over linear imaging techniques have been reviewed. The fundamental working principle of CRS has been explored in depth to deduct the optimal parameters for a driving laser source. An ambitious goal was set to implement these parameters in a novel kind of laser source based on fiber technology. Such a laser has often been referred to as the holy grail in biomedical imaging. A source which is powerful and versatile enough to drive these highly demanding imaging techniques and which is robust and compact enough to be deployed in a medical environment. Coupled with a sophisticated imaging system, the chemically sensitive nature of CRS could replace time-consuming staining procedures e.g. during cancer detection aside the operation table and enable the precise identification of the tumor directly on the patient without the need for biopsy.

The key technology which promised this dream to become reality is fiber based four-wave mixing. It enables the conversion of light within fibers without the need for additional free-space components. The conversion fibers can be spliced to standard fiber components and can be easily pumped by diode-pumped fiber lasers. After the implementation of this process in an optical parametric oscillator (OPO) cavity, the converted signal and idler radiation could fulfill the requirements for coherent Raman spectroscopy and multi-photon imaging. A deep understanding of the physics involved in the conversion process was the foundation to reach the desired pulse properties from such a source. It also sparked the idea of a wavelength tuneable all-fiber seed source, which allowed wide-band conversion and full fiber-integration. The key development for its realization was a simple and yet robust mode-locked oscillator which was continuously wavelength and repetition rate tuneable. The combination of this oscillator and the FWM-based OPO enabled a wide tuning range of 785 to 960 nm and 1177 to 1500 nm for the first laser output and 1015 to 1065 nm for the second output. The addresses energy differences between both channels can be set from 900 to over 3000 cm^{-1} or 1800 to over 6000 cm^{-1} if only the first channel is used. The system is in terms of peak

7. Conclusion

power, tuning range and pulse duration comparable to state-of-the-art free-space OPO systems but is conceptionally more simple, is inherently alignment-free, much more compact and offers near diffraction-limited beam quality.

The potency of the setup has been proven in different imaging experiments and has already found implementation in a prototype, where the wavelengths of the pump, signal and idler were automatically set by a computer. This system, therefore, represents the first turn-key, all-fiber, widely tuneable laser source and could mark the beginning of clinical non-linear imaging as a basic diagnostic tool by which tissue staining becomes more and more obsolete.

Bibliography

- [1] W. L. Peticolas and K. E. Rieckhoff, “Double-Photon Excitation of Organic Molecules in Dilute Solution,” *The Journal of Chemical Physics* **39**, 1347 (1963).
- [2] W. Denk, J. H. Strickler, and W. W. Webb, “Two-photon laser scanning fluorescence microscopy.” *Science (New York, N.Y.)* **248**, 73–6 (1990).
- [3] S. Maiti, B. Jason, W. Watt, J. B. Shear, R. M. Williams, W. R. Zipfel, and W. W. Webb, “Measuring Serotonin Distribution in Live Cells with Three-Photon Excitation,” *Science* **275**, 530–532 (1997).
- [4] D. V. Patel and C. N. J. McGhee, “Contemporary in vivo confocal microscopy of the living human cornea using white light and laser scanning techniques: A major review,” *Clinical and Experimental Ophthalmology* **35**, 71–88 (2007).
- [5] J. a.N. Buytaert, D. Adriaens, and J. J. Dirckx, “Orthogonal-plane fluorescence optical sectioning: a technique for 3-D imaging of biomedical specimens,” *Microscopy : science, technology, applications and education*, vol. 2 pp. 1356–1365 (2010).
- [6] N. G. Horton, K. Wang, D. Kobat, C. G. Clark, F. W. Wise, C. B. Schaffer, and C. Xu, “In vivo three-photon microscopy of subcortical structures within an intact mouse brain.” *Nature photonics* **7**, 205–209 (2013).
- [7] L. Wei, F. Hu, Y. Shen, Z. Chen, Y. Yu, C.-C. Lin, M. C. Wang, and W. Min, “Live-cell imaging of alkyne-tagged small biomolecules by stimulated Raman scattering.” *Nature methods* **11**, 410–2 (2014).
- [8] J.-X. Cheng and X. S. Xie, *Coherent Raman scattering microscopy* (CRC press, 2016).
- [9] A. Alfonso-García, R. Mittal, E. S. Lee, and E. O. Potma, “Biological imaging with coherent Raman scattering microscopy: a tutorial.” *Journal of biomedical optics* **19**, 71407 (2014).

- [10] E. Garmire, F. Pandarese, and C. H. Townes, “Coherently driven molecular vibrations and light modulation,” *Physical Review Letters* **11**, 160–163 (1963).
- [11] E. O. Potma, W. P. de Boeij, and D. a. Wiersma, “Nonlinear coherent four-wave mixing in optical microscopy,” *Journal of the Optical Society of America B* **17**, 1678 (2000).
- [12] J.-x. Cheng and X. S. Xie, “Coherent Anti-Stokes Raman Scattering Microscopy: Instrumentation, Theory, and Applications,” *J. Phys. Chem. B* pp. 827–840 (2004).
- [13] T. Gottschall, M. Baumgartl, A. Sagnier, J. Rothhardt, C. Jauregui, J. Limpert, and A. Tünnermann, “Fiber-based source for multiplex-CARS microscopy based on degenerate four-wave mixing.” *Optics express* **20**, 12004–13 (2012).
- [14] T. Meyer, M. Chemnitz, M. Baumgartl, T. Gottschall, T. Pascher, B. F. M. Romeike, B. R. Brehm, J. Limpert, A. Tünnermann, M. Schmitt, B. Dietzek, and J. Popp, “Expanding Multimodal Microscopy by High Spectral Resolution Coherent Anti-Stokes Raman Scattering Imaging for Clinical Disease Diagnostics,” *Analytical Chemistry* **14**, 6703–6715 (2013).
- [15] G. G. Krauss, T. Hanke, A. Sell, D. Trüçcutlein, A. Leitenstorfer, R. Selm, M. Winterhalder, A. Zumbusch, D. Träutlein, A. Leitenstorfer, R. Selm, M. Winterhalder, and A. Zumbusch, “Compact coherent anti-Stokes Raman scattering microscope based on a picosecond two-color Er: fiber laser system.” *Optics letters* **34**, 2847–9 (2009).
- [16] T. Gottschall, T. Meyer, M. Baumgartl, C. Jauregui, M. Schmitt, J. Popp, J. Limpert, and A. Tünnermann, “Fiber-based light sources for biomedical applications of coherent anti-Stokes Raman scattering microscopy,” *Laser & Photonics Reviews* **9**, 435–451 (2015).
- [17] M. Chemnitz, M. Baumgartl, T. Meyer, C. Jauregui, B. Dietzek, J. Popp, J. Limpert, and A. Tünnermann, “Widely tuneable fiber optical parametric amplifier for coherent anti-Stokes Raman scattering microscopy.” *Optics express* **20**, 26583–95 (2012).
- [18] A. Hopt and E. Neher, “Highly Nonlinear Photodamage in Two-Photon Fluorescence Microscopy,” *Biophysical journal* **80**, 2029–2036 (2001).

- [19] H. Wang, Y. Fu, and J.-X. Cheng, “Experimental observation and theoretical analysis of Raman resonance-enhanced photodamage in coherent anti-Stokes Raman scattering microscopy,” *Journal of the Optical Society of America B* **24**, 544–552 (2007).
- [20] K. König, H. Liang, M. W. Berns, and B. J. Tromberg, “Cell damage by near-IR microbeams,” *Nature* **377**, 20–21 (1995).
- [21] K. König, P. T. C. So, W. W. Mantulin, and E. Gratton, “Cellular response to near-infrared femtosecond laser pulses in two-photon microscopes,” *Optics Letters* **22**, 135–136 (1997).
- [22] K. König, T. W. Becker, P. Fischer, I. Riemann, and K.-J. Halbhuber, “Pulse-length dependence of cellular response to intense near-infrared laser pulses in multiphoton microscopes,” *Optics Letters* **24**, 113–115 (1999).
- [23] Y. Fu, H. Wang, R. Shi, and J.-X. Cheng, “Characterization of photodamage in coherent anti-Stokes Raman scattering microscopy.” *Optics express* **14**, 3942–51 (2006).
- [24] V. V. Yakovlev, “Advanced instrumentation for non-linear Raman microscopy,” *Journal of Raman Spectroscopy* **34**, 957–964 (2003).
- [25] C. Zhang, D. Zhang, and J.-X. Cheng, “Coherent Raman Scattering Microscopy in Biology and Medicine.” *Annual review of biomedical engineering* **17**, 415–445 (2015).
- [26] D. Kobat, M. E. Durst, N. Nishimura, A. W. Wong, C. B. Schaffer, and C. Xu, “Deep tissue multiphoton microscopy using longer wavelength excitation,” *Optics Express* **17**, 13354 (2009).
- [27] C. Xu, W. Zipfel, J. B. Shear, R. M. Williams, and W. W. Webb, “Multiphoton fluorescence excitation: new spectral windows for biological nonlinear microscopy.” *Proceedings of the National Academy of Sciences of the United States of America* **93**, 10763–10768 (1996).
- [28] A. C. S. Van Heel, “A New Method of transporting Optical Images without Aberrations,” (1954).
- [29] K. Kao and G. Hockham, “Dielectric-fibre surface waveguides for optical frequencies,” *Proceedings of the Institution of Electrical Engineers* **113**, 1151 (1966).

- [30] G. P. Agrawal, *Nonlinear Fiber Optics* (Academic Press, San Diego, 2001), 3rd ed.
- [31] R. W. Boyd, *Nonlinear Optics* (Academic Press, 2002), 2nd ed.
- [32] J. C. Knight, T. A. Birks, P. S. J. Russell, and D. M. Atkin, “All-silica single-mode optical fiber with photonic crystal cladding,” *Opt. Lett.* **21**, 1547–1549 (1996).
- [33] T. a. Birks, J. C. Knight, and P. S. J. Russell, “Endlessly single-mode photonic crystal fiber,” *Optics Letters* **22**, 961 (1997).
- [34] L. Brillouin, *Wave propagation and group velocity* (Academic Press, New York, 1960).
- [35] D. Mogilevtsev, T. A. Birks, and P. S. J. Russell, “Group-velocity dispersion in photonic crystal fibers,” *Opt. Lett.* **23**, 1662–1664 (1998).
- [36] S. H. L. Guang S. He, *Physics of Nonlinear Optics* (World Scientific, 1999).
- [37] R. H. Stolen, J. P. Gordon, W. J. Tomlinson, and H. A. Haus, “Raman response function of silica-core fibers,” *J. Opt. Soc. Am. B* **6**, 1159–1166 (1989).
- [38] A. E. Siegman, *Lasers* (Mill Valley, Calif., 1986).
- [39] K. Wang, N. Horton, K. Charan, and C. Xu, “Advanced Fiber Soliton Sources for Nonlinear Deep Tissue Imaging in Biophotonics,” *IEEE Journal of Selected Topics in Quantum Electronics* **20** (2014).
- [40] S. Ramachandran, J. M. Fini, M. Mermelstein, J. W. Nicholson, S. Ghalmi, and M. F. Yan, “Ultra-large effective-area, higher-order mode fibers: A new strategy for high-power lasers,” *Laser and Photonics Reviews* **2**, 429–448 (2008).
- [41] J. Rothhardt, A. M. Heidt, S. Hädrich, S. Demmler, J. Limpert, and A. Tünnermann, “High stability soliton frequency-shifting mechanisms for laser synchronization applications,” *Journal of the Optical Society of America B* **29**, 1257 (2012).
- [42] V. E. Zakharov and L. A. Ostrovsky, “Modulation instability: The beginning,” *Physica D: Nonlinear Phenomena* **238**, 540–548 (2009).

- [43] E. A. Golovchenko and A. N. Pilipentishii, “Unified Analysis of 4-Photon Mixing, Modulational Instability, and Stimulated Raman-Scattering Under Various Polarization Conditions in Fibers,” *J Opt Soc Am B* **11**, 92–101 (1994).
- [44] Djafar K. Mynbaev and Lowell L. Scheiner, *Fiber-Optic Communications Technology* (2001).
- [45] D. Nodop, C. Jauregui, D. Schimpf, J. Limpert, and a. Tünnermann, “Efficient high-power generation of visible and mid-infrared light by degenerate four-wave-mixing in a large-mode-area photonic-crystal fiber.” *Optics letters* **34**, 3499–501 (2009).
- [46] G. Renversez, F. Bordas, and B. T. Kuhlmeiy, “Second mode transition in microstructured optical fibers: determination of the critical geometrical parameter and study of the matrix refractive index and effects of cladding size.” *Optics letters* **30**, 1264–6 (2005).
- [47] N. a. Mortensen, M. D. Nielsen, J. R. Folkenberg, a. Petersson, and H. R. Simonsen, “Improved large-mode-area endlessly single-mode photonic crystal fibers.” *Optics letters* **28**, 393–395 (2003).
- [48] S. L.-S. Frederic Zolla, Gilles Renversez, Andre Nicolet, Boris Kuhlmeiy, Sebastien Guenneau, Didier Felbacq, Alexander Argyros, *Foundations of Photonic Crystal Fibers* (2012).
- [49] A. M. Heidt, “Pulse preserving flat-top supercontinuum generation in all-normal dispersion photonic crystal fiber,” *J Opt Soc Am B* **27**, 550–559 (2010).
- [50] S. L. Alfano, R. R. and Shapiro, “Emission in the Region 4000 to 7000 A Via Four-Photon Coupling in Glass,” *Phys. Rev. Lett.* **24**, 584–588 (1970).
- [51] J. M. Dudley and S. Coen, “Supercontinuum generation in photonic crystal fiber,” *Reviews of Modern Physics* **78**, 1135–1184 (2006).
- [52] J. Swiderski, “High-power mid-infrared supercontinuum sources: current status and future perspectives,” *Progress in Quantum Electronics* pp. 1–47 (2014).
- [53] S. Murugkar, C. Brideau, A. Ridsdale, M. Naji, P. K. Stys, and H. Anis, “Coherent anti-Stokes Raman scattering microscopy using photonic crystal

- fiber with two closely lying zero dispersion wavelengths,” *Optics Express* **15**, 14028–14037 (2007).
- [54] A. Tünnermann, T. Schreiber, F. Röser, A. Liem, S. Höfer, H. Zellmer, S. Nolte, and J. Limpert, “The renaissance and bright future of fibre lasers,” *Opt. Express* **38**, 681–693 (2005).
- [55] H. M. Pask, R. J. Carman, D. C. Hanna, A. C. Tropper, C. J. Mackechnie, P. R. Barber, and J. M. Dawes, “Ytterbium-doped silica fiber lasers: versatile sources for the 1-1.2 μm region,” *Selected Topics in Quantum Electronics, IEEE Journal of* **1**, 2–13 (1995).
- [56] X. Zhou, D. Yoshitomi, Y. Kobayashi, and K. Torizuka, “Generation of 28-fs pulses from a mode-locked ytterbium fiber oscillator,” *Optics Express* **16**, 7055–7059 (2008).
- [57] J. Hu, L. Zhang, and Y. Feng, “Widely Tunable Single-Mode Yb-Doped All-Fiber Master Oscillator Power Amplifier,” *IEEE Photonics Technology Letters* **27**, 2559–2562 (2015).
- [58] R. Royon, J. Lhermite, L. Sarger, and E. Cormier, “High power, continuous-wave ytterbium-doped fiber laser tunable from 976 to 1120 nm,” *Optics Express* **21**, 13818 (2013).
- [59] H. A. Haus, “Mode-locking of lasers,” *IEEE Journal on Selected Topics in Quantum Electronics* **6**, 1173–1185 (2000).
- [60] G. J. Sp??hler, S. Reffert, M. Haiml, M. Moser, and U. Keller, “Output-coupling semiconductor saturable absorber mirror,” *Applied Physics Letters* **78**, 2733–2735 (2001).
- [61] I. Duling, “Subpicosecond all-fibre erbium laser,” *Electronics Letters* **27**, 544 (1991).
- [62] K. Tamura, E. P. Ippen, H. a. Haus, and L. E. Nelson, “77-Fs Pulse Generation From a Stretched-Pulse Mode-Locked All-Fiber Ring Laser.” *Optics letters* **18**, 1080 (1993).
- [63] M. H. Ober, M. Hofer, and M. E. Fermann, “42-Fs Pulse Generation From a Mode-Locked Fiber Laser Started With a Moving Mirror.” *Optics letters* **18**, 367–369 (1993).

- [64] W. H. Renninger, A. Chong, and F. W. Wise, “Pulse Shaping and Evolution in Normal-Dispersion Mode-Locked Fiber Lasers.” *IEEE journal of selected topics in quantum electronics : a publication of the IEEE Lasers and Electro-optics Society* **18**, 389–398 (2012).
- [65] M. Baumgartl, C. Lecaplain, A. Hideur, J. Limpert, and A. Tünnermann, “66 W average power from a microjoule-class sub-100 fs fiber oscillator,” *Optics Letters* **37**, 1640 (2012).
- [66] M. Baumgartl, M. Chemnitz, C. Jauregui, T. Meyer, B. Dietzek, J. Popp, J. Limpert, and A. Tünnermann, “All-fiber laser source for CARS microscopy based on fiber optical parametric frequency conversion.” *Optics express* **20**, 4484–93 (2012).
- [67] E. S. Lamb, S. Lefrancois, M. Ji, W. J. Wadsworth, X. S. Xie, and F. W. Wise, “Fiber optical parametric oscillator for coherent anti-Stokes Raman scattering microscopy.” *Optics letters* **38**, 4154–7 (2013).
- [68] I. C. Chang, “Collinear beam acousto-optic tunable filters,” *Electronics Letters* **28**, 1255–1256 (1992).
- [69] G. Van der Westhuizen and J. Nilsson, “Fiber Optical Parametric Oscillator for Large Frequency-Shift Wavelength Conversion,” *IEEE Journal of Quantum Electronics* **47**, 1396–1403 (2011).
- [70] C. Jauregui, A. Steinmetz, J. Limpert, and A. Tünnermann, “High-power efficient generation of visible and mid-infrared radiation exploiting four-wave-mixing in optical fibers,” *Optics Express* **20**, 24957 (2012).
- [71] M. Baumgartl, T. Gottschall, J. Abreu-Afonso, A. Díez, T. Meyer, B. Dietzek, M. Rothhardt, J. Popp, J. Limpert, and A. Tünnermann, “Alignment-free, all-spliced fiber laser source for CARS microscopy based on four-wave-mixing.” *Optics express* **20**, 21010–8 (2012).
- [72] A. Chong, W. H. Renninger, and F. W. Wise, “All-normal-dispersion femtosecond fiber laser with pulse energy above 20 nJ.” *Optics letters* **32**, 2408–10 (2007).
- [73] a. Yariv, D. Fekete, and D. M. Pepper, “Compensation for channel dispersion by nonlinear optical phase conjugation.” *Optics letters* **4**, 52 (1979).

- [74] W. M. Grossman and D. M. Shemwell, “Coherence lengths and phase conjugation by degenerate four-wave mixing,” *Journal of Applied Physics* **51**, 914–916 (1980).
- [75] K. Inoue and T. Mukai, “Signal wavelength dependence of gain saturation in a fiber optical parametric amplifier,” *Optics Letters* **26**, 10 (2001).
- [76] Y. Q. Xu and S. G. Murdoch, “High conversion efficiency fiber optical parametric oscillator.” *Optics letters* **36**, 4266–8 (2011).
- [77] T. Gottschall, T. Meyer, M. Schmitt, J. Popp, J. Limpert, and A. Tünnermann, “Four-wave-mixing-based optical parametric oscillator delivering energetic, tunable, chirped femtosecond pulses for non-linear biomedical applications.” *Optics express* **23**, 23968–77 (2015).
- [78] T. Gottschall, T. Meyer, M. Baumgartl, B. Dietzek, J. Popp, J. Limpert, and A. Tünnermann, “Fiber-based optical parametric oscillator for high resolution coherent anti-Stokes Raman scattering (CARS) microscopy,” *Optics Express* **22**, 21921 (2014).
- [79] D. Kobat, N. G. Horton, and C. Xu, “In vivo two-photon microscopy to 1.6-mm depth in mouse cortex,” *Journal of Biomedical Optics* **16**, 106014 (2011).
- [80] A. Agnesi and L. Carrà, “Fourier-Limited 19-ps Yb-Fiber Seeder Stabilized by Spectral Filtering and Tunable Between 1015 and 1085 nm,” *Photonics Technology ...* **24**, 927–929 (2012).
- [81] B. Ortaç, M. Plötner, T. Schreiber, J. Limpert and A. Tünnermann, “Experimental and numerical study of pulse dynamics in positive net-cavity dispersion modelocked Yb-doped fiber lasers,” *Optics express* **15**, 15595 (2007).
- [82] N. J. Doran and D. Wood, “Nonlinear-optical loop mirror.” *Optics letters* **13**, 56–58 (1988).
- [83] Thorlabs, “<https://www.thorlabs.de>,” (2016).
- [84] C. W. Freudiger, W. Yang, G. R. Holtom, N. Peyghambarian, X. S. Xie, and K. Q. Kieu, “Stimulated Raman scattering microscopy with a robust fibre laser source,” *Nature Photonics* **8**, 153–159 (2014).

Appendix

The temporal position within a Gaussian shaped pulse, where the frequency shift induced by SPM is at its maximum

A Gaussian shaped pulse with a FWHM duration of 23 ps is plotted in figure 7.1. The first derivative and the points of contraflexure are added. Equation 4.17 states that the highest frequency shift is taking place at the points of contraflexure (where the first derivative has its extreme values).

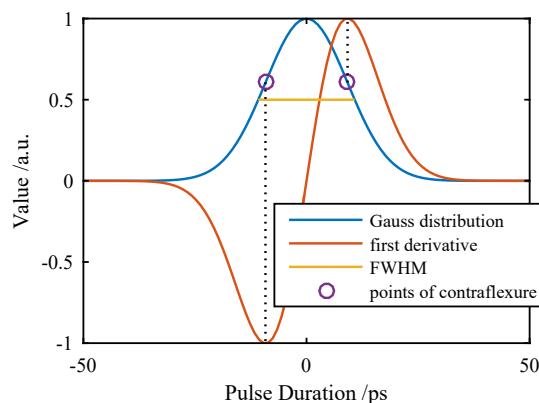


Figure 7.1: Gaussian shaped pulse with an FWHM of 23 ps, its first derivative and the points of contraflexure.

The rate of change in the vicinity of these points of the pulse are relatively small. Therefore, a large portion of the pulse energy is shifted to the edges of the spectrum, which is then concentrated around the points of contraflexure of the pulse.

Zusammenfassung (Summary)

In der vorliegenden Arbeit wurden die grundsätzlichen Eigenschaften und Vorteile von der Mehrphotonenbildgebung und der kohärenten Raman-Streuung (CRS)

gegenüber linearen Abbildungsverfahren untersucht. Die grundlegenden physikalischen Vorgänge von CRS wurden beleuchtet und im Hinblick auf die optimalen Parameter einer antreibenden Laserquelle untersucht. Es wurde das ambitionierte Ziel gefasst, den identifizierten Parametersatz durch eine neuartige Laserquelle, die allein auf Fasern und fasergekoppelten Komponenten basiert, darzustellen. Solch eine Lichtquelle wurde oftmals als der heilige Gral der biomedizinischen Bildgebung bezeichnet - eine Laserquelle, die einerseits leistungsfähig und flexibel genug ist diese anspruchsvollen bildgebenden Verfahren zu betreiben und andererseits auch robust und kompakt genug ist, um in einer klinischen Umgebung eingesetzt werden zu können.

Im Zusammenspiel mit einem leistungsfähigen Laserscanningmikroskop kann die chemische Sensibilität der CRS-Bildgebung beispielsweise genutzt werden, um zeitaufwändige Kontrastierungsverfahren bei der Krebsdiagnose abseits des Operationstisches, durch präzise Tumorortung direkt am Patienten abzulösen und so Biopsien unnötig zu machen.

Das Grundprinzip, einer solchen Quelle, ist die faserbasierte Vierwellenmischung (FWM). Diese ermöglicht die Konvertierung von Licht ohne die Verwendung von Freistrahlskomponenten. Die Konvertierungsfaser kann direkt an Faserkomponenten gespleißt werden und so durch diodengepumpte Faserlasersysteme gespeist werden.

Nachdem die Umsetzung dieses Konversionsprozesses in einem optisch parametrischen Oszillator (OPO) gelungen war und ein grundlegendes Verständnis über die physikalischen Mechanismen durch umfassende Simulationen hergestellt wurde, konnten die entstandene Signal- und Idlerstrahlung den Anforderungen der CRS- und Multiphotonenbildgebung angepasst werden. Es folgte die Konstruktion eines durchstimmbaren Faserlasers um eine große spektrale Durchstimmbarkeit des Gesamtsystems zu erreichen und eine vollständige Faserintegration zu ermöglichen. Der sowohl einfache als auch robuste modengekoppelte Faseroszillator ist damit die zweite Schlüsselkomponente dieser Arbeit. Die Kombination aus diesem Oszillator und dem FWM-basierten OPO ermöglicht adressierbare Wellenlängenbereiche von 785 bis 960 nm und 1177 bis 1500 nm vom ersten Ausgang und 1015 bis 1065 nm vom zweiten Ausgang. Die Energiedifferenz zwischen beiden Kanälen lässt sich im Bereich von 900 bis über 3000 cm^{-1} einstellen bzw. zwischen 1800 und über 6000 cm^{-1} , wenn nur der erste Ausgang verwendet wird. Das Potential dieser Quelle wurde in verschiedenen CRS-Mikroskopieexperimenten unter Beweis gestellt und bereits in Form eines automatisierten Prototypen realisiert, dessen Pump-, Signal- und Idlerwellenlängen per Knopfdruck einstellbar sind. Dieses Lasersystem ist damit das erste automatisch einstellbare, faserintegrierte und weit durchstimbare

7. Appendix

Lasersystem der Welt, welches nun das Potenzial besitzt die nichtlineare Mikroskopie als ein routinemäßiges Diagnoseverfahren zu etablieren und Kontrastmittel in der Morphologie überflüssig zu machen.

Danksagung (Acknowledgement)

An erster Stelle möchte ich mich bei meiner Familie und insbesondere bei meiner Frau Sophie für die tägliche Unterstützung bedanken. Ohne Dich wäre es nicht möglich gewesen. Meinen Eltern bin ich dankbar, dass sie mir den Bildungsweg finanziell ermöglicht haben und an den entscheidenden Stellen moralische Unterstützung leisteten diesen bis zu Ende zu gehen. Ich danke Euch.

Meiner Arbeitsgruppe danke ich für die jahrelange Zusammenarbeit. Insbesondere Hädi, Jan, Tino und Jens möchte ich für die Betreuung während meiner ersten Jahre am IAP danken. Ich habe unheimlich viel gelernt. Was ich heute über Faserlaser zu wissen hätte ich nirgendwo sonst lernen können. Ich bedanke mich nochmal explizit bei Jens, der stets an die für unsere Arbeitsgruppe ausgefallenen Laserkonzepte glaubte und deren Entwicklung ermöglichte. Danke, ich weiß, dass das nicht selbstverständlich war! Cesar und Martin möchte ich für den Ideenaustausch danken, wodurch ich die Herausforderungen des FOPO lösen konnte. Tom möchte ich für die Diskussionen und die daraus entstandenen Erweiterungen an Fiberdesk danken. Auch das war nicht selbstverständlich. Ich hoffe du weist, wie sehr mir dieses Programm half. Tino, dir möchte ich für die gemeinsamen Arbeiten an unseren UKP-Lasern danken. Ich denke immer gern an die gemeinsame Arbeit und an unser Motto, welchen an dieser Stelle aber nicht genannt sei, zurück.

Nun möchte ich mich besonders bei Tobias bedanken. Ohne Dich wären die schönen bunten Bildchen nicht entstanden und du liefertest die Motivation diese Laser zu bauen. Hans-Jürgen möchte ich für seinen professionellen Einfluss danken. Meine Aufbauten sind dadurch vielleicht nicht unbedingt aufgeräumter geworden, aber deutlich rechtwinkliger! Jan möchte ich speziell für den löblichen Beistand auf Dienstreisen danken und Hädi für die körperliche Regeneration dazwischen. Zu guter Letzt gilt mein Dank allen Kollegen, die über die Jahre geduldig die Entwicklung meiner Lowpower-Laser verfolgten.

Ehrenwörtliche Erklärung

Ich erkläre hiermit ehrenwörtlich, dass ich die vorliegende Arbeit selbständig, ohne unzulässige Hilfe Dritter und ohne Benutzung anderer als der angegebenen Hilfsmittel und Literatur angefertigt habe. Die aus anderen Quellen direkt oder indirekt übernommenen Daten und Konzepte sind unter Angabe der Quelle gekennzeichnet.

Bei der Auswahl und Auswertung folgenden Materials haben mir die nachstehend aufgeführten Personen in der jeweils beschriebenen Weise unentgeltlich geholfen:

- Cesar Jauregui bei der Erstellung einiger Simulationsskripte.
- Thomas Schreiber bei der Anpassung von Fiberdesk.
- Die Koautoren der entsprechenden Publikationen bei den durchgeführten Experimenten.

Weitere Personen waren an der inhaltlich-materiellen Erstellung der vorliegenden Arbeit nicht beteiligt. Insbesondere habe ich hierfür nicht die entgeltliche Hilfe von Vermittlungs- bzw. Beratungsdiensten (Promotionsberater oder andere Personen) in Anspruch genommen. Niemand hat von mir unmittelbar oder mittelbar geldwerte Leistungen für Arbeiten erhalten, die im Zusammenhang mit dem Inhalt der vorgelegten Dissertation stehen.

Die Arbeit wurde bisher weder im In- noch im Ausland in gleicher oder ähnlicher Form einer anderen Prüfungsbehörde vorgelegt.

Die geltende Promotionsordnung der Physikalisch-Astronomischen Fakultät ist mir bekannt.

Ich versichere ehrenwörtlich, dass ich nach bestem Wissen die reine Wahrheit gesagt und nichts verschwiegen habe.

Jena, den 04.01.2017

Thomas Gottschall